Assessment of Gonadal Toxicity of PARP Inhibitors on Human Ovary and Testis

by

Ece İLTÜMÜR

A Dissertation Submitted to the

Graduate School of Health Sciences in Partial

Fulfillment of the Requirements for the Degree

of

Doctor of Philosophy

in

Reproductive Medicine

KOÇ ÜNİVERSİTESİ

August 21, 2025

Assessment of Gonadal Toxicity of PARP Inhibitors
on Human Ovary and Testis

Koc University

Graduate School of Health Sciences

This is to certify that I have examined this copy of a doctoral dissertation by

Ece İLTÜMÜR

and have found that it is complete and satisfactory in all respects,
and that any and all revisions required by the final
examining committee have been made.

Committee Members:

Prof. Dr. Özgür ÖKTEM (Advisor)

Assist. Prof. Serçin Karahüseyinoğlu

Assist. Prof. İrem Durmaz Şahin

Prof. Dr. Volkan Turan

Prof. Dr. Fazilet Kübra Boynukalın

Date 21/08/2025

ACKNOWLEDGMENTS

I would like to extend my gratitude to myself for sustaining the commitment and strength required to continue throughout this demanding process and to reach the successful completion of my PhD.

ABSTRACT

Assessment of Gonadal Toxicity of PARP Inhibitors
on Human Ovary and Testis

Ece İLTÜMÜR
Doctor of Philosophy in Reproductive Medicine August 21, 2025

Objective: This research aimed to investigate the molecular and cellular impacts of PARP inhibitors (Niraparib and Olaparib) on human reproductive cells and tissues.

Methods: Human testicular and ovarian tissues, human luteinized granulosa cells, as well as the COV434 and HGrC1, were used. xCELLigence, MTT, SRB, and Calcein/PI staining were used to check cell proliferation and viability. Western blotting, flow cytometry, and immunofluorescence techniques were utilized to look at apoptosis and cell death. PCR and Western blotting methods have been conducted to assess steroidogenic genes and proteins. Estradiol, progesterone, AMH, and testosterone levels were measured from the culture medium.

Results: Inhibiting PARP results in a time and dose-dependent reduction in the proliferation of cells and induces apoptosis. In granulosa cells, the expression of genes involved in steroidogenesis was downregulated, resulting in a substantial reduction in progesterone synthesis, whereas estrogen and AMH levels remained unchanged. Olaparib dramatically elevated apoptotic markers in testicular tissue without affecting testosterone secretion.

Conclusion: This study shows that PARP inhibitors significantly affect the cytotoxicity and steroidogenesis in human reproductive cells and tissues. Results underscore the need to evaluate possible reproductive concerns associated with PARP inhibitors, especially regarding fertility preservation.

Keywords: PARP inhibitors, Niraparib, Olaparib, steroidogenesis, apoptosis, fertility

OZETCE

PARP İnhibitörlerinin İnsan Over ve Testis Üzerindeki Gonadal Toksisitesinin Değerlendirilmesi

Ece İLTÜMÜR
Üreme Tıbbı, Doktora
21 Ağustos 2025

Amaç: Bu çalışma, PARP inhibitörleri (Olaparib ve Niraparib)'nin insan üreme hücreleri ve dokuları üzerindeki moleküler ve hücresel etkilerini araştırmayı amaçlamaktadır.

Yöntem: Çalışmada insan testis ve over dokuları, insan luteinize granuloza hücreleri ile COV434 ve HGrC1 hücre hatları kullanıldı. Hücre proliferasyonu ve canlılığı xCELLigence, MTT, SRB ve Calcein/PI boyama yöntemleriyle değerlendirildi. Apoptoz ve hücre ölümü akım sitometrisi, immunofloresan ve Western blot analizleriyle incelendi. Steroidojenik gen ve proteinlerin ekspresyon düzeyleri PCR ve Western blot ile belirlendi. Estradiol, progesteron, AMH ve testosteron hormon düzeyleri kültür süpernatantlarından ölçüldü.

Bulgular: Sonuçlar, PARP inhibitörlerinin doz ve zamana bağlı olarak hücre proliferasyonunu baskıladığını ve apoptozu artırdığını göstermiştir. Granüloza hücrelerinde steroidogenezle ilişkili genlerin ekspresyonu azalmış, özellikle progesteron üretimi belirgin şekilde baskılanmıştır. Estradiol ve AMH düzeylerinde anlamlı değişiklik gözlenmemiştir. Testis dokusunda Olaparib, apoptoz belirteçlerini artırmasına rağmen testosteron düzeylerini etkilememiştir.

Sonuç: Bu çalışma, PARP inhibitörlerinin insan üreme hücrelerinde ve dokularında belirgin sitotoksik ve steroidogenez ile ilişkili etkiler oluşturduğunu ortaya koymaktadır. Bulgular, PARP inhibitörlerinin klinik kullanımında özellikle fertilite korunumu açısından dikkatle değerlendirilmesi gerektiğini göstermektedir.

Anahtar kelimeler: PARP inhibitörleri, Niraparib, Olaparib, steroidogenez, apoptoz, fertilite

TABLE OF CONTENTS

Isolation and Culture of HLGCs

Characterization of HLGCs

2.5.2 Mitotic Granulosa Cell Lines

COV43

HGrC1

2.5.3 Treatments for Cell Culture

2.6 In Vitro Culture of Human Ovarian Tissue

2.7 Preparation and Culture of Human Testicular Tissue

2.8 Treatments for cell and tissue culture

2.9 Flow Cytometry

2.10 Cell Cycle Analysis

2.11 Cell Viability Assays

2.11.1 MTT Assay

2.11.2 Calcein/PI Assay

2.11.3 SRB Assay

2.12 xCELLigence Real-Time Cell Analysis

2.13 Western Blot Analysis

2.13.1 Protein Isolation

2.13.2 Protein Concentration Measurement by BCA Assay

2.13.3 Gel Electrophoresis

2.13.4 Semi-Dry Transfer

2.13.5 Blocking

2.13.6 Primary and Secondary Antibody Incubation

2.13.7 Detecting

2.14 Immunofluorescent Staining

2.14.1 Immunofluorescent Staining of Cells

2.14.2 Immunofluorescent Staining of Tissue

2.15 Gene Expression Analysis

2.15.1 RNA Isolation

2.15.2 cDNA Synthesis

2.15.3 qRT-PCR

2.16 Hormone Assays

LIST OF TABLES

LIST OF FIGURES

Figure 48: Representative immunofluorescence images and quantification of normalized fluorescence intensity for cleaved PARP and 3β-HSD in HLGCs after a 96-hour treatment with Olaparib at concentrations of 10 μM, 20 μM, and 40 μM

Figure 49: Representative immunofluorescence images of human testis tissue sections stained for laminin (to verify tissue identity and integrity) and CYP17A1 (as a marker of steroidogenic Leydig cells) after a 96-hour treatment with increasing doses of Olaparib

Figure 50: Representative immunofluorescence images and quantification of normalized fluorescence intensity for StAR and Cleaved PARP in human testis tissue after 96-hour treatment with increasing concentrations of Olaparib

ABBREVIATIONS

3–ABA	3–Aminobenzamide
ACAT	Acyl Coenzyme A: Cholesterol Acyltransferase
ADPR	Adenosine Diphosphate Ribose
AM	Acetoxymethyl
AMH	Anti Müllerian Hormone
APE1	Apurinic/Apyrimidinic Endonuclease 1
AR	Androgen Receptor
ATM	Ataxia-Telangiectasia Mutated
BER	Base Excision Repair
BSA	Bovine Serum Albumin
BRCA1	Breast Cancer Type 1 Susceptibility Protein 1
BRCA2	Breast Cancer Type 2 Susceptibility Protein
C-NHEJ	Classical Non-Homologous End Joining
CHD2	Chromodomain Helicase DNA-Binding Protein 2
CI	Cell Index
COV434	Immortalized Granulosa Cell Line
CYP19A1	Aromatase
CYPs	Cytochrome P450s
DMEM	Dulbecco's Modified Eagle Medium
DHE	Dehydroepiandrosterone
DNA-PKcs	DNA-Dependent Protein Kinase Catalytic Subunit
DDR	DNA Damage Response
DSBs	Double-Strand Breaks
DMSO	Dimethyl Sulfoxide
DPBS	Dulbecco's Phosphate Buffered Saline
ECL	Enhanced Chemiluminescence
EMA	European Medicines Agency
FBS	Fetal Bovine Serum
FDX1	Ferredoxin
FDXR	Ferredoxin Reductase
FEN-1	Flap Endonuclease-1
FSH	Follicle Stimulating Hormone
GnRH	Gonadotropin-Releasing Hormone
HBSS	Hanks' Balanced Salt Solution

H&E	Hematoxylin-Eosin
HGrC1	Human Nonluteinized Granulosa Cell Line
HLGCs	Human Luteinized Granulosa Cells
HSDs	Hydroxysteroid Dehydrogenases
HR	Homologous Recombination
IMM	Inner Mitochondrial Membrane
IVF	In Vitro Fertilization
LH	Luteinizing Hormone
LHR	Luteinizing Hormone Receptor
LDL	Low-Density Lipoproteins
MRN	Mre11/Nbs1/Rad50 Complex
NAD	Nicotinamide Adenine Dinucleotide
NHEJ	Non-Homologous End-Joining
OMM	Outer Mitochondrial Membrane
PAR	Polymer of ADP-Ribose
PARP	Poly (ADP-Ribose) Polymerase
PARPi	PARP1/2 Inhibitors
PARylation	Poly(ADP-Ribosyl)ation
PARG	Poly(ADP-Ribose) Glycohydrolase
PI	Propidium Iodide
PNK	Polynucleotide Kinase
P450scc	Cytochrome P450 Cholesterol Side-Chain Cleavage Enzyme
qRT-PCR	Quantitative Real-Time PCR
ROS	Reactive Oxygen Species
RT	Room Temperature
SRB	Sulforhodamine B
SCE	Sister Chromatid Exchange
SMC1	Structural Maintenance of Chromosomes Protein 1
SSBR	Single-Strand Break Repair
SSBs	Single-Strand Breaks
SER	Smooth Endoplasmic Reticulum
StAR	Steroidogenic Acute Regulatory Protein
TA	Tunica Albuginea
TGF	Transforming Growth Factor
TOP1	Topoisomerase I

TOP1–SSBs	TOP1-Linked Single-Strand Breaks
TOP2	Topoisomerase II
17OHPreg	17α-Hydroxypregnenolon

CHAPTER 1
REVIEW OF LITERATURE

1.1 Gonadal Function and Fertility

Gonads are the main reproductive organs of males and females. In humans, the gonads are represented by two testes in males and a pair of ovaries in females.

1.1.1 Anatomy and Physiology of the Ovary

The ovaries situated within the pelvic cavity and enveloped by a mesothelium layer, perform many key roles, including the synthesis of female gametes and the release of female sex hormones (estrogen and progesterone) to control the postnatal growth of reproductive organs and the development of secondary sexual features (Jinno, 2025; Ma et al., 2023). The ovary comprises an outer cortex enveloped in the tunica albuginea and an inner medulla. The medulla comprises connective tissue that provides support for blood arteries, lymph vessels, and nerves. On the other hand, the cortex contains ovarian follicles at various stages of development (Puttabyatappa & Padmanabhan, 2018). Ovarian follicles are covered by stromal tissue. And the histological classification of ovarian follicles consists of three main types: primordial follicles, developing follicles (primary and secondary follicles), and mature follicles (Abraham L. Kierszenbaum, 2019).

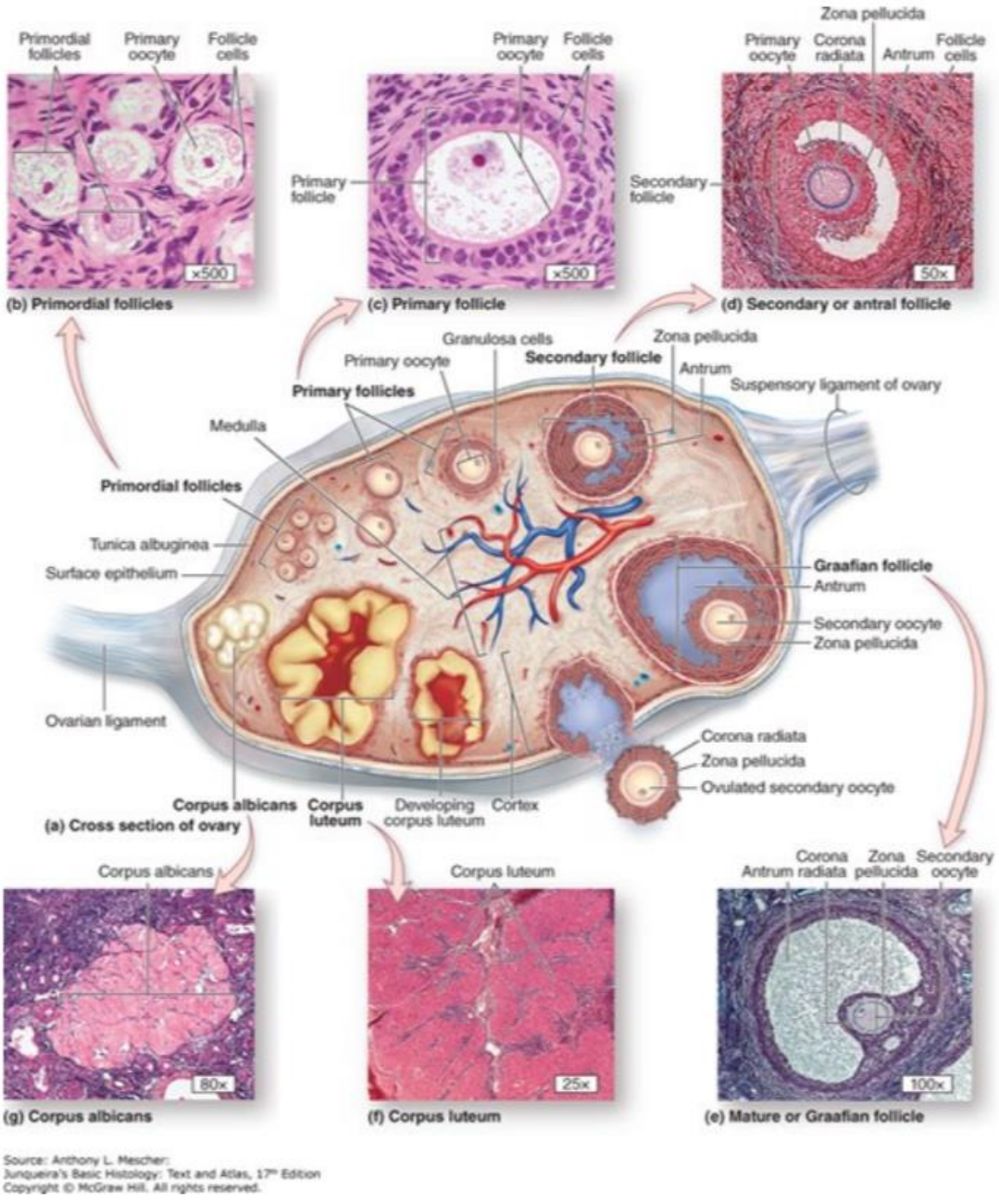

38

Figure 1. Ovarian follicle maturation (Mescher, 2024a) Follicular development, ovulation, and corpus luteum growth and degeneration are shown in (a). A mature follicle (e), a secondary follicle (d), a primary follicle (c), and primordial follicles (b) are all identified in the histological

sections. Subsequent to ovulation, the corpus luteum (f) is formed from the residuals of the follicle, which subsequently degenerates into the corpus albicans (g).

Primordial follicles are the most primitive stage of follicular development. Each of them comprises a primary oocyte, which is in a state of arrest during the prophase stage of meiosis I and is enveloped by a single layer of flattened follicular (pre-granulosa) cells (Gura & Freiman, 2018). Primordial follicles form by the week 16 of embryonic development until six months postnatally. Once the primordial follicle pool is developed, the primordial follicles start follicular differentiation or undergo apoptosis (Ma et al., 2023). The process of follicular differentiation from the primordial pool commences with follicular activation, which happens independently of gonadotropins and is modulated by locally synthesized growth factors, hormones, and cytokines, including kit ligand, fibroblast growth factor, transforming growth factor (TGF) α, bone morphogenetic protein 4, leukemia inhibitory factor, TGFβ, anti-Müllerian hormone (AMH), and androgens (Puttabyatappa & Padmanabhan, 2018). This phenomenon is termed initial recruitment, seen as an ongoing event beginning immediately upon follicle development, far in advance of pubertal commencement (McGee & Hsueh, 2000). Other type of primordial follicle recruitment is called cyclic recruitment which is gonadotropin-dependent (Figure 2) (Ma et al., 2023).

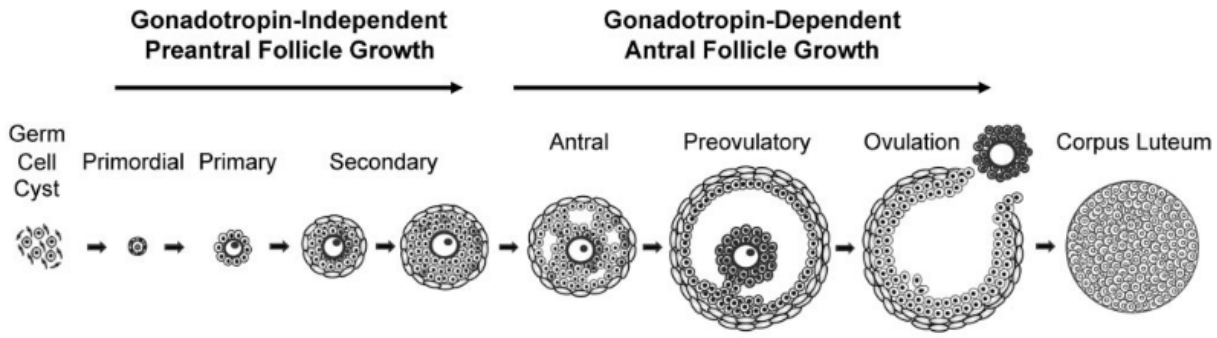

Figure 2. Outline of the main phases of folliculogenesis (Edson, Nagaraja, & Matzuk, 2009).

Oocyte development, together with the expansion and specialization of surrounding primordial granulosa cells, constitutes primordial follicle activation, yet, those oocytes stay suspended in the prophase phase of meiosis I (Y. Zhang et al., 2021). The granulosa cells are considered as supply sustenance required by the ovum and produce an oocyte maturation inhibitory

factor which maintains the ovum through the primordial condition at the prophase stage of meiotic division during childhood. Afterwards, at puberty, the ovaries (along with a portion of the follicles within them) start to develop as Follicle Stimulating Hormone (FSH) and Luteinizing Hormone (LH) from the anterior pituitary gland commence to be released (John E. Hall, 2020).

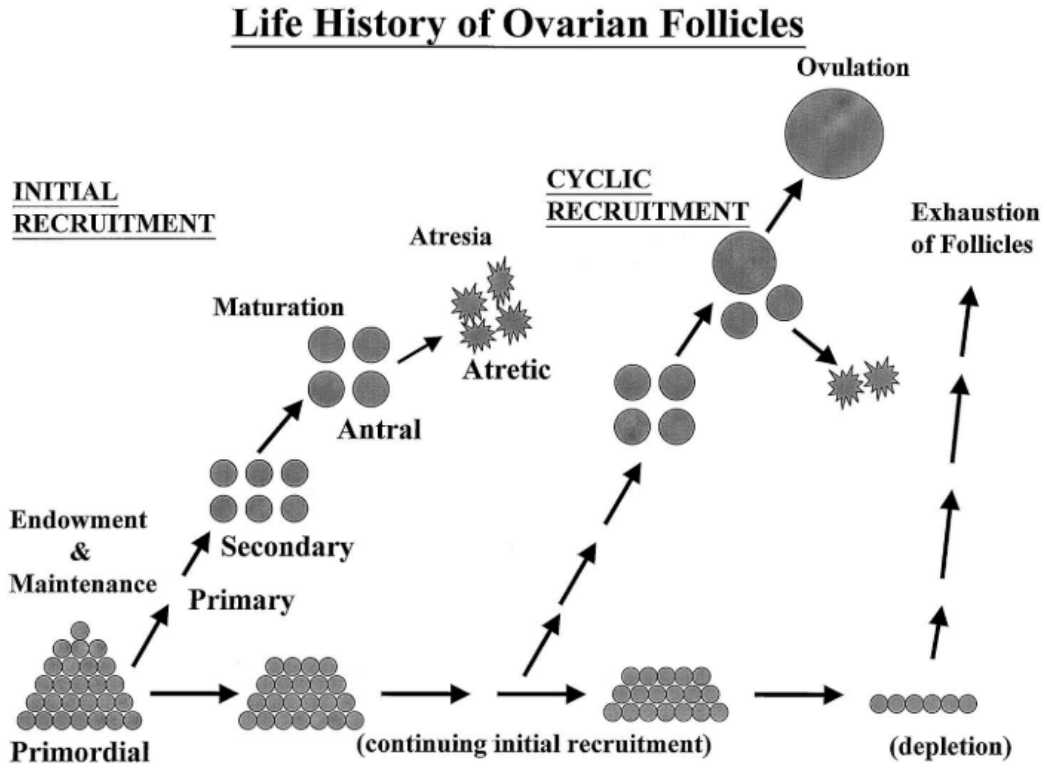

Figure 3. The developmental history of ovarian follicles (McGee & Hsueh, 2000).

The cyclic recruitment process commences with the beginning of puberty and results from the rise in circulating FSH throughout each reproductive cycle, which saves a group of antral follicles from atresia (McGee & Hsueh, 2000). Once females display reproductive cyclicity, there are cyclical changes in the pattern of hypothalamic Gonadotropin-releasing hormone (GnRH) secretion from the tonic and surge centers, which associate with the anterior pituitary to modulate the secretion levels of FSH and LH (Evans & Ganjam, 2017). Despite early follicle growth, FSH stimulation is essential for the maturation of large antral preovulatory follicles

(Macklon & Fauser, 2001). Under stimulation by FSH, the oocyte undergoes its most rapid growth in the early phases of follicular development. During this period, the nucleus enlarges, and mitochondria multiply in an equally spaced manner around the cell. The endoplasmic reticulum also greatly expands, and the golgi complexes will expand in size and move towards the periphery of the cell. Simultaneous follicular cells change into cuboidal in type around a growing oocyte. At this point, the follicle is referred to as the primary follicle. The follicular cells undergo continuous proliferation, resulting in the formation of a stratified follicular epithelium. At the moment, follicle cells are referred to as granulosa cells, and the follicle itself is a multilayered primary follicle. The zona pellucida (extracellular coat), which is composed of four glycoproteins that are released by the oocyte, forms between the oocyte and granulosa cells (Mescher, 2024a).

The oocyte's microvilli and the granulosa cells' processes (Transzonal projections) penetrate the zona pellucida, creating gap junctions that enable communication and promote follicular growth. During the process of follicular expansion, there is a significant development of gap junctions between the granulosa cells (Albertini, Combelles, Benecchi, & Carabatsos, 2001). In contrast to Sertoli cells located within the testis, the basal layer of granulosa cells lacks complex tight junctions (zonulae occludentes), which suggests that there is no blood-follicle barrier present. This situation allows the transfer of nutrients and tiny informational macromolecules from the bloodstream to the follicular fluid, which are crucial for the proper growth of the oocyte and the follicle (Abraham L. Kierszenbaum, 2019). The follicle undergoes a transformation into a small secondary follicle with two or more layers of granulosa cells as the oocyte grows and granulosa cells proliferate. One or two arterioles supply a small secondary follicle, which ends in an anastomotic network located just outside the basal lamina (Jinno, 2025). Stromal cells of these follicles begin to differentiate and form two layers: theca interna and theca externa. The theca interna, an inner highly-vascularized cellular layer, expresses luteinizing hormone receptor (LHR) and responds to this hormone stimulus, leading in turn to the production of androstenedione (Gougeon, 2010). Theca interna, which has fully differentiated with its vasculature, represents a large secondary follicle, and when theca interna cells resemble steroid-secreting cells, the large secondary follicles transition into the preantral stage. The appearance of fluid-filled spaces marks the transition to an early antral follicle. As the follicles enlarge, with the

oocyte increasing in size and the number of granulosa cells rising, small spaces begin to form within the granulosa layer due to the secretion of follicular fluid. This fluid accumulates, causing the spaces to gradually merge, and the granulosa cells rearrange themselves around a larger cavity known as the antrum (Jinno, 2025). During the reorganization of the granulosa layer to form the antrum, some cells form a slight hillock known as the cumulus oophorus. It surrounds the oocyte and extends into the antrum (Mescher, 2024a)

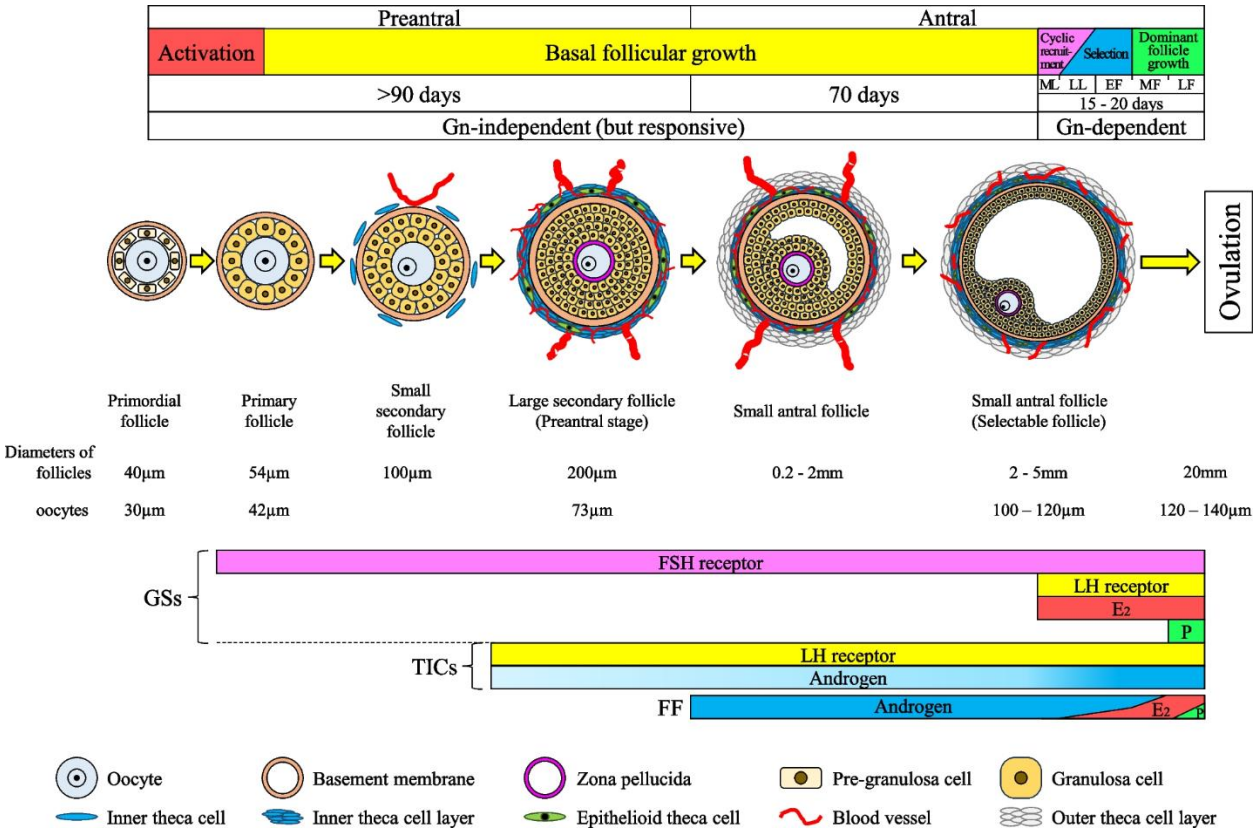

Figure 4. Overview of folliculogenesis (Jinno, 2025).

At each menstrual cycle, normally a single follicle has much more growth compared to the rest and forms the dominant follicle, although many of the other follicles ultimately undergo atresia (John E. Hall, 2020). The dominant follicle often achieves the highest level of follicular development and can go through ovulation. This mature or preovulatory follicle referred to

graafian follicle, grows to a size of 20-30 mm or more before ovulation. Due to its considerable dimensions, it spans the entire depth of the ovarian cortex and results in a protrusion on the ovary's surface. Once the interstitial spaces among the granulosa cells progressively increase, the oocyte and cumulus cells are incrementally separated from the remaining granulosa cells in preparation for ovulation. The cumulus cells around the oocyte now constitute the monolayer of cells known as the corona radiata, and they stay with the oocyte during ovulation (Pawlina & Ross, 2018). As the mid-cycle nears, the increase in estrogen from the dominant follicle triggers an LH surge and, to a lesser degree, an FSH surge. This initiates the recommencement of meiosis, ovulation, and luteinization (*Yen & Jaffe's Reproductive Endocrinology*

Physiology, Pathophysiology, and Clinical Management 2019).

1.1.2 Anatomy and Physiology of the Testis

The male gonads, known as the testes, perform two critical functions: spermatogenesis (the generation of male gametes) and the synthesis and release of male sex hormones (Wistuba, Neuhaus, & Nieschlag, 2023). The paired testes grow up in the abdomen and descend into the scrotum just before birth, where the temperature is 2-3 °C lower than the body's temperature. The reduced temperature is crucial for spermatogenesis (Cameron, 2007). But this lower temperature is not required for hormone production.

The human testes possess a notably thick connective tissue capsule, tunica albuginea (TA) and the inner part of TA is a loose connective tissue layer, tunica vasculosa. Posteriorly, TA thickens to form the mediastinum testis (Figure 5). Near the mediastinum, seminiferous tubules assume a short straight course-straight tubule, and this straight tubule becomes continuous with rete testis. The incomplete septa meeting in the mediastinum testis divide each testis into around 250–350 lobules, and each lobule consists of significantly convoluted seminiferous tubules responsible for sperm production (Fietz & Bergmann, 2017). The seminiferous tubules include spermatogenic cells at different stages of maturation and Sertoli cells supplying structural support, nutrition, regulatory and paracrine substances to the germ cells. Sertoli cells are anchored to the basement membrane and surround the spermatogenic cells (Pawlina & Ross, 2018). Prepubescent Sertoli

cells synthesize elevated concentrations of AMH independently of FSH and commence the expression of the androgen receptor (AR). Elevated AMH expression levels characterize immature Sertoli cells during the prenatal phase and prepubescence. The quantity of AR positive Sertoli cells and their expression levels rise progressively until the onset of puberty. As puberty commences, AMH levels begin to diminish due to the direct influence of androgens on Sertoli cells (Edelsztein & Rey, 2019). Moreover, Sertoli cells face a significant transformation in their morphology and function at the start of puberty, indicating the transition from an immature, proliferative state to a mature, non-proliferative state (Sharpe, McKinnell, Kivlin, & Fisher, 2003).

It is widely recognized that the proliferation and functional maturation of Sertoli cells are regulated by FSH and androgens. Additionally, FSH controls Sertoli cell proliferation exclusively during fetal and early postnatal life, while it regulates differentiation following the cessation of mitosis at puberty (Meroni et al., 2019). By way of example, Sertoli cells respond to FSH stimulation and express androgen receptors (Verhoeven & CAILLEAU, 1988). It is crucial because androgens must interact with Sertoli cell AR in order to induce spermatogenesis (O'shaughnessy, Verhoeven, De Gendt, Monteiro, & Abel, 2010). Moreover, the expression of inhibin B in Sertoli cells is stimulated by FSH, which serves as negative feedback for the secretion of FSH in the pituitary (Namwanje & Brown, 2016). Another crucial aspect that occurs at the onset of puberty is the establishment of intimate connections (tight and gap junctions) between Sertoli cells, which enables the controlled transport of substances and molecules through cell membranes (Wistuba et al., 2023). This inter-Sertoli cell tight junctions situated on the luminal side of the basally located spermatogonia and preleptotene/leptotene primary spermatocytes (first germ cells derived from spermatogonia) form the blood-testis barrier (Degroot, Jameson, & De Kretser, 2016). The blood-testis barrier serves to isolate germ cells in the adluminal compartment from the lymphatic and circulatory systems. (Mruk & Cheng, 2015). This physicobiochemical barrier establishes the immunologically favorable environment within the seminiferous epithelium, allowing meiosis, the generation of round spermatids, and the processes of spermiogenesis and spermiation (T. Plant, Ramaswamy, & De Gendt, 2016).

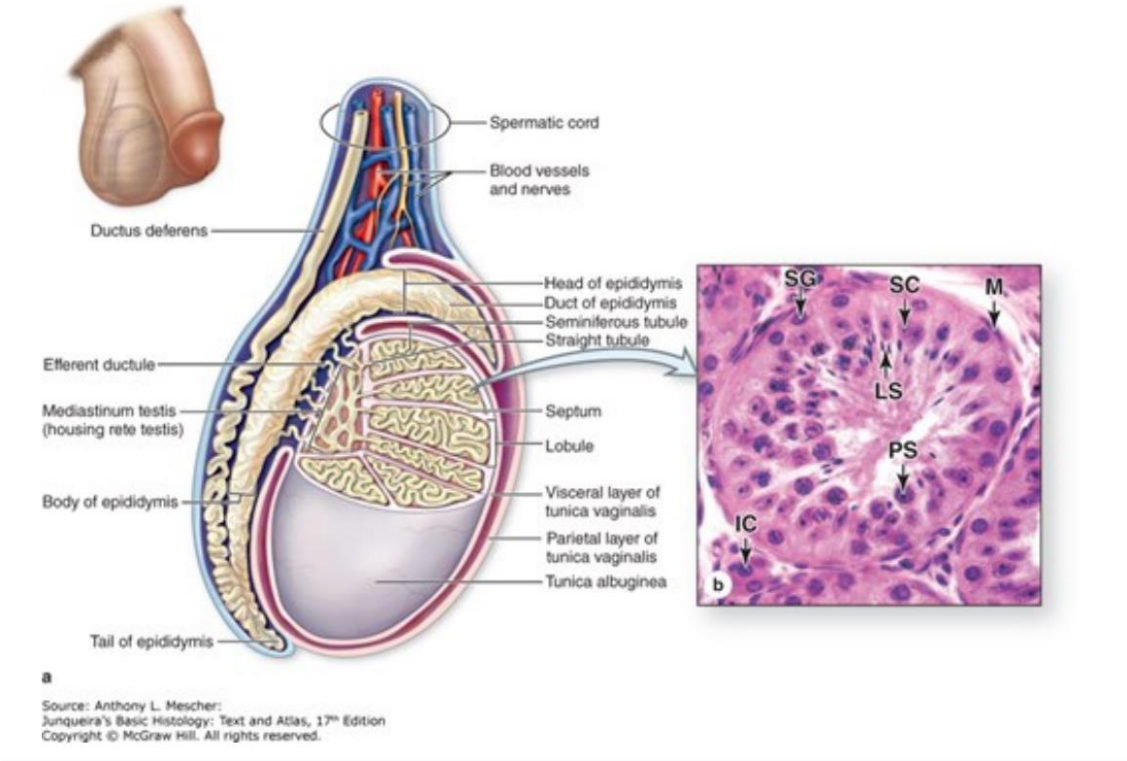

Figure 5. Testes and seminiferous tubules (Mescher, 2024b) The illustration depicts a slightly sectioned sagittal view of the testis (a). A cross slice of a seminiferous tubule reveals spermatogonia (SG) positioned at the edge, next to the nuclei of Sertoli cells (SC), primary spermatocytes (PS), and late spermatids (LS) located in the lumen, with interstitial cells (IC) present in the surrounding connective tissue (b).

Spermatogenesis is the process by which spermatogenic cells consistently proliferate and develop into mature spermatozoa (Griswold, 2016). That starts just prior to puberty, influenced by increasing gonadotropins, and persists all along life. Furthermore, it is categorized into 3 different stages: Spermatogonial phase, spermatocyte phase and spermatid phase (Suede, Malik, & Sapra, 2020). In spermatogonial phase, stem cells undergo multiple divisions and produce spermatogonial progeny. Human spermatogonia are categorized as three separate groups according to the morphology of the nuclei. These are Type A dark spermatogonia with darker nuclei, Type A pale spermatogonia with pale nuclei and Type B spermatogonia. Type A dark spermatogonia give rise to a pair of Type A pale spermatogonia (Gizer, Önen, & Korkusuz, 2024). Then, Type A pale spermatogonia differentiate into Type B spermatogonia. In the

spermatocyte phase, Type B spermatogonia give rise to primary spermatocytes, which will enter meiosis I and, by meiosis I, they form secondary spermatocytes, and by meiosis II, secondary spermatocytes will form spermatids (Figure 6). These spermatids go into the spermatid phase, where they differentiate into mature sperm cells (Robinson, Sparanese, Witherspoon, & Flannigan, 2023). Upon completion of spermatogenesis, spermatids complete final maturation and are discharged into the lumen of the seminiferous tubule during a process known as spermiation (Pawlina & Ross, 2018).

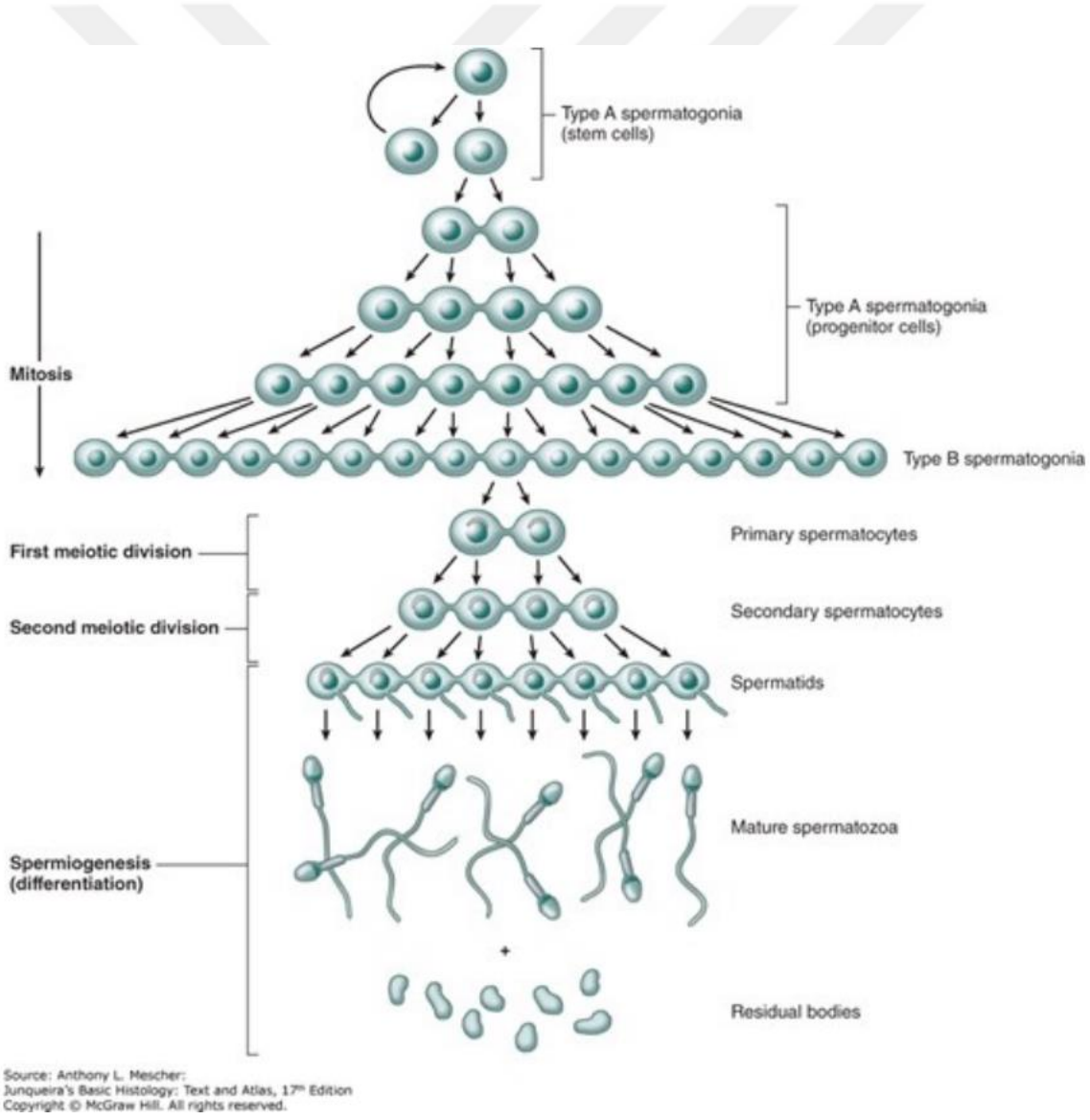

Figure 6. Clonal characteristics of spermatogenesis (Mescher, 2024b).

Spermatogenesis is controlled by FSH and androgens secreted by Leydig cells in reaction to LH (O'shaughnessy et al., 2010). Leydig cells, along with blood arteries, lymphocytes, macrophages, lymphatic vessels, and connective tissue, exist in the interstitial compartment (interstitium), the area between the seminal tubules (Mital, Hinton, & Dufour, 2011).

Male fetuses need a certain level of androgens during a designated timeframe to enable the development of the male reproductive system (Jiang & Jorgensen, 2024). Leydig cells differentiate and start to secrete testosterone during the early differentiation of the male fetus (Scott, Mason, & Sharpe, 2009). Subsequently, they experience a phase of dormancy around four months of fetal development, and upon gonadotropic activation during puberty, they reestablish their function as androgen-secreting cells, remaining active for the duration of life (T. M. Plant & Zeleznik, 2014). In puberty, Leydig cells emerge alone or in small clusters as large polygonal cells characterized by central nuclei and eosinophilic cytoplasm abundant in mitochondria, smooth endoplasmic reticulum (SER), and tiny lipid droplets (Mescher, 2024b). The proper formation of the male fetus's gonads depends on the presence of testosterone in the embryo. It controls the commencement of spermatogenesis, the secretion of accessory reproductive glands, and the emergence of secondary sexual characteristics during puberty. In adulthood, it is essential for the preservation of secondary sexual traits and sperm production (Bhattacharya & Dey, 2023). Testicular testosterone secretion is significantly influenced by the hypothalamic–pituitary axis. GnRH stimulates the biosynthesis and secretion of LH by binding to a membrane receptor on pituitary gonadotrophins. LH binds to the LHR on Leydig cell surfaces, consequently activating intracellular signaling pathways (Zirkin & Papadopoulos, 2018). As a final point, Leydig cell function is mainly regulated by LH and Prolactin (inducing expression of LHR) (Purvis & Hansson, 1978).

1.2 Steroidogenesis in Gonads and Its Regulation

1.2.2 Key Enzymes in Steroidogenesis

Steroidogenesis is the biological process by which cholesterol is converted into steroid hormones (Haggstrom, 2014). Steroidogenic cells get cholesterol from three primary sources: de novo synthesis, lipoprotein cholesterol, and intracellular cholesteryl ester reserves (Gwynne & Strauss,

1982). Cholesterol might be produced de novo by an enzymatic pathway starting with acetate (Porter & Herman, 2011). Nevertheless, steroidogenic tissues mostly depend on cholesterol obtained from circulating lipoproteins under normal conditions. While rodents preferably utilize the high density lipoproteins via scavenger receptor B1, in humans the main source is low-density lipoproteins (LDL), which is absorbed via receptor-mediated endocytosis (W. L. Miller, 2013). The ensuing endocytic vesicles merge with lysosomes, where engulfed LDL proteins undergo proteolytic degradation, releasing cholesterol esters that are later hydrolyzed to free cholesterol by lysosomal acid lipase (Esmaeilian et al., 2023). Due to the localization of the cholesterol side-chain cleavage enzyme (P450scc) system to inner mitochondiral membrane (IMM), the commencement of steroidogenesis is centered on the movement of cholesterol from the outer mitochondiral membrane (OMM) to the IMM. In specialized steroidogenic cells, steroidogenic acute regulatory protein (StAR) is responsible for transporting cholesterol from the OMM to the IMM (W. L. Miller, 2007). Free cholesterol that is not transported to the IMM via StAR is esterified via the 3β-hydroxyl group to polyunsaturated fatty acids or to sulfate, which is mediated via the microsomal acyl coenzyme A:cholesterol acyltransferase (ACAT) and recently produced cholesterol esters gather inside the rough endoplasmic reticulum then bud out as cytoplasmic lipid droplets (Christenson & Devoto, 2003).

Steroidogenesis is regulated at various levels, primarily through the transcription of genes that encode steroidogenic enzymes and co-factors, as well as their post-translational modifications (Bremer & Miller, 2014). In the 1980s, the isolation of several critical steroidogenic enzymes from animals and the subsequent cloning of numerous cDNAs and genes demonstrated that there were significantly fewer steroidogenic enzymes than steroidogenic reactions. Most of the time, the same enzyme was responsible for catalyzing the same steroidogenic process across all organs. The majority of enzymes participating in steroid biosynthesis are either hydroxysteroid dehydrogenases (HSDs) or cytochrome P450s (CYPs). These enzymes operate unidirectionally, thus the accumulation of the product does not induce a return flux to the precursor. Reactions mediated by Cytochrome P450, such as hydroxylations and carbon–carbon bond cleavages, are both physiologically and mechanistically non-reversible whereas HSDs are theoretically reversible but typically function unidirectionally in vivo (W. L. Miller & Auchus, 2011).

Cytochrome P450 is an insufficient designation for a family of proteins classified as oxygenase enzymes that contain a non-covalently bound protoporphyrin (heme) cofactor (Hall, 1986). The

enzymes have been called P450 (pigment 450) due to their absorption of light at 450 nm in their reduced forms (W. Miller, 2008). The genes encoding these enzymes have been identified as CYP genes and there are total 57 CYP genes within the human genome, with six principal enzymes facilitating specific stages in steroid hormone biosynthesis. Mitochondrial CYP11A1 (P450scc) facilitates the cleavage of the cholesterol side chain, thereby initiating steroid biosynthesis. CYP11B1 (11β-hydroxylase) and CYP11B2 (aldosterone synthase), both mitochondrial enzymes, facilitate 11β-hydroxylase, 18-hydroxylase, and 18-methyloxidase activities. Meanwhile, the endoplasmic reticulum-associated CYP17A1 performs 17α-hydroxylase and 17,20-lyase reactions, whereas CYP21A2 catalyzes the 21-hydroxylation of glucocorticoid and mineralocorticoid precursors. Additionally, CYP19A1 (aromatase) converts androgens into estrogens within the gonads (Bremer & Miller, 2014).

The 3α- and 3β-HSDs, two 11β-HSDs, and a set of 17β-HSDs constitute the HSDs. While the majority of steroidogenic events facilitated by P450 enzymes involve a singular P450 form, each reaction mediated through HSDs may be conducted by a minimum of two, distinct, isozymes (W. L. Miller & Auchus, 2011). HSDs lack heme groups and facilitate the interconversion of active and comparatively inactive versions of specific steroid hormones, utilizing nicotinamide cofactors NADPH/NADP+ and NADH/NAD+ (reduced/oxidized forms of nicotinamide adenine dinucleotide phosphate)(A. K. Agarwal & Auchus, 2005).

1.2.3 Regulation of Steroidogenic Pathways in the Ovary and Testis

Among the six main categories of steroid hormones, androgens, estrogens, and progestogens are mostly synthesized in the gonadal organs (W. L. Miller, 2013). Typically, organ-specific gene expression determines the steroid composition of each specialized organ.

The testis is designated to synthesize androgens from cholesterol (Flück & Pandey, 2014). To be more precise, the interstitial Leydig cells produce androgens in response to the pulsatile discharge of the pituitary gonadotroph, LH, which acts through the LH receptor on the surface of the Leydig cells and they synthesize androgens via two distinct routes, with the particular mechanism used depending on the species. For the most part, rodents possess the the Δ^4 pathway, which goes as follows: cholesterol → pregnenolone → progesterone → androstenedione → testosterone while, dogs, rabbits, pigs, humans, and higher primates all have the Δ^5 pathway, which goes as follows: cholesterol → pregnenolone → 17α-

hydroxypregnenolone(17OHPreg) → dehydroepiandrosterone(DHEA) → androstenedione → testosterone (Stocco & McPhaul, 2006) (Figure 7)

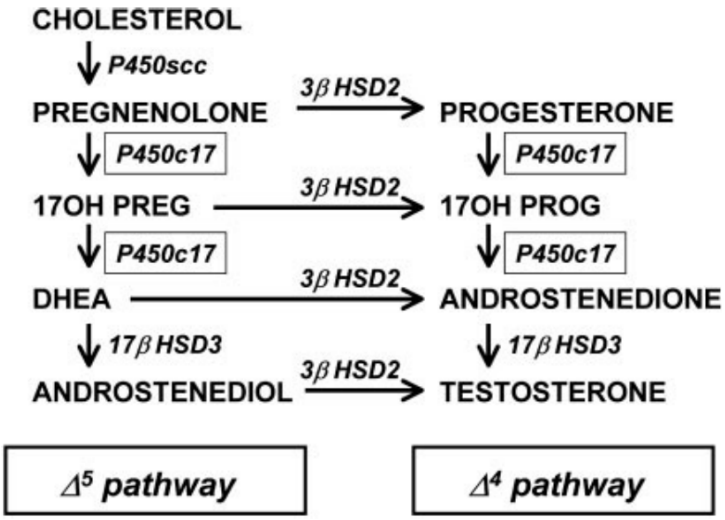

Figure 7. Potential routes of testosterone production in the human testis (Flück, Miller, & Auchus, 2003).

Gonadal steroidogenesis is a complex process that involves numerous enzymatic stages, as illustrated in Figure 8. The initial enzyme in the steroidogenic pathway, P450scc, is situated in the IMM; the other gonadal steroidogenic enzymes are found in the agranular endoplasmic reticulum; and lipid vesicles contain cholesteryl esters which serve as precursors for steroid hormone synthesis (Magoffin, 2005).

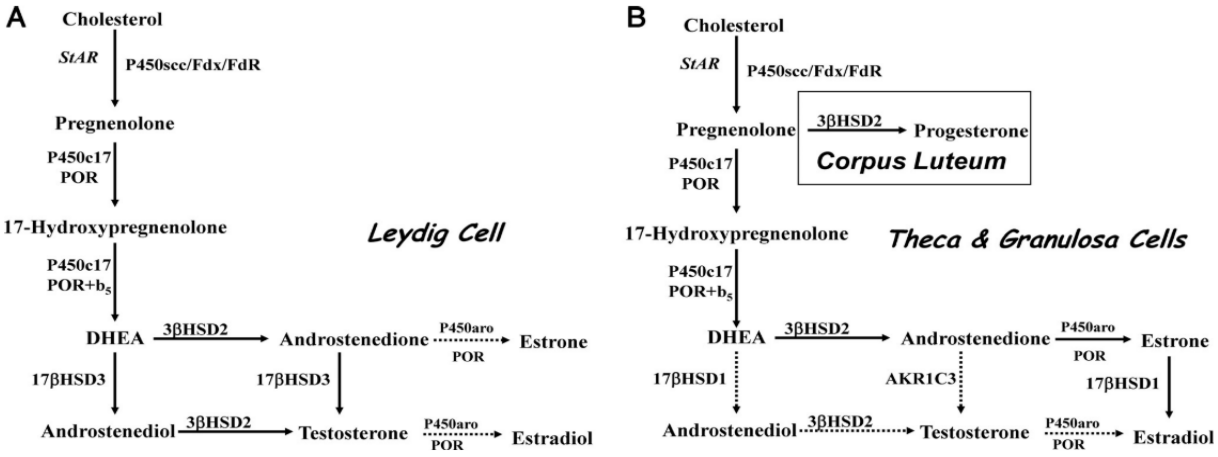

Figure 8. Main routes of gonadal steroidogenesis A. In testicular Leydig cells; B. In ovarian granulosa and theca cells (W. L. Miller & Auchus, 2011).

Following a translocation of cholesterol into the IMM by StAR, the mitochondrial side-chain cleavage system including P450scc, ferredoxin (FDX1), and ferredoxin reductase (FDXR) metabolizes it to pregnenolone (Kubeil, Yeung, Tuckey, Rodgers, & Martin, 2016; Strauss III, 2019). Cytochrome P450c17 enables both 17-hydroxylation and 17,20-lyase conversion of 21-carbon steroids into 19-carbon precursors of sex hormones. It may conduct testosterone production by converting pregnenolone to DHEA (the delta 5 route) or by converting progesterone to androstenedione (the delta 4 pathway) (Flück et al., 2003).

In the delta 5 route, CYP17A1 (P450c17) converts pregnenolone to 17OHPreg and DHEA. The first reaction is catalyzed via its 17-hydroxylase activity, which is facilitated by P450 oxidoreductase (POR), and the second reaction is catalyzed by its 17,20 lyase activity, which is facilitated by POR and cytochrome b5. DHEA is then converted to testosterone via intermediates such as androstenedione or androstenediol by 3β HSDII and 17β HSD3 (Flück & Pandey, 2014). The majority of testosterone produced by the human testis comes from the delta 5 route, which converts pregnenolone to DHEA. This pathway is chosen because the testicular P450c17 system has an enzyme with a catalytic capacity that is eleven times greater. (Flück et al., 2003).

Steroids produced by ovarian cells are estrogens, progesterone, and weak androgens. Estradiol is the principal steroid hormone produced by preovulatory granulosa cells, while progesterone, a precursor of androgens and estrogens, is created by the corpus luteum in the luteal phase. Theca interna cells generate weak androgens, namely DHEA and androstenedione (Abraham L. Kierszenbaum, 2019).

Ovarian steroidogenesis starts also with the conversion of cholesterol to pregnenolone. However ovarian steroidogenesis exhibits greater complexity resulting from the compartmentalization of enzymatic activity between granulosa and theca cells, along with differing steroidogenic patterns (estradiol predominates in the follicular phase, whereas progesterone becomes the primary product in the luteal phase) (W. L. Miller & Auchus, 2011). Granulosa cells and thecal cells have diverse responses to FSH and LH, exhibiting unique enzymatic capabilities to generate (thecal) or convert (granulosa) androgens into estrogens. This is the 'two-cell, two-gonadotropin' model presented by Armstrong et al (Hillier, Whitelaw, & Smyth, 1994) (Figure 9). The maximum synthesis of estrogen during the follicular phase of the menstrual cycle relies on the collaboration between theca cells, which can synthesize androgens de novo but lack the ability to

convert androgens into estrogens, and granulosa cells, that do not express the CYP17A1 necessary for androgen production but possess significant levels of aromatase and 17βHSD1 (Magoffin, 2005). During the luteal phase, 3β HSDII within the corpus luteum converts precursor pregnenolone into progesterone, the ultimate product (W. L. Miller & Auchus, 2011).

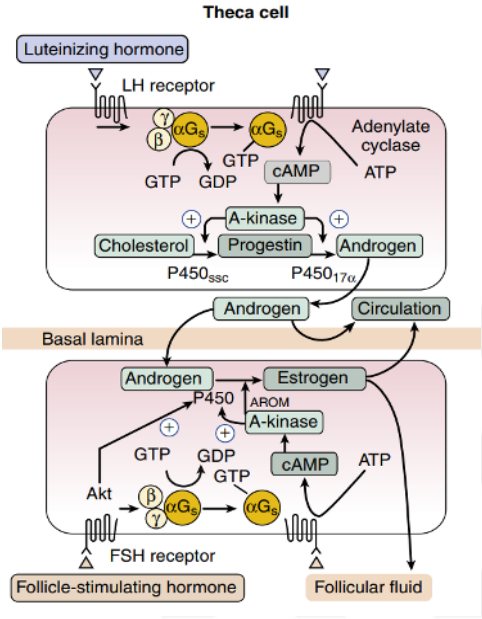

Figure 9. Illustration of the Two-Cell, Two-Gonadotropin Pathway in the Ovary (*Yen & Jaffe's Reproductive Endocrinology Physiology, Pathophysiology, and Clinical Management* 2019)

1.3 PARP Protein Family and DNA Repair Mechanisms

1.3.1 Overview of the PARP Protein Family

Poly (ADP-ribose) polymerase (PARP), mostly situated in the cell nucleus, is crucial for DNA damage repair and participates in many important cellular processes, including genomic stability, immunological response, transcription control, inflammation, and apoptosis (Wang et al., 2024). In all, seventeen forms constitute the PARP family in eukaryotic organisms, and they are all defined by sharing a conserved catalytic domain, which is homologous to the diphtheria toxin ART domain. (Langelier, Eisemann, Riccio, & Pascal, 2018) (Figure 10).

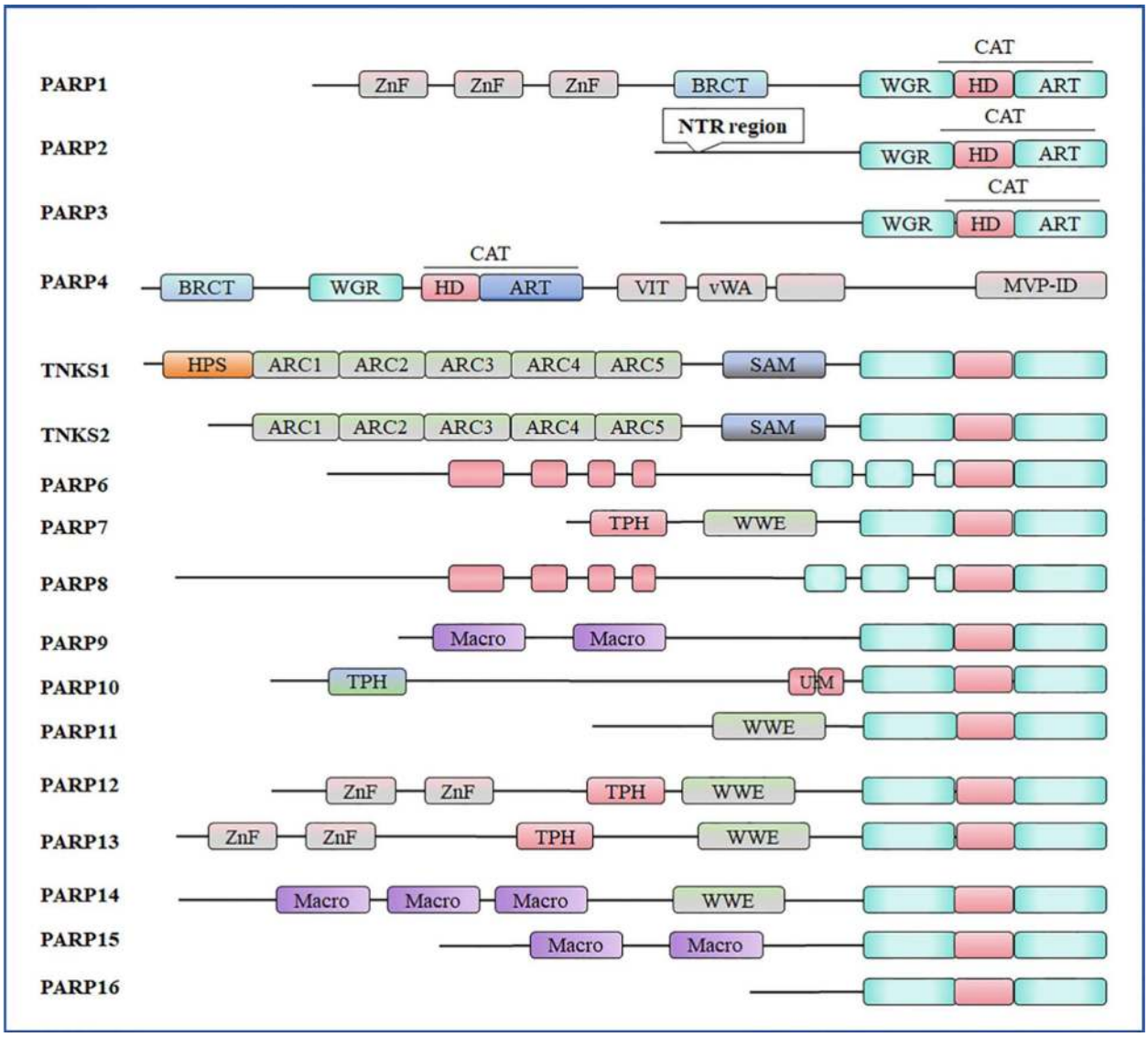

Figure 10. The PARP family is classified into DNA damage-dependent PARPs (PARP-1, PARP-2, PARP-3, essential for DNA repair), Tankyrases (TNKS1/TNKS2, implicated in cell signaling and telomere maintenance), CCCH PARPs (PARP-7, PARP-12, PARP-13, modulating immune response), Macro PARPs (PARP-9, PARP-14, PARP-15), and additional variants (Wang et al., 2024).

During the reaction catalyzed by PARP enzymes, nicotinamide adenine dinucleotide (NAD+) is hydrolyzed into ADP-ribose (ADPR) and nicotinamide; subsequently, conjugating one or more ADPR units to glutamate, aspartate, or lysine residues on acceptor proteins, a process referred to

as mono, oligo, or poly(ADP-ribosyl)ation (PARylation), depending on the quantity of ADPR units involved (Vida, Márton, Mikó, & Bai, 2017). The resultant polymer of ADP-ribose (PAR) is a linear or multibranched polyanion of varying size which selectively interacts with various protein targets implicated in the physiological response to DNA damage. Those protein targets possess a PAR-binding common pattern that often coincides with a functional domain, such as a protein- or DNA-binding domain. Therefore, PAR binding might modify the functional characteristics of its targets (Schreiber, Dantzer, Ame, & De Murcia, 2006). The breakdown of PAR is done by the enzyme poly(ADP-ribose) glycohydrolase (PARG) (Meyer-Ficca, Meyer, Jacobson, & Jacobson, 2005).

Of the 17 PARP family members, PARP-1, PARP-2, and PARP-5a/PARP-5b produce polymers of ADP-ribose, whereas the remaining PARPs induce mono ADP-ribose posttranslational modifications (Langelier et al., 2018). The predominant stimulated and baseline PARP activity is attributed to PARP-1 (85%–90%) and PARP-2 (10%–15%), whereas the involvement of other PARPs is minimal in relation to the overall activity (Szántó et al., 2012). PARP-1, the first identified and most prominent member of the PARP protein family is a multi-domain protein, and it contains multiple different regions. At the beginning, there is a DNA-binding domain with three DNA-specific zinc finger motifs. In the middle, there is a central auto-modification domain that contains a BRCT domain. Finally, at the end, there is a highly conserved catalytic domain that has WGR domain characterized by conserved tryptophan, glycine, and arginine residues (Figure 11). The catalytic domain includes the "PARP signature" sequence, which comprises a NAD+ acceptor site as well as many residues necessary for the initiation, elongation, and branching of PAR chains (Li, Li, Zhang, Zhang, & Dai, 2023). Collectively, these domains regulate the reaction of PARP1 to many forms of DNA damage.

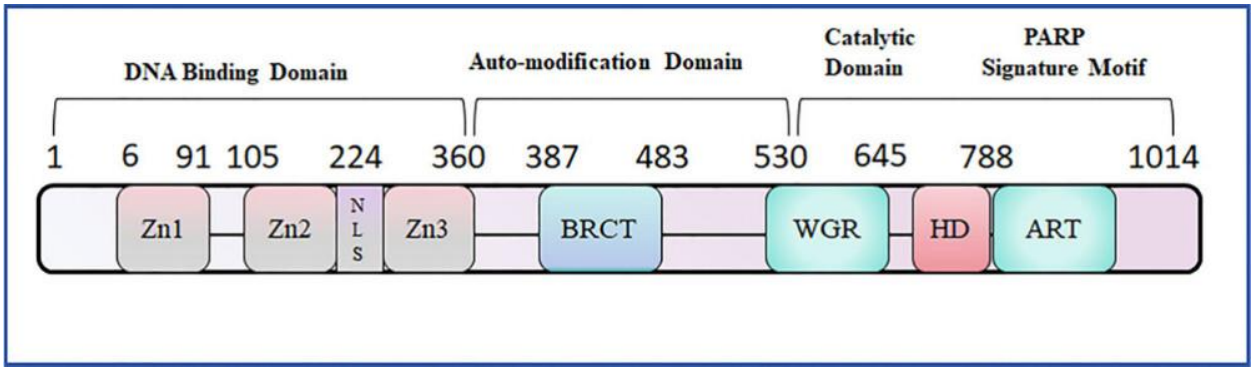

Figure 11. Configuration of PARP-1 (Wang et al., 2024).

PARP-1 and PARP-2 exhibit a high degree of similarity in their catalytic domains. However, PARP-2 has an extra three-amino-acid insertion in the loop linking the β-strands k and l seen in PARP-1. Moreover, PARP-2 conducts both hetero and auto PARylation of proteins.
PARP-1 is an extensively studied protein implicated in DNA repair mechanisms. So, its structural and functional similarity to PARP-2 indicates that PARP-2 may likewise be essential for preserving DNA integrity(Szántó et al., 2012).

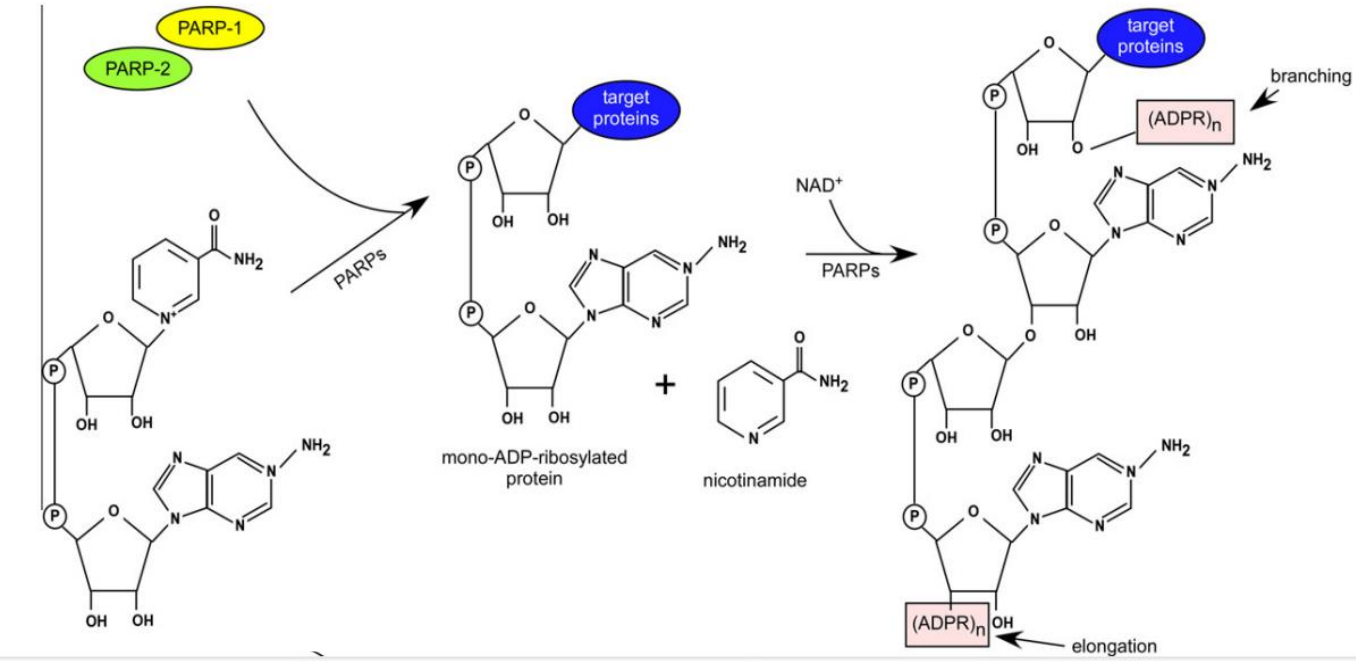

Figure 12. A summary of the mono- and poly(ADP-ribosyl)ation processes conducted by PARPs (Cantó, Sauve, & Bai, 2013).

1.3.2 Role of PARP in Single-Strand Break (SSB) Repair

DNA's structure may be destroyed in a variety of ways when exposed to chemicals or radiation. It is believed that each human cell's DNA undergoes thousands of damage daily (Lindahl & Barnes, 2000). DNA damage can disrupt replication and produce single-strand breaks(SSBs) or double-strand breaks (DSBs), resulting in chromosomal abnormalities (Marteijn, Lans, Vermeulen, & Hoeijmakers, 2014).
SSBs represent the most prevalent form of DNA damage. They are defined as interruptions occurring in one strand of the DNA double helix, and SSBs are usually caused by oxidative damage initiated by endogenous reactive oxygen species (ROS). Oxidative

attack on deoxyribose leads to hydrogen detachment and consequent sugar fragmentation. So, this series of events generates SSBs characterized by damaged ends, such as 3′-phosphoglycolate (3′-PG) or 3′-phosphate (3′-P). Furthermore, oxidized deoxyribose may indirectly facilitate the development of single strand breaks during the elimination of the corresponding nucleobase. This mechanism generates an oxidized abasic site, which is then cleaved by apurinic/apyrimidinic endonuclease 1 (APE1) during DNA base excision repair (BER) (Caldecott, 2022). Other kinds of BER responses might indirectly create SSBs as well. For example, upon the removal of a damaged base by a monofunctional DNA glycosylase, APE1 cleaves the sugar-phosphate backbone, resulting in a SSB intermediate. And if a bifunctional DNA glycosylase removes a damaged base, it generates a SSB at the 3′-side of the abasic site (Caldecott, 2020). Consequently, both monofunctional DNA glycosylases (by APE1 activity) and bifunctional DNA glycosylases enable the formation of SSBs during BER. Other forms of DNA excision repair, including ribonucleotide excision repair, mismatch repair, and nucleotide excision repair also indirectly cause SSBs. Although they operate autonomously and intrinsically reseal SSB intermediates, it is possible that SSBs may sometimes 'escape' and need to be recognized and repaired by single-strand break repair (SSBR) machinery (Caldecott, 2022). Ultimately, the erroneous or deficient operation of DNA topoisomerases could additionally lead to SSBs. These enzymes enable the resolution of topological constraints and torsional stress encountered during DNA transcription and replication by introducing DNA breaks to form cleavage complex intermediates (Caldecott, 2022). Yet, when cleavage complexes confront RNA or DNA polymerases or are situated near various DNA lesions, they may not resolve correctly. This failure leads to the stabilization of Topoisomerase I (TOP1) cleavage complexes, ultimately resulting in the formation of TOP1-linked SSBs (TOP1–SSBs) (Caldecott, 2008). Likewise, Topoisomerase II (TOP2) may create SSBs since it operates as a homodimer, with each subunit creating tightly aligned SSBs on opposing DNA strands during its routine role of transiently generating DSBs. Although the functions of these subunits are often well-coordinated, partial inhibition or dysfunction of one subunit might disturb this coordination, resulting in the creation of a failed SSB rather than a DSB (Caldecott, 2022).

Considering the remarkable daily onslaught of both endogenous and exogenous DNA damage, it is clear that cells must have evolved enzymes capable of repairing DNA irregularities and thus preserving genomic integrity (Tubbs & Nussenzweig, 2017).

SSBs originate from various sources, and the individual mechanisms for repairing SSBs from these different sources are described as sub-pathways of SSBR. Nevertheless, these repair mechanisms exhibit overlapping enzymatic pathways.

There are four main phases of the fast global SSBR way that fixes most SSBs: SSB detection, DNA end processing, DNA gap filling, and DNA ligation (Caldecott, 2022). And an essential primary sensor of SSBs in DNA is PARP-1 (Eustermann et al., 2015).

PARP-1 can rapidly detect and bind a variety of DNA strand break structures, including nicked and gapped single-strand breaks (Langelier et al., 2018). The binding to the DNA strand breaks activates the auto-modification function of PARP-1, promoting the transfer of DNA repair mechanisms to the damaged sites. Significantly, PAR generated by PARP-1 automodification functions as a ligand, that attracts PAR-binding factors, including histone variations and chromatin-remodeling enzymes. This function allows PARP-1 to control chromatin structure, specifically by adjusting chromatin compaction at areas of SSBs, thereby improving the accessibility and efficacy of the DNA repair mechanism (Langelier, Ruhl, Planck, Kraus, & Pascal, 2010). PARP1 regulates chromatin structure based on its activation status. In the absence of DNA damage, the existence of PARP1 in chromatin may enhance compaction, probably via PARP1 homodimerization. Upon activation, PARP1 facilitates chromatin decompaction, either directly via PARylation effects on chromatin structure and nucleosome stability or indirectly by attracting chromatin remodelers including SMARCA5/SNF2H/ISWI, CHD3/CHD4/NuRD, polycomb repressive complexes, SSRP1/FACT, and ALC1 (Caldecott, 2022). Matveeva and colleagues demonstrated that PARP1 inhibits RNAPII elongation and facilitates the recruitment of splicing factors to weak splice sites by modifying chromatin structure (Matveeva, Al-Tinawi, Rouchka, & Fondufe-Mittendorf, 2019). Thus, PARP1 activity might serve as a protective mechanism; nevertheless, excessive activation may result in adverse consequences. For instance, the extended PARP1 activity on DNA damage limits transcription recovery by enhancing the recruitment and activity of the ubiquitin-specific protease USP3. Because, high USP3 activity significantly diminishes the amount of monoubiquitinated histones, which are crucial for transcriptional control (Adamowicz et al., 2021). Correspondingly, the effect of PARP1 on chromatin structure at DNA breaks influences transcription control.

PARP-2 may also gather at the damaged area after DNA damage. However, it exhibits slower kinetics compared to PARP-1 and remains at the DNA damage foci for a longer duration (Szántó et al., 2012).

Another crucial function of PARP activity is the attachment of X-ray repair cross-complementing protein 1 (XRCC1), a molecular scaffold protein that engages with proteins involved in the SSBR mechanism (Caldecott, 2019). XRCC1 regulates SSBR by interacting with DNA polymerase β (Polβ) and DNA ligase IIIα (Lig3α) for strand filling and ligation. It additionally recruits end-processing enzymes, such as aprataxin (APTX) and polynucleotide kinase-3′-phosphatase (PNKP), to guarantee appropriate 3′-hydroxyl and 5′-phosphate ends at the repair site (L. M. Polo et al., 2019).

For XRCC1 complexes to be recruited to DNA damage sites, activation of PARP1 and PARP2 is crucial, and the central BRCT domain (BRCT1) is necessary for the PARP-dependent assembly of XRCC1 (Hanzlikova, Gittens, Krejcikova, Zeng, & Caldecott, 2017; L. M. Polo et al., 2019). The role of PARP activity in recruiting XRCC1 protein complexes is especially significant for direct SSBs, as these breaks arise unpredictably and randomly throughout the genome, requiring a quick and efficient detection and repair mechanism.

PARP function is likewise necessary for the repair of indirect SSBs that form as intermediates of base excision repair BER (Caldecott, 2022). PARP1 has been reported to be essential for efficient BER (Dantzer et al., 2000). However, some researchers claim that BER is not significantly influenced by the lack of PARP-1, and the principal function of PARP-1 in BER may not be related to the direct catalysis of DNA damage processing but rather to its involvement in linking repair mechanisms. In addition, the metabolic kinetics of BER can potentially be reduced by PARP1(Allinson, Dianova, & Dianov, 2003; Ström et al., 2011; Vodenicharov, Sallmann, Satoh, & Poirier, 2000).

PARP-2 was additionally proposed to actively participate in BER in conjunction with XRCC1. Supporting this, researchers have shown that PARP-2 deficient cells display a marked delay in the repair of DNA strand breaks, similar to the defect seen in PARP-1 deficient cells (Schreiber et al., 2002). A further study indicated a necessity for PARP2 in stabilizing replication forks that confront BER intermediates. While PARP2 is non-essential for cellular tolerance to SSBs or homologous recombination impairment, it is redundant with PARP1 in BER. Consequently, the simultaneous disruption of PARP1 and PARP2 results in impaired BER (Ronson et al., 2018).

However, it is noteworthy that, unlike direct SSBs, the requirement for PARP enzymes to recruit XRCC1 during BER is less apparent. As previously mentioned, scheduled intermediates of BER are generated by APE1 activity and are subsequently processed by DNA polymerase β for gap filling, followed by DNA ligase III for DNA ligation. In this context, Demin and colleagues demonstrated that protein complexes including DNA polymerase β and DNA ligase III, organized by XRCC1, are essential in modulating PARP1 activity during BER. The lack of these complexes causes PARP1 to interact with BER intermediates excessively in XRCC1-deficient cells, which ultimately leads to PARP1 being stuck to DNA. The efficacy of BER is reduced because the trapped PARP1 blocks the access of essential repair enzymes. As a result of this, inappropriate PARP1 involvement during BER poses a risk to genomic integrity and XRCC1 is recognized as an anti-trapper that inhibits hazardous PARP1 activity (Demin et al., 2021). Alternatively, it may be elucidated as the synchronized transfer of BER intermediates protects them from possibly harmful enzymes, such as PARP1. Nonetheless, if these intermediates detach from the BER machinery, PARP activity might be necessary to reestablish their appropriate engagement for effective repair (Caldecott, 2022).

Additional potential functions of PARP1 in SSBR might involve the repair of single-stranded DNA (ssDNA) nicks which arise from the incomplete action of TOP1. As previously stated, to reduce topological stress in DNA, TOP1 briefly nicks one strand, enables controlled rotation around the intact strand, and thereafter religates the nick. The complexes are subsequently removed from the DNA by tyrosyl-DNA phosphodiesterase 1 (TDP1). TDP1, a recognized target of PARP1, undergoes PARylation, which is crucial for stabilizing the enzyme and increasing its recruitment to TOP1cc. Consequently, this process enables the removal of TOP1cc from the DNA (Ray Chaudhuri & Nussenzweig, 2017).

PARP1 plays roles beyond SSB detection and DNA end processing, contributing to DNA gap filling and DNA ligation phases of the fast global SSBR. It stimulates long-patch gap filling by Pol β in vitro and facilitates ATP generation required for the final step of DNA ligation (Caldecott, 2008).

1.3.3 Role of PARP in Double-Strand Break (DSB) Repair

Failure to repair chromosomal SSBs presents a significant risk to genetic stability and cellular viability. For example, the obstruction of DNA replication forks in the S phase of the cell cycle

is the most probable outcome of unrepaired SSBs in proliferating cells. And this may cause the formation of DNA DSBs (Kuzminov, 2001). DSBs occur when both strands of the DNA helix are damaged. Independent of their origin, DSBs are very hazardous and may induce genomic rearrangements and cellular apoptosis (Chapman, Taylor, & Boulton, 2012). PARP1 acts as a sensor of DSBs, similar to its role in identifying SSBs. In the context of DSB repair, PARP1 is crucial for the prompt recruitment of repair elements to the site of damage. Its catalytic activity is important for activating subsequent repair pathways, therefore facilitating the effective resolution of DSBs (Ray Chaudhuri & Nussenzweig, 2017).

Researchers have demonstrated that the impaired synthesis of PAR in cells leads to delayed phosphorylation of structural maintenance of chromosomes protein 1(SMC1), p53, and histone variant H2AX, which are various proteins critical for the DNA damage response (DDR) and repair. This phenomenon can be elucidated as follows: Shortly after the induction of DNA damage, ataxia-telangiectasia mutated (ATM) kinase is recruited and activated at areas of DSBs. Significantly, to enhance ATM activity, the interaction of PAR with PAR-binding domains of ATM is required. Upon activation, SMC1, p53, and the histone variant H2AX are phosphorylated by ATM. Consequently, the lack or inhibition of PARP1 results in postponed activation of SMC1, p53, and H2AX following DNA damage (Haince et al., 2007). One year later, the same group noted that the quick aggregation of double-strand break sensors NBS1 and MRE11 at DNA damage sites necessitates PARP1. On the other hand, there may be additional pathways to facilitate the recruitment of ATM to the site of DSBs, as ATM substrate phosphorylation, although delayed in PAR-deficient cells, ultimately still occurs.
(Haince et al., 2008).

DSBs are repaired via two main mechanisms, these are homologous recombination (HR) and non-homologous end-joining (NHEJ) (Gupta et al., 2018). The selection of a pathway for repairing DSBs depends on the chromatin environment and cell cycle phase(Ray Chaudhuri & Nussenzweig, 2017) HR necessitates a homologous template for precise repair of post-replicative DSBs during the S and G2 stages of the cell cycle.

On the contrary, classical non-homologous end joining (C-NHEJ) does not need template DNA and may function at any point in the cell cycle (S. E. Polo & Jackson, 2011).

C-NHEJ has two separate phases: a quick phase that corrects small DNA lesions without end processing, and a slower phase that resolves complicated DSBs. The process starts with the

identification of DNA lesions by the Ku70/Ku86 complex, which then attracts the DNA-dependent protein kinase catalytic subunit (DNA-PKcs) to the site of damage. Activation of DNA-PK induces the phosphorylation of Artemis, facilitating its endonuclease function to handle 3′ and 5′ DNA overhangs. The XLF/DNA ligase IV/XRCC4 complex subsequently ligates simple lesions. Conversely, complex DSBs need further DNA end processing by enzymes like DNA polymerases μ and λ, flap endonuclease-1 (FEN-1), and polynucleotide kinase (PNK). These proteins guarantee repair with minimum modifications to the sequence at the junction (Caracciolo, Riillo, Di Martino, Tagliaferri, & Tassone, 2021).

Surprisingly, cells lacking PARP1 exhibit decreased HR repair and elevated NHEJ, indicating that PARP1 regulates the ratio between these pathways by recruiting the nuclease MRE11 to direct repair of DSB toward HR (Haince et al., 2008; Ray Chaudhuri & Nussenzweig, 2017). The Mre11/Nbs1/Rad50 complex (MRN) serves several functions in preserving genomic integrity, such as the recruitment and regulation of essential HR proteins. The quick and early recruitment of HR proteins is additionally facilitated by PARP1(Ray Chaudhuri & Nussenzweig, 2017). And, breast cancer type 1 susceptibility protein 1 (BRCA1) is the most crucial one, which is a big protein that has widespread expression. Its function is rigorously controlled by phosphorylation, sumoylation, and interactions with various other proteins (Bouwman et al., 2010).

BRCA1 operates throughout both the initial and afterward phases of HR. Subsequent to DSBs generation, BRCA1 is crucial in stopping the NHEJ factor 53BP1 to promote DNA end resection, an initial stage in HR. In the subsequent phase of HR, BRCA1 connects with the PALB2 protein, which then attaches to breast cancer type 2 susceptibility protein (BRCA2), causing RAD51 filament production. (C.-C. Chen, Feng, Lim, Kass, & Jasin, 2018). The production and recruitment of RAD51 to DNA is crucial for strand exchange in HR.

The absence of BRCA1 results in chromosomal instability and cancer progression resulting from the failure to induce proper repair of DSBs (Bouwman et al., 2010). Yet, some observations suggest that enhanced BRCA1 activity and/or inadequate regulation of this activity is linked to genomic instability as well (Hu et al., 2014). This can be seen in various cases. For instance, researchers have demonstrated that the loading of RAD51 and sister chromatid exchange (SCE) occurrence in response to replication arrest are enhanced by PARP-1 loss. It indicates that a lack

of PARP-1 results in increased recombination activity (Y.-G. Yang, Cortes, Patnaik, Jasin, & Wang, 2004).

In addition, a different study concluded that PARP1 limits BRCA1's functionality in the HR pathway by promoting RAP80 binding to BRCA1 via PARylation of BRCA1. According to all of these studies, PARylation regulates BRCA1 DNA binding activity, which is essential for proper HR control and inhibiting the emergence of a hyper-HR mode.

Earlier studies in PARP-2−/− cells coupled with Atm deficiency suggested that the cell's ability to defend itself against DNA damage was severely compromised (Huber, Bai, De Murcia, & De Murcia, 2004). This fact indicates that PARP-2 also has a role in the repair of DSBs during replication.

Alongside HR and C-NHEJ, several error-prone DNA repair pathways may be activated when these essential pathways are impaired. These alternate mechanisms, generally known as alternative non-homologous end joining (Alt-NHEJ), are involved in the repair of DNA damage but have been linked to increased genomic instability, which may facilitate cancer progression (Caracciolo et al., 2021). In contrast to C-NHEJ, Alt-NHEJ conducts independently of Ku proteins and DNA ligase IV (Kent, Chandramouly, McDevitt, Ozdemir, & Pomerantz, 2015). Researchers supported that PARP1 and the MRN proteins participate in the Alt-NHEJ pathway, whereas Ku proteins serve as the primary antagonist to the recruitment of PARP1 and the MRN complex to broken chromatin. Furthermore, Ku proteins restrict PAR synthesis. So, a decrease in Ku proteins inside cells prompts a transition from C-NHEJ to Alt-NHEJ (Cheng et al., 2011). Another function of PARP1 in Alt-NHEJ is to facilitate the recruitment of Polθ to DSBs, a process that is essential for the Alt-NHEJ-dependent repair of DSBs in mammalian cells (Ceccaldi et al., 2015). Besides its established function in Alt-NHEJ, PARP1 also facilitates effective KU-dependent C-NHEJ in human cells by recruiting the chromatin remodeller chromodomain helicase DNA-binding protein 2 (CHD2). CHD2 subsequently initiates quick chromatin expansion, the deposition of histone variant H3.3 at DNA damage sites, and the effective operation of C-NHEJ repair complexes (Luijsterburg et al., 2016). An additional chromatin remodeller that is brought to DSBs in a PARP1-dependent manner is SMARCA5/SNF2H. Researchers demonstrated that SMARCA5 and RNF168 interact in PARP-dependent manner on sites of DSB, and the depletion of SMARCA5 compromised NHEJ to the same degree as XRCC4 knockdown. Consequently, their findings strongly indicate that the

recruitment of SMARCA5 by PARP1 facilitates DSBs repair through NHEJ (Smeenk et al., 2013). Alongside chromatin remodelers, NR4A proteins, which are orphan members of the nuclear receptor family functioning as ligand-independent transcription factors, are moved to DSB foci through a mechanism that necessitates the activity of PARP-1, following DNA damage. At DNA repair foci, NR4A proteins undergo phosphorylation by DNA-PK, enhancing DSB repair (Malewicz et al., 2011).

Lastly, to repair DSBs accurately, transcription needs to be blocked at the repair sites and PAR acquires transcription repression complexes to DNA damage sites in order to restrict transcription there (Ray Chaudhuri & Nussenzweig, 2017).

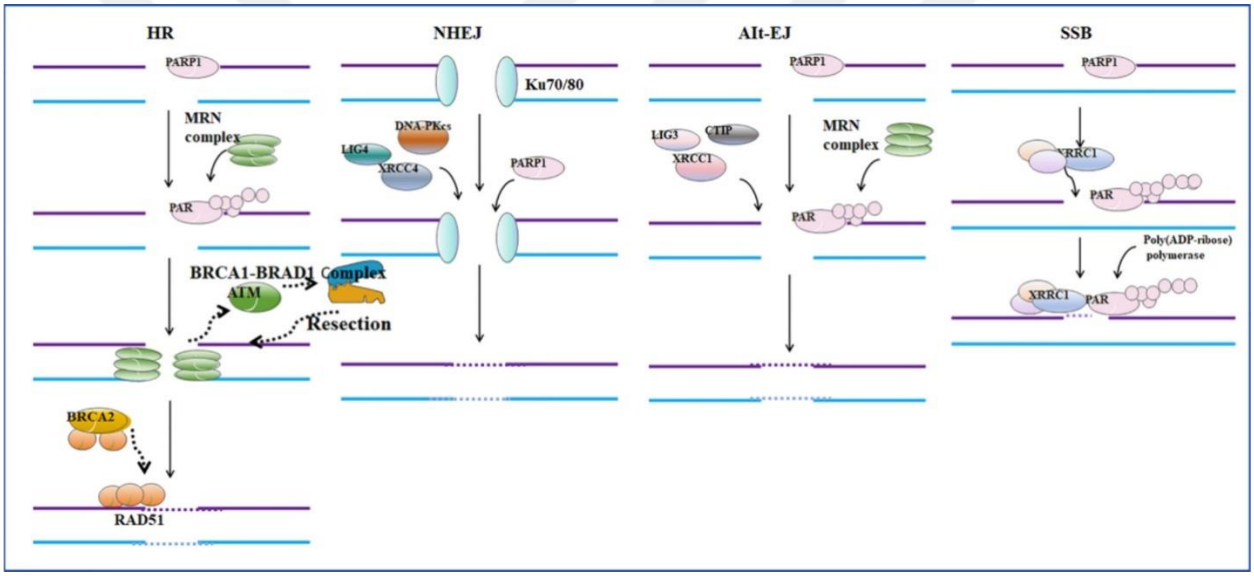

Figure 13. Schematic summary of the essential functions of PARP in DNA repair (Wang et al., 2024).

1.4 Functions of PARP in Ovary and Testis

1.4.1 Functions of PARP on Female Reproductive Function

In females, as mentioned before, the full complement of gametes is generated throughout fetal development; beyond this point in time, no more oocytes will be produced. Therefore, the repair of damaged oocytes is likely a critical mechanism to assure that the ovary maintains an adequate number of primordial follicles to promote the species' continuation and fertility (Stringer, Winship, Liew, & Hutt, 2018). Despite the fact that oocytes within primordial follicles are more

susceptible to DNA damage compared to somatic cells, they are able to conduct effective DNA repair (Li et al., 2023). From the primordial to the secondary follicle stages, PARP1 has been observed in the nucleus of oocytes during follicular development. Additionally, PARP1 is expressed in a large proportion of granulosa cells throughout the post-primary follicle stages(Qian, Xu, Lalioti, Gulle, & Sakkas, 2010). A recent research indicates that PARP1 in granulosa cells serves as a crucial regulator of primordial follicle destiny, since its inhibition minimizes the depletion of the primordial follicle reserve by reducing excessive endoplasmic reticulum stress in granulosa cells exposed to fetal bisphenol A (W. Chen et al., 2023).
It had been shown in a study by Yang and colleagues that, during prophase I of meiosis, half of Parp-1 null oocytes display a variety of chromosomal anomalies, especially the presence of aberrant chromatin modifications with a form of persisting H2AX phosphorylation in fully synapsed bivalents, or defective homologous chromosome synapsis. Significantly, a high percentage of Parp-1 null oocytes that developed in vivo exhibit inadequate sister chromatid cohesion during metaphase II, resulting in the early commencement of anaphase II following removal from the oviductal environment. Moreover, without functioning PARP-1 protein, the completely synapsed X chromosome bivalent is susceptible to persisting DSBs at the pachytene stage. Their findings together demonstrate that PARP-1 is essential for maintaining chromosomal integrity throughout crucial phases of meiosis in the female germ line (F. Yang, Baumann, & De La Fuente, 2009). Remarkably, Makogon and colleagues has demonstrated that PARP might play a role in immune-mediated ovarian damage. Their findings rely on observations from previous studies: PARP activation had been shown to exacerbate tissue damage in several types of inflammation. A potential mechanism of PARP-mediated tissue injury involves a functional connection between PARP and proinflammatory transcription factors (Makogon et al., 2010). It had been already shown that PARP-1 activity is crucial for the upstream control of Ionizing radiation-induced NF-κB activation (Veuger, Hunter, & Durkacz, 2009). Moreover, exposure to gamma radiation augmented ovarian visfatin mRNA expression, which synthesizes NAD+, subsequently consumed by the overexpression of PARP-1, resulting in the depletion of NAD+ reserves. This depletion inhibits SIRT1 activity, thereby alleviating SIRT1's repression of NF-κB, ultimately promoting an increase in proinflammatory cytokine production. In contrast, Resveratrol administration suppresses inflammatory signaling linked to ionizing radiation-induced premature ovarian failure by enhancing the expression of PPAR-γ and SIRT1, which in

turn restricts the production of PARP-1 and NF-κB-mediated inflammatory cytokines in rats (Riham Soliman Said, El-Demerdash, Nada, & Kamal, 2016). The same research group afterwards showed that Resveratrol secures the ovary from harmful effects of cisplatin by reducing PARP-1 expression, decreasing the inflammatory and apoptotic processes associated with cisplatin toxic impacts and preserving AMH-secreting granulosa cells (Riham S Said, Mantawy, & El-Demerdash, 2019). Corroborating these results more recent work by (Alharbi, Alshehri, Ahmad, & Guo, 2021) indicated that Resveratrol repairs ovarian function by elevating AMH levels and reducing ovarian inflammation in rat model of premature ovarian failure, mostly via the regulation of PARP-1 and the suppression of inflammatory cytokines. PARylation has roles in mammalian oogenesis and folliculogenesis. Suppressing PARylation resulted in a substantial rise in the quantity of oocytes in prepubertal and pubertal females, as well as an elevated number of fetuses (this effect disappeared with the lack of PARP1), in addition simultaneously enhancing the expression levels of various ovarian-specific genes, especially those belonging to the TGF-beta family, which might lead to raised folliculogenesis and oogenesis (Qian et al., 2010). Findings from research by (Dang et al., 2018) revealed that granulosa cells from patients with biochemical premature ovarian insufficiency had substantially increased levels of miR-379-5p, which inhibited proliferation of cells and compromised DNA repair activity by directly targeting PARP1, that had been downregulated in the same group of patients.

Additionally, there have been studies that suggest that PARP might indirectly affect steroidogenesis. The DNA-binding domain of the progesterone receptors has been linked with PARP in human (Sartorius, Takimoto, Richer, Tung, & Horwitz, 2000). Luteal progesterone plays a role in both the repair of genomic lesions and the apoptotic clearance of sheep ovarian surface epithelial cells with DNA damaged after ovulation, by increased PARP activity (Murdoch, 1998). Moreover, the formation of transient DNA breaks by the TopoIIb/PARP-1 complex is essential for gene activation in response to estradiol (Ju et al., 2006).

1.4.2 Functions of PARP on Male Reproductive Function

Extensive evidence demonstrates the existence of PARP and its homologs in testicular germ line cells, suggesting their activity may play a crucial role in maintaining DNA integrity during spermatogenesis, yet there is a probable involvement of PARP overactivation in oxidative stress-induced male reproductive diseases (Celik-Ozenci & Tasatargil, 2013). The role of PARylation in DNA repair has been examined in rat spermatocytes and spermatids by (Atorino, Di Meglio, Farina, Jones, & Quesada, 2001). Subsequent work by the same group revealed, both mRNA and protein investigations have shown that PARP-1 is highly expressed within primary spermatocytes, especially during the pachytene stage of meiosis. Moreover, both the 110 and 60 kDa isoforms of PARG have been identified in rat germ cells. Overall, these findings emphasize the significance of poly(ADP-ribose) turnover across several paths throughout meiotic and post-meiotic germinal cell development (Di Meglio, Denegri, Tramontano, Scovassi, & Quesada, 2003). The temporary activation of PARP and the resulting production of PAR have been associated with assisting in the control of DNA strand breaks at the chromatin remodeling phases of spermiogenesis in rats (Meyer-Ficca, Scherthan, Bürkle, & Meyer, 2005). A subsequent study by the same research group revealed that knockout mice lacking PARP1, PARG (110-kDa isoform), or both exhibit functional and morphological sperm defects depending upon their specific genotypes, involving remaining DNA strand breaks linked to various degrees of subfertility (Meyer-Ficca et al., 2009). In a different context, PARP-1 overactivation has been associated with abamectin-induced oxidative stress, which in turn results in testicular damage (Celik-Ozenci et al., 2011). In line with their earlier findings, the same investigators showed that doxorubicin-induced testicular damage and attenuated sperm motility in mice are closely linked to oxidative stress and subsequent PARP-1 overactivation. (Gungor-Ordueri et al., 2019). Besides PARP1, PARP2 also has been demonstrated to be crucial in spermatogenesis, as male mice deficient in PARP2 had exhibit hypofertility due to anomalies in meiosis I and spermiogenesis (Dantzer et al., 2006). Significantly, PARP2 gene has been linked to azoospermia in humans through meiotic arrest (Sakugawa et al., 2009). In mouse spermiogenesis, PARP1 and PARP2 both regulate TOP2B function during chromatin condensation (Meyer-Ficca et al., 2011). However, as reported by Schreiber and colleagues, PARP-1 and PARP-2 display divergent expression patterns in the testis: PARP-1 is highly expressed, especially in the basal layers of the seminiferous tubules of the developing testis, while no signal is observed in the luminal layers of the seminiferous epithelium, signifying a

reduction of PARP-1 levels at the haploid stage of meiosis. Conversely, the PARP-2 signal is modest and somewhat uniform across the seminiferous tubules and interstitial tissue in the mouse (Schreiber et al., 2002). Another research indicates that PARP-1 is the principal source of PAR production within isolated rat primary spermatocytes, alongside both the enzyme and histone proteins acting as covalent PAR recipients, while a negligible fraction of freshly synthesized PAR was seen to be covalently attached to PARP-2 (Tramontano, Malanga, & Quesada, 2007).

In humans, PARP-1 and PARP activity, as shown by PAR production, were primarily located in testicular germ line cells rather than in somatic testicular cells at certain phases of spermatogenesis, and linked to chromatin modifications (Maymon et al., 2006). Following these findings, more research has shown that PARP-1 and PARylation have many functions during spermatogenesis. They not only protect genomic integrity by repairing DNA and remodeling chromatin, but they also help with apoptotic and cytoplasmic remodeling. Their expression and activity change depending on the stage of spermatogenesis and the age of a person. Furthermore, sertoli cells have also been shown to express PARP-1 and PAR (El-Domyati et al., 2009). Notably, human ejaculated spermatozoa have been shown to contain the PARP homologues PARP-1, PARP-2, and PARP-9, and lower levels of these proteins may damage sperm maturity, which could affect male fertility. Additionally, PARP-1 and PARP-2 are thought to protect the sperm that is ejaculated, especially after it has been exposed to oxidative stress and apoptosis inducers (Jha et al., 2009). It is important to note that high levels of PARP expression have been observed in mature spermatozoa and in proven fertile men, while there have been higher levels of cleaved PARP (cPARP) in the sperm of infertile men (A. Agarwal et al., 2009).

1.5 Overview of PARP Inhibitors

1.5.1 Mechanism of Action

Long ago, it has been shown that small molecule nicotinamide analogues might prevent PARylation (Purnell & Whish, 1980). Following drug discovery initiatives resulted in the creation of clinical PARP1/2 inhibitors (PARPi), such as Olaparib (KuDOS/AstraZeneca) and Niraparib (Merck/Tesaro). The long-standing work to develop PARPi was motivated by a comprehension of the functions of PARP1 and PARP2 in DNA damage response. The initial

thinking behind PARPi was that it might render tumor cells more vulnerable to DNA-damaging traditional therapies, such as the several forms of chemotherapy and radiation that are still the mainstay of cancer management (Lord & Ashworth, 2017).

PARPi were considered to exert their anticancer effects as catalytic inhibitors that hinder DNA SSB repair. On the other hand, it was demonstrated that PARPi also trap the PARP1 and PARP2 enzymes in sites of SSBs. Moreover, trapped PARP–DNA complexes exhibited more cytotoxicity than unrepaired SSB resulting from PARP inactivation, suggesting that PARP inhibitors function, in part, as toxins that immobilize the PARP enzyme on DNA (Murai et al., 2012). From a mechanistic standpoint, PARP trapping is not separate from but rather connected to catalytic inhibition of PARylation (Pommier, O'Connor, & De Bono, 2016). A concise reminder of the PARP family's function is presented to enhance contextual understanding. PARP protein family's main role is to produce PAR chains by utilizing NAD+ as a substrate (Vyas et al., 2014). PAR possesses a net negative charge which supports the recruiting of proteins involved in DNA repair and aids in the elimination of PARP1 from DNA damage sites. PARPi imitate the nicotinamide component of NAD+, resulting in blocking auto modification and the removal of the enzyme from the DNA damage site (Kummar et al., 2012). Therefore, until PARPi separates from the active site, PARP1 and PARP2 will be trapped to the DNA (Pommier et al., 2016).

In cell-free systems built from recombinant proteins, the PARP inhibition efficacy and the capacity to trap PARP of Olaparib and niraparib are alike (Sun et al., 2018). Along cultured tumor cells, the efficacy of PARP trapping exhibited considerable variation across inhibitors, with niraparib showing superior trapping capability compared to olaparib (Murai et al., 2012). Chornenkyy and colleagues consistently demonstrated that niraparib was superior than olaparib in diminishing cell viability and suppressing proliferation (Chornenkyy et al., 2015). Furthermore, the S-phase-specific γH2AX signal, suggestive of DNA damage, elicited by niraparib was shown to be more prominent than that generated by Olaparib (Michelena et al., 2018). The higher cytotoxicity of niraparib identified in research studies might be attributed to the differing cell membrane permeabilities of the two medicines, since the apparent permeability coefficient of niraparib exceeds the coefficient for Olaparib. Besides its limited permeability, olaparib has also poor solubility in water-based solutions (Sun et al., 2018). Olaparib and

niraparib vary also in their chemical structures, which express differences in flexibility and overall size(Figure 14) (Pommier et al., 2016).

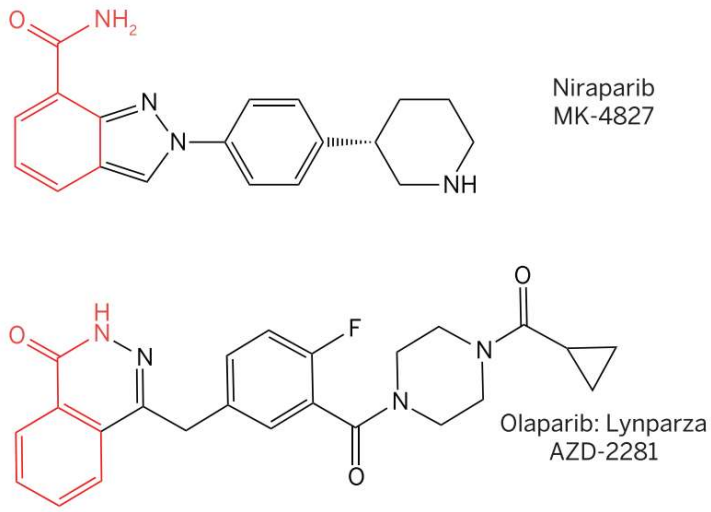

Figure 14. Structures of the PARPi (Pommier et al., 2016).

In short, the primary mechanisms of action of PARPi include the blocking of SSB repair and the entrapment of PARP–DNA complexes at the replication fork, eventually leading to the induction of DSBs. The first mechanism is further specific to HR deficit. However, other mechanisms of action of PARPi, such as the exacerbation of error-prone C-NHEJ and the collapse of replication forks, are also present (Konstantinopoulos & Matulonis, 2018).

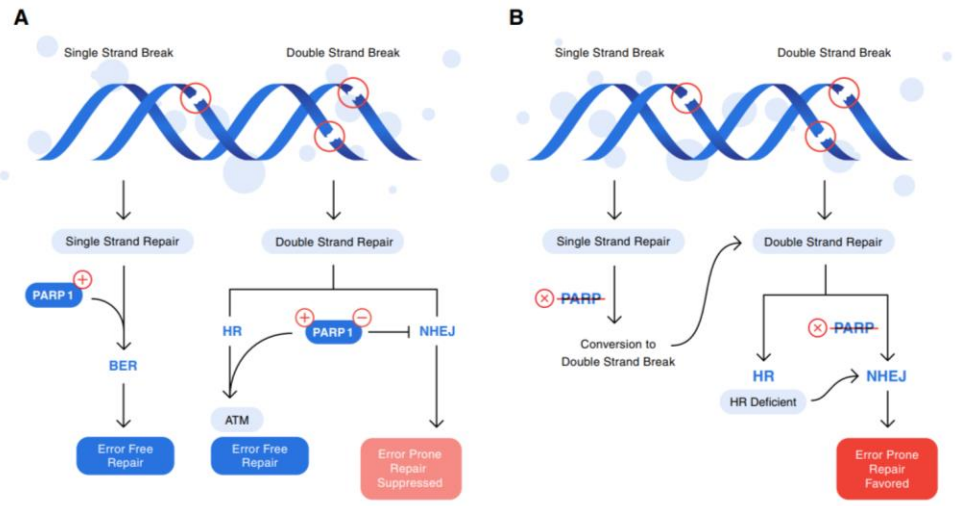

Figure 15. PARP Function in Genomic Integrity and DNA Repair (A) If the PARP activity is functioning, SSBs in DNA are fixed by BER, an error-free process and DSBs in DNA are resolved by HR, an error-free mechanism facilitated by the activation of PARP, which in turn activates the DNA damage kinase ATM protein. Concurrently, PARP inhibits error-prone pathways of DSB repair to preserve genomic integrity. (B) Once PARP function is compromised, SSBs in DNA are transformed into DSBs in DNA, and the inhibition of error-prone DSB repair processes is removed. Furthermore, if HR is also damaged (e.g., due to BRCA 1/2 mutations or other HR abnormalities), DNA repair proceeds via error-prone pathways, resulting in genomic instability and cellular apoptosis (Cook & Tinker, 2019).

Healthy cells may avoid the impairment resulting from PARPi by employing effective HR. However, DSBs are accumulated resulting from PARPi in HR deficit cells (such as those with BRCA and PALB2 mutations), and that eventually results in genomic instability and cell mortality (Figure 15). That is to say, although the inhibition of PARP activity alone does not pose a threat to cell viability, and HR deficiency is not fatal alone, their combined dysfunction impairs essential DNA repair mechanisms. (Cook & Tinker, 2019). This phenomenon can be illustrated by the principle of synthetic lethality, which is a gene interaction where one of two genetic abnormalities allows for cell survival, but the simultaneous dysfunction of both genes leads to cell death (Ashworth, Lord, & Reis-Filho, 2011). Synthetic lethality has attracted considerable interest as a potential approach for cancer therapy development. This method depends on a context-specific process, whereby a genetic modification—like a mutation in a tumor suppressor gene—renders another gene crucial for the survival of the affected cells. In this setting, pharmacological inhibition of the second gene's product may selectively eliminate tumor cells while safeguarding healthy, nonmalignant cells. So, synthetic lethality exploits the distinctive vulnerabilities of cancer cells, providing a targeted therapeutic strategy that minimizes damage to normal tissues, thus delivering a more precise and patient-centered treatment plan (Ashworth & Lord, 2018).

The first clinically authorized medicines to exploit synthetic lethality are PARPi. In 2005, two groups elucidated the synthetic lethal interaction between PARP inhibition and mutations in BRCA1 or BRCA2, proposing a potential therapeutic choice for patients with BRCA-mutant

malignancies. BRCA1 and BRCA2 are regarded as classical tumor suppressors since the wild-type BRCA allele disappears throughout tumor progression. (Lord & Ashworth, 2017). Heterozygous germline mutations in these genes significantly raise the risk of developing malignancies such as ovarian, breast, prostate, and pancreatic cancer. As previously stated, the proteins encoded by BRCA1 and BRCA2 are essential for the repair of DSBs through HR. A somatic elimination of the leftover functional BRCA allele is frequently observed in tumors of individuals with germline BRCA mutations. As a result, this situation causes defective HR repair. Thereby, the synthetic lethality seen between PARP inhibition and BRCA failure results from the buildup of unrepaired DSBs and, or the collapse of replication forks. Eventually, it is important to point out that preclinical studies of BRCA-mutant malignancies demonstrated a significant synthetic lethal impact, which served as a solid basis for the progress of this treatment approach into clinical studies (Ashworth & Lord, 2018).

1.5.2 Clinical Uses

PARPi for the management of solid tumors have been studied for a long time. The significance of BRCA1/2 mutation status was expected according to the drug's mechanism of action, and the influence of platinum sensitivity and responsiveness in forecasting treatment efficacy quickly became apparent. (Cook & Tinker, 2019). A phase 1 clinical study of olaparib had been established for patients with germ-line BRCA1 or BRCA2 mutations. A therapeutic advantage was seen in sixty-three percent of patients with germ-line BRCA1 or BRCA2 mutations, providing additional support for the synthetic lethality concept (Lord & Ashworth, 2017).
In 2014, the European Medicines Agency (EMA) authorized Olaparib as the first PARP inhibitor. In vivo, olaparib demonstrates monotherapy efficacy in BRCA1-deficient and BRCA2-deficient cells but exhibits reduced effectiveness in wild-type ovarian and/or breast cancer models. It was first approved for the maintenance treatment of germline or somatic BRCA1/2 mutated patients with platinum-sensitive, relapsed ovarian cancer (Bruin, Sonke, Beijnen, & Huitema, 2022). In study 19, Olaparib maintenance therapy demonstrated a positive overall survival result and an exceptional long-term benefit, regardless of BRCA1/2 mutation status, in patients with platinum-sensitive recurrent ovarian cancer (Friedlander et al., 2018). In light of the outcomes of this study, by 2018, Olaparib was authorized to be administered for platinum-sensitive, relapsed, high-grade serous ovarian cancer irrespective of BRCA mutation status.

Subsequently, indications were extended to include maintenance treatment or treatment for breast, prostate, and pancreatic cancers harboring specific mutations. Niraparib therapy in vivo led to tumor regression in both BRCA-1 mutant and BRCA wild-type mice xenograft models. And, it was authorized by EMA in 2017 for the maintenance therapy of recurrent, high-grade epithelial ovarian cancer that is platinum-sensitive, independent of BRCA mutation status (Bruin et al., 2022).

1.6 Effects of PARP Inhibitors on Reproductive Function

The impact of PARPi on reproductive function is still unclear. Qian and colleagues demonstrated that, the blocking of PARylation by 5-aminoisoquinolinone resulted in a significant increase in oocyte counts and a marked rise in primordial follicle numbers, accompanied by heightened expression of key genes and pathways in mice ovaries, especially members of the transforming growth factor superfamily (Qian et al., 2010). The treatment of 4-HQN (PARP-1 inhibitor) to mice infected with gram-negative bacteria improved oocyte meiotic maturation and demonstrated a substantial cytoprotective impact. Moreover, 4-HQN promoted cell viability by reducing necrosis and apoptosis in granulosa cells, while enhancing mRNA expression levels of HAS2, COX2, and GREM1 in cumulus cells (Kondratska et al., 2021). In support of these findings, treatment with the PARPi, 3–aminobenzamide (3–ABA), effectively prevented meiotic maturation impairment, cell death, and inflammation in mice (Makogon et al., 2010). Nonetheless, the same therapy (3–ABA) to embryos was shown to inhibit the growth of porcine blastocysts (Lee et al., 2016). These results are in line with the observations of (Kim et al., 2017) which indicates that 3-ABA treatment diminished developmental rates, compromised parthenogenetic embryo quality, and cumulus cell growth via atypical alterations in the expression levels of maturation- and expansion-related genes in porcine. Another PARPi, Olaparib, therapy resulted in reduced estradiol synthesis and expression of granulosa cell markers, along with aberrant granulosa cell shape in vitro. Moreover, it caused follicular atresia both in vitro and in vivo, lowered oocyte production and fertilization rates in In Vitro Fertilization (IVF), but these effects were reversible after a 3-week withdrawal of the medication in mice (Nakamura et al., 2020). A related study, which specifically investigated the effects of olaparib on mice ovarian tissue demonstrated that olaparib substantially reduced primordial follicles by 36% in comparison to the control group, nevertheless, it did not affect other follicle

categories, estrous cycling, corpus luteum number, or serum AMH level. The DNA damage indicated by γH2AX foci was entirely undetectable in the primordial follicles of control animals; however, this phenomenon was observed in 10% of the surviving primordial follicle oocytes in mice treated with olaparib alone. Yet, Olaparib did not exacerbate chemotherapy-mediated follicle depletion in the wild-type mice ovary (Winship et al., 2020). Additionally, one of the new research revealed that enzymatically inactive PARP1 induces genome instability and embryonic lethality in a dominant-negative manner, obstructing DNA repair in specific pathways beyond wild-type PARP1, thereby establishing a significant physiological distinction between PARP1 inactivation and deletion (Shao et al., 2023). The vascular and stromal microenvironment is essential for ovarian function (Li et al., 2023). Thus, the results of such studies that examine the influence of PARPi on vascular and stromal function are crucial for a thorough comprehension of its overall effect of PARPi on ovarian function. The PARPi GPI 15427 was shown to reduce angiogenesis in vivo (Tentori et al., 2007). On the other hand, the function of PARPi in lowering fibrosis progression in essential organs, such as the heart, lungs, kidneys, and liver has been reviewed (Rao et al., 2020). Disruption of follicular angiogenesis leading to insufficient development is probably linked to some forms of infertility (Fraser, 2006). Moreover, ovarian fibrosis compromises ovarian function, obstructing oocyte development and the initiation of ovulation, therefore significantly impacting female fertility (Gu, Wang, & Yu, 2024). Hence, the influence of PARPi on ovarian function may be in both directions as a result of its diverse effects on ovarian stromal and vascular functions. Overall, PARPi may also influence fertility through alternative mechanisms in addition to its effect on ovarian function (Li et al., 2023).

The literature contains an absence of studies that examine the influence of PARPi on testicular activity. Following PARP inhibition with 3–ABA worsened the reduction in embryo survival linked with sperm cryopreservation; however, embryos generated from fresh sperm did not exhibit any substantial adverse effects of 3-ABA in Misgurnus fossilis (Kopeika, Kopeika, Zhang, Rawson, & Holt, 2004). The administration of PARPi , such as 3-ABA or luminol, in rats has been shown to prolong the recovery duration of DNA repair in spermatocytes and spermatids, but spermatids exhibit greater sensitivity to PARP inhibitors compared to spermatocytes (Atorino et al., 2001). Research by Mahfouz et al indicates that sperm damage caused by staurosporine (STS) in the lack of PARP inhibition mostly increased the percentage of

early apoptotic sperm. Surprisingly, PARP inhibition reduces this early apoptotic response but concurrently causes a more than twofold rise in the proportion of late apoptotic sperm, especially in fractions of immature sperm. On the other hand, PARP inhibition under oxidative stress significantly raises early apoptosis, particularly in mature sperm cells, suggesting that under stress, too much PARP activation could accelerate the path toward late-stage apoptosis and necrosis (Mahfouz et al., 2009).

Additionally, pharmacological PARP blocking demonstrated an enhancement TOP2B activity in murine spermatids in vivo, indicating a functional correlation between the DNA strand break-inducing activity of TOP2B and the DNA strand break-dependent activation of PARP enzymes, which subsequently inhibit TOP2B (Meyer-Ficca et al., 2011). Of note, the pharmacological suppression of PARP-1 overactivity with PJ34 has been reported to avoid oxidative stress and cell apoptosis in testicular tissue generated by doxorubicin via reducing both mitochondria-dependent and -independent apoptotic pathways (Gungor-Ordueri et al., 2019).

In a study investigating the role of PARP1 during embryo implantation, PARP1 inhibition by drug EB-47 was found to reduce the quantity of blastocysts and embryo implantation sites in mice (Joshi et al., 2014).

1.7 Research Aims and Significance

Despite a significant rise of clinical applications and authorized indications for PARP inhibitors in recent years, their possible gonadotoxic effects continue to raise concerns and uncertainties. This study proposes to examine these effects at the molecular level and presents extensive research of the steroidogenic and apoptotic effects of PARPi on human ovarian and testicular tissues. This study examines those effects at the molecular and cellular level in an in vitro setting using human testicular and ovarian cells through the use of various techniques. Moreover, the results of this translational research are significant not just at the molecular and cellular levels but also possess critical clinical implications. It is intended to direct future reproductive concerns for patients who may not have had the opportunity to preserve oocytes or sperms before commencing PARPi treatment.

CHAPTER 2
MATERIALS & METHODS

2.*1 Study Plan, Sample Size, and Timeline*

This in vitro translational research study was conducted on mitotic granulosa cell lines, human luteinized granulosa cells (HLGCs), ovarian and testicular tissues. HLGCs, ovarian and testicular tissues were collected at Koç University Hospital and American Hospital between 2024 and 2025.

2.2 *Patients*

HLGCs of this study were derived from follicular aspirates of 43 IVF patients with a recombinant FSH and GnRH antagonist protocol. Recombinant hCG was administered for ovulation induction when the ovaries had a normal response to gonadotropin, or GnRH analogues were used in cycles with high response ovarian stimulation. The retrieval of the oocyte was performed 36 hours post-ovulation trigger. Ovarian cortex specimens were collected from 6 patients undergoing laparoscopic excision of cysts during the early follicular phase of their menstrual cycle. Testicular tissues have been obtained from three individuals who had orchiectomy procedures. All participants provided informed permission, and this research obtained approval from the institutional review board of Koç University. (2024.243.IRB2.108).

2.3 Chemicals and Reagents

The reagents and chemicals utilized in current research were of analytical quality and were from commercial companies. Detailed information regarding each reagent, including supplier and catalog or lot numbers, is provided below. All products were handled and stored according to manufacturers' instructions unless otherwise specified.

General Laboratory Plastics and Consumables: Cell culture plastics such as flasks, 6-, 12-, and 24-well plates, filter tips, and Falcon tubes were obtained from Sarstedt.

Cell Culture Media and Additives:

- **Dulbecco's Modified Eagle Medium/F12 (DMEM/F12),** Multicell, Cat. No: 319-085-CL
- **Fetal Bovine Serum, Heat-Inactivated (FBS),** Biowest, ID Number: S00PB20301
- **Penicillin-Streptomycin Solution (100X),** Biowest, ID Number: MS0216200O
- **Dulbecco's Phosphate Buffered Saline (DPBS),** Biowest, ID Number: MS02DK1007
- **DPBS 10X,** Biowest, ID Number: MS0114Z100F
- **Amphotericin B (Streptomyces sp., CAS 1397-89-3),** Calbiochem, Merck; used as an antifungal agent in cell culture media.
- **Trypsin/EDTA (0.25%),** Multicell, Cat. No: 325-043-EL
- **Trypan Blue 0.4% Solution,** EcoTech Biotechnology, Cat. No: TRY-B100; utilized for cell counting.

DNA, and RNA Work:

- **Quick-RNA™ Microprep Kit,** Zymo Research, Cat. No: R1050 Quick-RNA™
- **RNaseZap,** Invitrogen by Thermo Fisher Scientific, Lot: 01274866; used to remove RNase contamination before RNA isolation.
- **PCR Primers,** synthesized by Sentromer DNA Teknolojileri or Oligomer.
- **iScript cDNA Synthesis Kit,** Bio-Rad, Cat. No: 1708891; used for cDNA synthesis prior to real-time PCR.
- **2X QuantiNova SYBR Green PCR Master Mix,** Lot: 175031764

Protein Quantification and Western Blot:

- **Pierce BCA Protein Assay Kit,** Thermo Scientific, Lot: XJ357486
- **RIPA Lysis Buffer,** EcoTech, Cat. No: RIPA-100
- **2-Mercaptoethanol,** Bio-Rad, Cat. No: 1610710; used as a reducing agent for Western blot sample preparation
- **Thermo Scientific Pierce ECL,** Lot: ZF388339; used as chemiluminescent substrate for Western blot visualization.
- **Ponceau S Staining Solution,** Thermo Scientific, Lot: XC3514601
- **Pierce Phosphatase Inhibitor,** Thermo Scientific, Lot: AC4565331

- **cOmplete™ Mini EDTA-free Protease Inhibitor Cocktail,** Roche, Cat. No: 11836170001
- **10X Tris/Glycine/SDS Buffer,** Bio-Rad, Cat. No: 1610772
- **4X Laemmli Sample Buffer,** Bio-Rad, Cat. No: 1610747
- **Precision Plus Protein Dual Color Standards,** Bio-Rad, Cat. No: 1610374
- **Mini-PROTEAN TGX Gels,** Bio-Rad, Cat. No: 4561084
- **Trans-Blot Turbo Transfer Pack,** Bio-Rad, Cat. No: 1704156
- **Extra Thick Blot Paper,** Bio-Rad, Cat. No: 1703966

Cell Proliferation and Viability Assays:

- **MTT,** Thermo Fisher Scientific, Lot: 2489061
- **Calcein AM,** Invitrogen, Lot: 2286887
- **Propidium iodide,** P4170
- **Sulforhodamine B Sodium Salt,** Sigma-Aldrich, Lot: SHBL9542

Histology and Immunofluorescence:

- **Mounting Medium with DAPI,** Abcam, Lot: GR3299210-7
- **OCT Compound,** DKItalia, Lot: I022I024B
- **Sakura Tissue-Tek Cryomold Standard,** Lot: 20240731
- **Paraformaldehyde 16%,** Electron Microscopy Sciences, Cat. No: 15710-S
- **Epredia Superfrost Plus Adhesion Microscope Slides,** Ref: J1800AMNZ
- **SuperBlock Blocking Buffer,** ScyTek Laboratories, Lot: 69144
- **Goat anti-Mouse Alexa Fluor 594,** Thermo Fisher, Cat. No: A11005
- **Goat anti-Rabbit Alexa Fluor 594,** Thermo Fisher, Cat. No: A11012
- **Goat anti-Mouse Alexa Fluor 488,** Thermo Fisher, Cat. No: A11001
- **Goat anti-Rabbit Alexa Fluor 488,** Thermo Fisher, Cat. No: A11008

Antibodies for Western Blot and Immunofluorescence:

- **PARP Rabbit Antibody,** Cell Signaling Technology, Cat. No #9542S
- **CYP11A1 (D8F4F) Rabbit Antibody,** Cell Signaling Technology, Cat. No #14217S
- **Cleaved PARP (Asp214) (D64E10) XP® Rabbit mAb,** Cell Signaling Technology, Cat. No #5625S
- **StAR (D10H12) XP® Rabbit mAb,** Cell Signaling Technology, Cat. No #8449S

- **3β-HSD Mouse Monoclonal IgG,** Santa Cruz, Cat. No: sc-100466
- **Vinculin Mouse Monoclonal IgG,** Santa Cruz, Cat. No: sc-25336
- **CYP17A1 Mouse Monoclonal IgG,** Santa Cruz, Cat. No: sc-376711
- **17β-HSD Mouse Monoclonal IgG,** Santa Cruz, Cat. No: sc-376719
- **CYP19 Mouse Monoclonal IgG,** Santa Cruz, Cat. No: sc-374176
- **Anti-Mouse IgG HRP-linked Antibody,** Cell Signaling Technology, Cat. No #7076S
- **Anti-Rabbit IgG HRP-linked Antibody,** Cell Signaling Technology, Cat. No #7074S
- **Anti-Bcl-2 Antibody,** St John's Laboratory, Cat. No: STJ27524
- **Anti-BAX Antibody,** Abcam, Cat. No: ab182734
- **Anti-Laminin Rabbit Polyclonal Antibody**, Abcam, Cat. No: ab11575

Flow Cytometry:

- **FXCycle PI/RNase Staining Solution,** Invitrogen by Thermo Fisher Scientific, Lot: 1951431
- **Zombie NIR™ Fixable Viability Kit,** BioLegend, Cat. No #423106

Other Reagents:

- **DMSO (Dimethyl sulfoxide),** Sigma-Aldrich, Cat. No: D2650
- **Niraparib,** Selleckchem.com, Cat. No: S7625
- **Olaparib,** Selleckchem.com, Cat. No: S1060
- **Methanol,** Isolab Chemicals, Lot: LR0903306ANQ
- **Ethanol Absolute,** Isolab Chemicals, Lot: LR0090608ARQ
- **Acetic Acid,** IsoLab Chemicals, Lot: LR0124907AKW
- **Triton X-100,** Sigma, Lot: MKBD8495V
- **Tween-20 Detergent,** Merck, Lot: 3088374
- **Nuclease-free Water,** EcoTech, Cat. No: DW003L
- **TBST Buffer 10X,** Elabscience, Cat. No: E-BC-R335
- **Trichloroacetic Acid,** IsoLab Chemicals, Lot: LR1722104ANW
- **Tris Base Buffer, powder,** Multicell Cat No: 600-127-CG
- **Hank's Balanced Salts Solution 10X,** Biowest, ID Number : MS008H100C

2.4 Cell Culture Medium Formulation

HGrC1 and COV434 granulosa cell lines, together with HLGCs, were maintained at 37 °C in a humidified atmosphere containing 5% CO_2. The cultures were grown in DMEM/F12 medium supplemented with 10% fetal bovine serum (FBS) and 1% Penicillin–Streptomycin–Amphotericin B. Human ovarian cortical tissue and testicular tissue samples were also cultured under the same conditions, with the medium modified to include 20% FBS along with 1% Penicillin–Streptomycin–Amphotericin B.

2.5 Experiments on Human Granulosa Cells

Non-Mitotic Luteinized Granulosa Cells

Isolation and Culture of HLGCs

Follicular fluid samples were obtained during oocyte retrieval procedures from patients undergoing assisted reproductive treatments. Granulosa cells were then isolated following the method reported by (Bildik et al., 2020). Luteinized granulosa cells were pooled when patients shared comparable clinical characteristics, including age, infertility etiology, and stimulation protocol. In cases where these parameters differed, the cells were kept separate unless a sufficient number was available for experimentation. Pooling ensured both adequate cell numbers for downstream assays and a more uniform distribution across experiments. Whenever possible, experiments were also repeated with cells isolated from a single patient to confirm reproducibility. In standard IVF practice, mature follicles are aspirated under transvaginal ultrasonography guidance. As follicular puncture can cause localized bleeding, later aspirates frequently contain blood, leading to a predominance of erythrocytes among the recovered cells. Because erythrocytes sediment more rapidly than granulosa-luteal cells, they can form a dense layer on the culture surface, hindering granulosa-luteal cell attachment. Therefore, removal of these contaminating red blood cells is critical to improve plating efficiency and obtain enriched cultures. Following oocyte retrieval, cumulus–oocyte complexes were visually identified and manually separated from the follicular fluid. The oocytes were then freed from surrounding cumulus cells using either enzymatic digestion or mechanical methods (ELCİK, 2019).
The follicular fluids containing luteal granulosa cells were collected in 50 ml centrifuge tubes, and erythrocytes were removed using the hypo-osmotic lysis method previously described by

(Lobb & Younglai, 2006). Briefly, the samples were centrifuged at 500 × g for 5 minutes, and the supernatants were discarded under sterile conditions using a glass Pasteur pipette connected to a vacuum line in a class II biosafety cabinet. The pellets were resuspended in 27 ml of filtered double-distilled water, and after 20–30 seconds, 3 ml of 10× phosphate-buffered saline (PBS) was added and mixed thoroughly. A second centrifugation at 500 × g for 5 minutes at room temperature (RT) was performed, and the supernatant was again removed. If residual erythrocytes were still visible, the washing step was repeated. Afterward, the final pellet was resuspended in 1 ml of culture medium. Small tissue fragments were eliminated, and the suspension was homogenized by gentle pipetting. Cell viability and concentration were assessed using a hemocytometer with 0.2% trypan blue, which selectively stains non-viable cells due to loss of plasma membrane integrity. The recovered cells were then seeded for subsequent experiments. For Western blotting, cells were plated in six-well plates at a density of 5×10^5 cells per well. For flow cytometry and qRT-PCR, cells were seeded in 12-well plates at 3×10^5 cells per well. Immunofluorescence experiments were performed on cells grown on 12 mm coverslips in 24-well plates at a density of 1×10^5 cells per well. All cultures were maintained at 37 °C with 5% CO_2 for at least 24 hours to allow proper cell adhesion. The following day, confluency, viability, and adherence were examined microscopically. Cultures were considered suitable for treatment when ≥80% of the cells had adhered in clusters without signs of contamination.

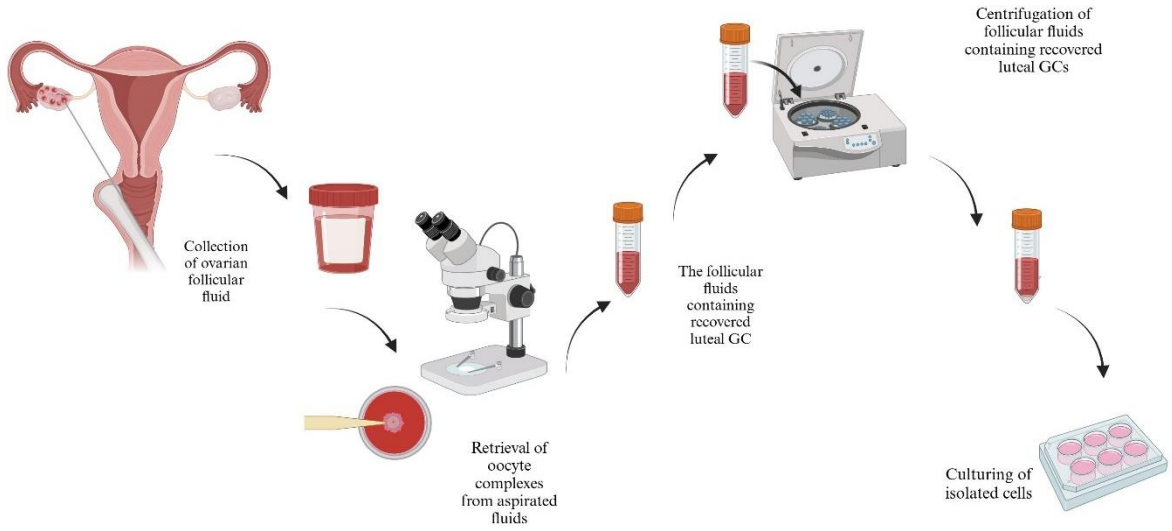

Created with BioRender.com

Figure 16. A diagram illustrating the process of isolating human granulosa cells.

Characterization of HLGCs

HLGCs exhibit a high degree of specialization that do not proliferate spontaneously or in response to mitogenic agents. In vitro, they produce significant amounts of progesterone and estradiol. (ELCİK, 2019).

2.5.1 Mitotic Granulosa Cell Lines

COV434

Immortalized granulosa cell line (COV434) obtained from a 27-year-old female with metastatic granulosa cell carcinoma was established in 1984 (van den Berg-Bakker et al., 1993). This cell line possess the capability to synthesize 17 beta-estradiol when stimulated by FSH, does not have LH receptors and therefore cannot be luteinized, contains molecular markers specific for the apoptotic process that initiates follicular atresia and can form gap junction with surrounding cells around an oocyte (H. Zhang et al., 2000).

HGrC1

Bayasula, et al. isolated granulosa cells from a 35-year-old female and made them immortal by introducing many genes via lentivirus-mediated transfer. This process resulted in the creation of a human nonluteinized granulosa cell line called HGrC1. Those cells express enzymes involved in the production of sex hormones, including steroidogenic acute regulatory protein, aromatase, CYP11A, and gonadotropin receptor but cannot undergo luteinization, exhibiting similar properties to granulosa cells seen in early-stage follicles (Bayasula et al., 2012).

2.6 In Vitro Culture of Human Ovarian Tissue

The ovarian cortical tissue fragments were obtained laparoscopically from non-malignant cyst resections. After washing with PBS, cortical tissue was dissected into 0.5 × 0.5 cm pieces and cultured in 100-mm petri dishes with 15 mL DMEM/F12 medium containing 20% FBS. Equal numbers of fragments were placed in each dish to maintain consistency across treatments. PARP inhibitors were applied at concentrations of 2.5–40 μM, and cultures were maintained for up to 96 h under standard conditions. After incubation, medium was collected for measurement of anti-Müllerian hormone (AMH), estradiol, and progesterone. Tissues were processed for either Western blotting or immunofluorescence.

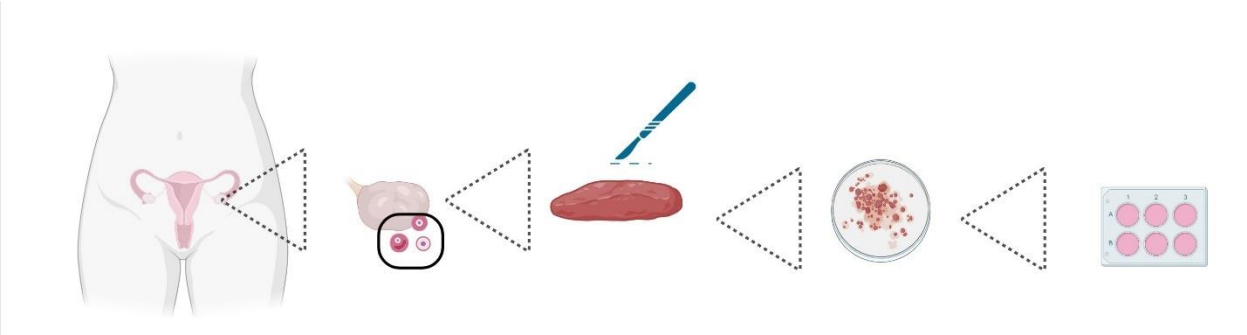

Created with BioRender.com

Figure 17. Schematic representation of the obtaining, processing, and culturing of human ovarian cortical tissues.

2.7 Preparation and Culture of Human Testicular Tissue

Testicular tissues were obtained under sterile conditions and dissected into ~0.5 × 0.5 cm fragments. Tissue samples were maintained in 100-mm Petri dishes with 15 mL of DMEM/F12 medium enriched with 20% FBS.

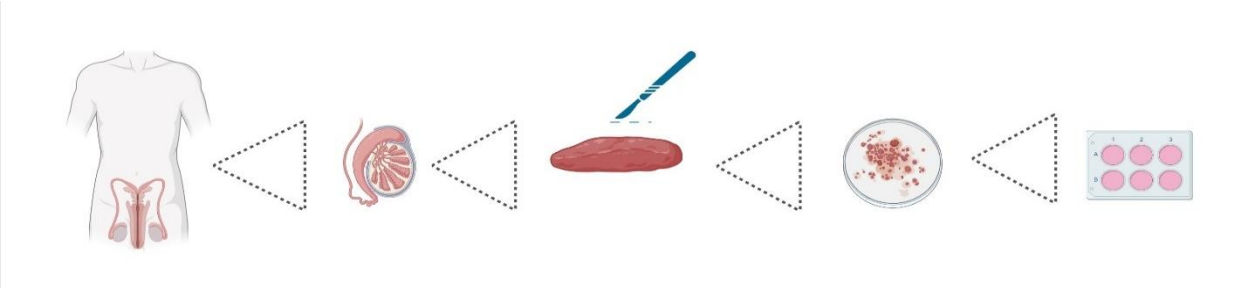

Created with BioRender.com

Figure 18. Schematic representation of the obtaining, processing, and culturing of human testicular tissues.

2.8 Treatments for cell and tissue culture

For PARP inhibition, Olaparib and Niraparib were used. Niraparib arrived in lyophilized form as 5 mg. A stock solution was prepared according to the datasheet instructions with 5 mg Niraparib dissolved in 3.1212 mL DMSO, yielding a concentration of 5 mM. The solution was further used at final concentrations of 2.5 µM, 5 µM, 10 µM, 20 µM, and 40 µM. Treatments were conducted for periods ranging from 24 to 96 hours at 37 °C under 5% CO_2. After treatment, 1 mL of conditioned culture medium was collected and stored at −20 °C for subsequent hormone assays.

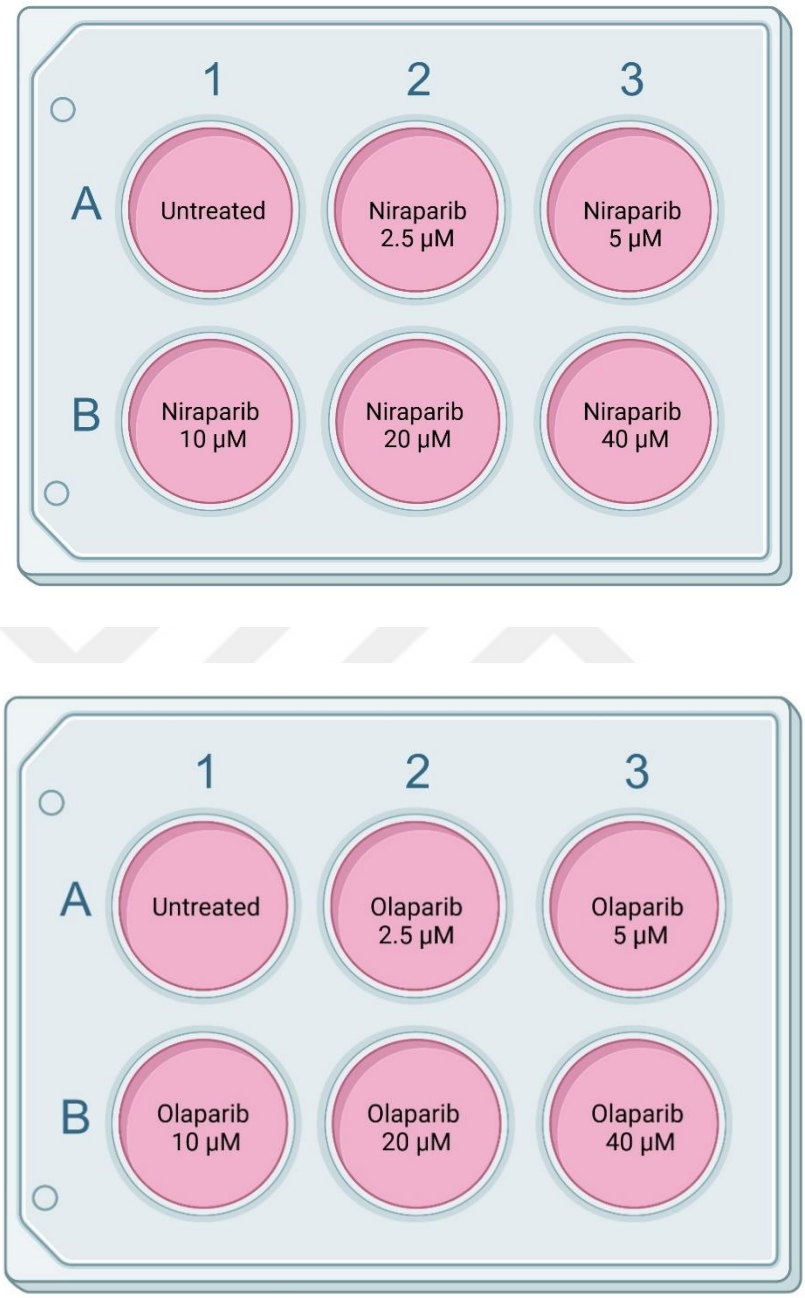

Created with BioRender.com

Figure 19. Treatment setup: Niraparib and Olaparib applied at varying concentrations.

2.9 Flow Cytometry

HLGCs were seeded into six-well plates at a density of 3×10^5 cells per well and exposed to Olaparib in a dose-dependent manner for 96 hours. After treatment, samples intended for hormone analyses were stored, and the culture supernatants were collected in pre-labeled 15 ml Falcon tubes to include any detached or apoptotic cells. Remaining adherent cells were detached with 0.05% Trypsin-EDTA, incubated at 37 °C for 5 minutes, and neutralized by adding fresh culture medium. The resulting cell suspensions were transferred to correspondingly labeled Falcon tubes and centrifuged at 500 × g for 5 minutes. Supernatants were discarded, and the pellets were washed once with 1× DPBS followed by another centrifugation under the same conditions. For cleaved PARP detection, the immunostaining procedure was carried out according to the antibody manufacturer's recommendations with minor modifications. After the final centrifugation, each pellet was incubated with 1 µl Zombie NIR viability dye in 100 µl 1× DPBS for 10 minutes at RT. Samples were then washed with 2 ml FACS buffer and centrifuged at 500 × g for 5 minutes. Cells were fixed in 500 µl of 4% formaldehyde for 20 minutes at RT, washed with DPBS by centrifugation, and resuspended in 1 ml 1× DPBS. Permeabilization was achieved by slowly adding 9 ml of ice-cold absolute methanol to the chilled cells, reaching a final concentration of 90%. Cells were incubated on ice for at least 10 minutes and then washed in 1× DPBS to remove methanol. For primary antibody staining, the cells were resuspended in 100 µl of anti-cleaved PARP antibody diluted 1:400 in antibody dilution buffer and incubated overnight at 4 °C. The following day, samples were washed twice with 1× DPBS and resuspended in 100 µl of fluorochrome-conjugated secondary antibody diluted 1:400 in antibody dilution buffer, followed by overnight incubation at 4 °C. After washing to remove unbound antibody, the final cell suspensions were resuspended in 1× DPBS and analyzed using an Attune NxT Flow Cytometer (Thermo Fisher Scientific, USA). Data were processed with FlowJo software (v10.10.0, BD Biosciences, USA), and the proportion of HLGCs expressing cleaved PARP following Olaparib treatment was quantified by gating on Zombie NIR^- / cleaved $PARP^+$ populations.

2.10 Cell Cycle Analysis

HGrC1 and COV434 cells were seeded into 6-well plates at a density of 1×10^5 cells per well. Subsequent to seeding, cells were cultivated in complete medium for 6 hours to enable optimum

adhesion. After confirming cell adhesion by microscopy, the culture media was replaced with serum-free medium, and the cells were incubated for 18 hours to synchronize their cell cycles before treatment (M. Chen et al., 2012). They were then treated with PARP inhibitors at 2.5–40 μM for 24–96 h. At each timepoint, media were collected, and cells were detached with trypsin-EDTA, pooled with corresponding media, and centrifuged. After PBS washes, pellets were resuspended in FxCycle™ PI/RNase Staining Solution and incubated for 20 minutes (min) in the dark. Cell cycle distribution (G0/G1, S, G2/M, Sub-G0) was analyzed by flow cytometry (Attune NxT) using the PE channel (585 nm).

2.11 Cell Viability Assays

2.11.1 MTT

HLGCs were seeded into 96-well plates, and treatments with PARP inhibitors at concentrations of 2.5, 5, 10, 20, and 40 μM were initiated the following day. MTT stock solution was prepared by dissolving 5 mg/ml of MTT in 1× DPBS to generate a 10× stock, which was subsequently diluted with culture medium to obtain a 1× working concentration. After 72 and 96 hours of drug exposure, the culture medium was replaced with 100 μl of 1× MTT reagent per well. The plates were incubated for 2 hours at 37 °C in a 5% CO_2 atmosphere. After incubation, 75 μl of the supernatant was removed from each well and replaced with 100 μl of DMSO. The plates were then incubated for an additional 10 minutes at 37 °C under 5% CO_2, followed by gentle shaking for 5 minutes to ensure complete solubilization of formazan crystals. Absorbance was subsequently measured at 570 nm using a microplate reader.

2.11.2 Calcein/PI Assay

To assess the viability of luteal granulosa cells following Olaparib exposure, dual staining with Calcein AM and Propidium Iodide (PI) was employed. Calcein AM is a cell-permeable, non-toxic dye that becomes fluorescent once hydrolyzed by intracellular esterases. The enzymatic cleavage of its acetoxymethyl ester group generates Calcein, which produces a bright and uniform green signal distributed throughout the cytoplasm and nucleus of viable cells. Since it does not interfere with cellular metabolism or activity, Calcein AM is well-suited for live-cell

imaging applications. For preparation of the working solution, 50 µg of Calcein AM was equilibrated to RT and dissolved in 50 µl of DMSO to yield a 1 mM stock solution. A 20 µl aliquot of this stock was then diluted with 10 ml of serum-free Hank's Balanced Salt Solution (HBSS), resulting in a ~2 µM working solution with a final DMSO concentration ≤0.1%, a level considered non-toxic for most cell types. This solution was freshly prepared and used within 24 hours to prevent hydrolysis. To discriminate viable from non-viable cells, Calcein AM staining was combined with PI. Propidium Iodide is a nucleic acid-binding dye that penetrates only cells with compromised plasma membranes, thus labeling late-apoptotic or necrotic cells. Consequently, live cells were identified as Calcein-positive, whereas dead or membrane-compromised cells were detected as PI-positive, allowing clear distinction between cell populations. For staining, HLGCs grown on coverslips were rinsed once with HBSS to remove residual serum and incubated with 2 ml of the Calcein AM/PI working solution for 30 minutes at 37 °C. Following incubation, cells were immediately visualized under a fluorescence microscope for assessment of viability.

2.11.3 Sulforhodamine B (SRB) Assay

The SRB assay, developed in 1990 by Skehan et al., has been widely used to produce cost-effective screening assays for investigating cytotoxicity in cell-based investigations. This technique is based on the characteristic of SRB, which forms a stoichiometric bond with proteins under slightly acidic settings and can be removed using basic conditions. Therefore, the quantity of dye attached to the proteins may be utilized as an indicator of cell mass, which can then be extrapolated to determine cell proliferation (Orellana & Kasinski, 2016; Vichai & Kirtikara, 2006). HGrC1 cells were seeded in 96-well plates at a density of 1×10^4 cells per well in 100 µl of culture medium. After 24 hours of incubation, the medium was aspirated and replaced with 150 µl of Niraparib-containing medium. At the end of the designated treatment period, 37.5 µl of 50% trichloroacetic acid (TCA) was directly added to each well, yielding a final concentration of 10% TCA for fixation. The plates were then wrapped in aluminum foil and incubated at 4 °C for one hour. Following fixation, the wells were emptied and rinsed four times with distilled water before being left to air-dry overnight. On the following day, 50 µl of sulforhodamine B (SRB) solution was added to each well and incubated at RT for 30 minutes. Excess dye was

subsequently removed, and the wells were washed five times with 1% acetic acid. The plates were again left to dry overnight. To solubilize the bound dye, 150 µl of 10 mM Tris base was added to each well the next day, and absorbance was measured at 564 nm using a microplate reader.

2.12 xCELLigence System

A cell culture device called xCELLigence enables the continuous and precise measurement of cell growth, survival, toxicity, and many cellular activities such as adhesion, invasion, and receptor function. Importantly, it achieves these measurements without the need for any chemical compounds or labeling agents (Bird & Kirstein, 2009). The impedance-based RTCA system (consisting of an impedance analyzer, RTCA station, computer with RTCA software, and a 96-well electronic E-Plate containing interdigitated gold microelectrodes) was employed to monitor cell viability and proliferation in real time. The instrument detects changes in electrical impedance, which is influenced by cell attachment, spreading, and proliferation, and reports these changes as the cell index (CI) (Martinez-Serra et al., 2014). Before cell seeding, each well of the E-Plate was preloaded with 100 µl of complete culture medium, incubated for 15 minutes at RT, and background impedance was measured. Cells were then added at a density of 1×10^4 per well in a final volume of 200 µl. Plates were maintained at 37 °C in a humidified incubator with 5% CO_2, and impedance was automatically monitored at 30-minute intervals. Once the cultures reached the logarithmic growth phase (approximately 18–20 hours after plating), treatments with Olaparib or Niraparib were applied at the indicated concentrations. Cell proliferation and viability were subsequently tracked in real time for up to 96 hours, with impedance measurements recorded every 30 minutes. Data acquisition and analysis were carried out using the xCELLigence RTCA software (version 1.2) (ELCİK, 2019).

2.13 Western Blot Analysis

2.13.1 Protein Isolation

Protein Isolation From Cell Culture

HLGCs, HGrC1, and COV434 cells were seeded in six-well plates, with densities of 5×10^5 cells per well for HLGCs and 3×10^5 cells per well for HGrC1 and COV434. The difference in seeding numbers reflected the higher proliferative capacity of the HGrC1 and COV434 cell lines compared to the non-proliferative nature of HLGCs. Protein extraction was carried out according to the duration of the designated treatments. Following treatment, conditioned media were collected in pre-labeled 15 ml Falcon tubes to ensure the inclusion of any detached cells. Adherent cells were detached using 0.05% trypsin–EDTA, and the enzymatic reaction was neutralized by the addition of fresh medium. The resulting suspensions were transferred into the same Falcon tubes containing the corresponding spent media and centrifuged at 500 × g for 5 minutes. Supernatants were discarded, and pellets were washed once with 1× DPBS, followed by another centrifugation step under the same conditions. Cell pellets were then resuspended in 100 µl of ice- cold Radioimmunoprecipitation Assay (RIPA) buffer supplemented with 1× phosphatase inhibitor cocktail and 1× protease inhibitor cocktail, and transferred into labeled 1.5 ml Eppendorf tubes kept on ice. To enhance cell lysis, the suspensions were vortexed four times at 5-minute intervals. Lysates were subsequently centrifuged at 16,000 × g for 20 minutes at 4 °C. After centrifugation, the clarified supernatants containing soluble proteins were transferred into new, labeled tubes and kept on ice. A BCA protein assay kit was used to assess protein concentrations in accordance with the manufacturer's procedure.

Protein Isolation From Ovarian and Testis tissues

After ovarian and testicular tissue fragments had been cultured in six-well plates and exposed to PARPi (Olaparib or Niraparib) for 96 hours, they were transferred into two ml Eppendorf tubes for protein isolation. Tissues were initially rinsed with 1× DPBS, after which 300 µl of ice-cold RIPA buffer mixture was added. Samples were kept on ice during the entire procedure. The tissue pieces were further dissected into smaller fragments with sterile scissors and homogenized using a tissue homogenizer. The homogenization was performed in two cycles: 20 seconds of processing, a 30-second pause, and an additional 20 seconds of homogenization. The lysates were then vortexed four times at 5-minute intervals and centrifuged at 16,000 × g for 20 minutes at 4 °C. Following centrifugation, the pellets containing insoluble material were discarded, and the clarified supernatants were transferred to fresh, labeled 1.5 ml Eppendorf tubes. A BCA

protein assay kit was used to assess protein concentrations in accordance with the manufacturer's procedure.

Protein Concentration Measurement by BCA Assay

The quantities of proteins were determined by using the Pierce™ BCA Protein Assay Kit, which quantifies protein content through the detection of cuprous ions formed during the reaction. The kit includes Reagent A, Reagent B, and a Bovine Serum Albumin (BSA) stock solution (2 mg/ml), all stored at RT. To generate the standard curve, protein standards were prepared according to the manufacturer's protocol using BSA as the reference protein. Eight concentrations were used (2000, 1500, 1000, 750, 500, 250, 125, and 25 µg/ml), while nuclease-free water served as the blank control. Sample lysates were diluted 1:10 in ultrapure water prior to loading. Ten microliters of each standard and diluted sample were pipetted in duplicate into a clear, flat-bottomed 96-well plate. The working reagent was prepared freshly by mixing Reagent A and Reagent B at a ratio of 50:1. Two hundred microliters of the reagent were added to each well, and the plate was briefly shaken for 40 seconds, then covered with aluminum foil to protect from light. Incubation was carried out at 37 °C for 30 minutes in a non-sterile incubator. After cooling the plate to RT, absorbance was recorded at 562 nm using a microplate reader. Protein concentrations of the samples were determined based on the standard curve, and 20 µg of protein from each lysate was subsequently loaded onto precast gels for electrophoresis.

2.13.2 Gel Electrophoresis

In order to allow protein running and separation through SDS-PAGE, a mixture of 4x Laemmli buffer and β-mercaptoethanol (10:1) was prepared. This master mix was added to the protein samples at a ratio of 3:1 (protein volume to master mix volume). To denature the proteins, the specimens have been heated at 95°C for 5 min and later positioned on ice. Mini-PROTEAN TGX precast gels (10-well, 50 µl volume per well, 4-15%) were used for gel electrophoresis. 3 µl of Precision Plus Protein Dual Color Standards were loaded into the first well, followed by the prepared samples in the subsequent wells. Electrophoresis was started at 90 V until the proteins passed through the stacking gel; later, the voltage was increased to 110 V to allow the proteins to run through the separating gel.

2.13.3 Semi-dry Transfer

Trans-Blot Turbo Transfer Packs were utilized for semi-dry transfer following the Bio-Rad protocol. The base of the cassette was layered with membrane, and the bottom stack, and a blot roller was used to remove any trapped air bubbles. The gel was immediately positioned on the membrane, and air bubbles were expelled again by using a blot roller. Next, a second wetted transfer stack, functioning as the top ion stack, was then positioned on top of the gel. The resulting sandwich was further rolled to eliminate any remaining air bubbles. After properly closing and locking the cassette lid, it was inserted into the instrument to begin the transfer process. Once the transfer procedure was complete, the efficiency is assessed by treating the membranes with Ponceau S solution for 1 minute on a shaker. This solution selectively attaches to the amino groups that have a positive charge and also forms non-covalently bonds with the non-polar regions of proteins. After confirming that the transfer was effective, the membrane underwent two washes with 1X TBS-T using a shaker.

2.13.4 Blocking

As soon as the membrane had been sufficiently cleansed, it was ready for blocking. A solution containing 5% nonfat dry milk powder was used for the purpose of blocking, and the membranes were subjected to this solution at RT for 1 hour. Following the membranes were thoroughly washed with TBST solution, repeating the process three times, with each rinse lasting for 5 minutes. Next, they were made ready for incubation with the primary antibody.

2.13.5 Primary and Secondary Antibody Incubation

Primary antibodies were diluted as recommended by the manufacturer in a solution containing 0.2% sodium azide (v/v) and 0.3% BSA prepared in 1× TBS-T. The membranes were shaken overnight at 4 °C with the diluted primary antibodies. Following the incubation period, the antibody solutions were saved for future use, and the membranes were gently agitated while being rinsed three times with 1× TBS-T. For secondary detection, HRP-conjugated antibodies were prepared at a 1:1000 dilution in 5% nonfat dry milk. Membranes were then incubated with

the secondary antibody solution for 1 hour at RT on a shaker, followed by three additional washes with 1× TBS-T (5 minutes each).

2.13.6 Detecting

To visualize the interest proteins, the Pierce Enhanced Chemiluminescence (ECL) substrate was used in a 1:1 proportion. The membranes were exposed to sufficient amount of ECL for a duration of 1 minute. Then, chemiluminescence detection was performed using the ChemiDoc XRS+ Imaging System (Bio-Rad). Further applications were conducted using ImageLab software (Bio-Rad, #1708299).

2.14 Immunofluorescent Staining

2.14.1 Immunofluorescent Staining of Cells

Before seeding, sterile 12 mm coverslips were placed into the wells of 24-well culture plates. Cells were then exposed to Olaparib or Niraparib at the specified concentrations and time points to achieve PARP inhibition. At the end of each treatment period, 1 ml of culture medium from each well was collected and stored for subsequent hormone analysis. The remaining medium was discarded, and cells were gently rinsed with 500 µl of 1× DPBS. To minimize detachment during fixation, both 1× DPBS and 4% paraformaldehyde (PFA) solutions were equilibrated to RT prior to use. Cells were fixed with 500 µl of 4% PFA for 20 min at RT, followed by three washes with 500 µl of 1× DPBS. Following fixation, permeabilization was performed by incubating the cells in 500 µl of 0.1% Triton X-100 for 15 min. The solution was then removed, and wells were rinsed once with 500 µl of DPBS-T. To reduce nonspecific antibody binding, 400 µl of SuperBlock solution was added to each well and incubated for 20 minutes. For co-staining assays, multiple primary antibodies labeled with distinct fluorophores were applied simultaneously, enabling visualization of different target proteins within the same sample (Suzuki, Matsuzaki, Hagiwara, Aoki, & Takata, 2007). For double staining, two primary antibodies raised in different host species (mouse, rabbit, or goat) were diluted together in Super Block medium at the concentrations recommended by the manufacturer. Equal volumes of each diluted antibody were combined in a single tube to allow simultaneous application. To prepare for staining, parafilm was layered over a sterile Petri dish, and 20 µL of the antibody mixture

was pipetted onto the parafilm for each coverslip. Coverslips containing cells were carefully removed from culture wells with sterile tweezers and placed cell-side down onto the antibody droplets. The Petri dishes were sealed with parafilm to prevent drying, a moistened tissue was placed inside to maintain humidity, and the dishes were incubated overnight at 4 °C. The following day, coverslips were gently lifted from the antibody droplets using tweezers and washed in a beaker containing 1× DPBS-T. Tween 20 was included in the buffer to reduce surface tension, enhance the removal of unbound antibodies, and minimize background fluorescence. Species-specific secondary antibodies conjugated to distinct fluorophores were diluted 1:100 in 1× DPBS according to the manufacturer's instructions. Coverslips were incubated with the secondary antibody mixture for 60 min at 37 °C in the dark to protect fluorophores from photobleaching. This incubation period was sufficient to promote strong binding between secondary and primary antibodies while avoiding excessive background fluorescence that could result from prolonged exposure (Esmaeilian, Yusufoglu, Iltumur, Bildik, & Oktem, 2024). Following secondary antibody incubation, coverslips were washed again by immersing them in 1× DPBS-T to remove residual antibodies. For mounting, 5–10 µL of Fluoroshield mounting medium containing DAPI was placed onto pre-labeled glass microscope slides. Coverslips were carefully lifted from the Petri dish with sterile tweezers and positioned cell-side down onto the droplet of mounting medium. To secure the coverslips, four small drops of nail polish were applied around the edges; once partially dried, additional nail polish was applied along the margins to seal the preparation. Slides were stored at 4 °C until imaging. Immunofluorescent images were acquired using a Leica DMI8 confocal microscope with appropriate excitation and emission channels for the selected fluorophores. Prior to imaging, a drop of immersion oil was placed on the slide, and coverslips were examined using a 63× objective. Imaging conditions were optimized to ensure visibility while keeping laser intensity at the lowest possible level to minimize photobleaching during spot identification and focusing. Parameters including image resolution, scan speed, and laser power were standardized before capturing final images. For quantitative analysis, ImageJ software was employed to evaluate fluorescence intensity of target proteins.

2.14.2 Immunofluorescent Staining of Tissue

Following the culturing of ovarian and testis tissues on 6-well plates, they were exposed to PARPi (Olaparib or Niraparib) at varying concentrations over a period of 96 hours. The tissues were fixed using a 4% paraformaldehyde solution, which is a potent fixative routinely used to stabilize tissue structure and prevent protein cross-linking. The tissues were first washed in 1X DPBS to remove any residual medium. After the washing step, with tweezers, the tissue was gently moved from petri to falcon tubes with minimum disturbance. Each 0.5 × 0.5 cm piece of tissue was fixed in 15 ml Falcon tube with 15 mL of fresh 4% paraformaldehyde solution. Tissue samples were then fixed in paraformaldehyde for at least 24 hrs at 4°C. Tissues were washed in 1x DPBS to remove the remaining fixative and then transferred through a series of increasing sucrose concentrations (10%, 20%, 30%) as cryoprotectants before embedding in OCT compound which is essential to cryoprotecting from ice crystal formation damage during freezing and section. The tissues were maintained in each sucrose solution until they had sank to the bottom of the falcon tube, which indicates that they had been adequately dehydrated.
Upon dehydration of the tissues with sucrose, the tissues were washed with 1X DPBS to remove any excess sucrose. Subsequently, the tissues were moved to cryomolds inside the freezing area of the cryostat. The cryomolds were filled with OCT compound, and the tissues were precisely placed inside the OCT to facilitate the desired sectioning plane. The embedding process guarantees the maintenance of tissue structure and shape upon freezing, which is essential for the accurate analysis of tissue structure, cellular morphology, and specific proteins. The tissues implanted in OCT were promptly cryopreserved and kept as solid blocks at a temperature of -80°C until they were cut into sections. In order to conduct frozen sectioning, tissue samples that had been embedded in OCT were sliced using a cryostat machine, which was adjusted to a temperature ranging from -20°C to -30°C. This temperature range allows for the maintenance of tissue rigidity, which enables the of high-quality sections. The 7 µm thick sections of testicular and ovarian tissues were carefully attached on tissue adhesive slides. After sectioning, slides were air-dried and stored at −20 °C until staining. Frozen sections were first rinsed with 1× DPBS to remove residual OCT compound, and hydrophobic barriers were drawn around the tissue using a PAP-PEN. Each section was incubated at room temperature for 15 minutes after being treated with 300-400 µl of permeabilization buffer. The buffer was then removed, and slides were washed three times with 0.3% DPBS-T (5 minutes each). Blocking was performed with SuperBlock solution for 20 minutes at RT to reduce nonspecific antibody binding. Primary

antibodies were diluted in SuperBlock according to the manufacturer's recommendations, and 20–30 µl of antibody solution was added to each section. Slides were incubated overnight at 4 °C in a humidified chamber. The following day, the antibody solution was removed, and sections were washed three times in DPBS-T (5 minutes each). For detection, fluorophore-conjugated, species-specific secondary antibodies were prepared in 1× DPBS and applied at 20–30 µl per section. For 90 minutes, the slides were left in a dark environment at 37 °C.
After secondary antibody incubation, samples were washed again three times with DPBS-T (5 minutes each). Nuclear counterstaining and mounting were performed by applying 5–10 µl of DAPI-containing mounting medium to the edge of each section, followed by careful placement of coverslips with tweezers to ensure even distribution. Coverslips were sealed with four small drops of nail polish, which were partially dried before completely sealing the edges. Prepared slides were stored at 4 °C until imaging (Esmaeilian et al., 2024). Confocal microscopy was used for visualization, and fluorescence intensity analyses were performed as described for the immunofluorescence staining of cultured cells.

2.15 Gene Expression Analysis

2.15.1 RNA Isolation

HLGCS were extracted and cultured for qRT-PCR experiments. Subsequent to cell adhesion and stability, the cells were exposed to 40 µM Olaparib for a duration of 72 hours. Post-treatment, adherent cells were detached with 0.05% trypsin/EDTA, as described previously for flow cytometry and Western blot assays. Total RNA was isolated using the Quick-RNA™ Microprep Kit in accordance with the manufacturer's guidelines. Use of a NanoDrop spectrophotometer (ND-2000, Thermo Fisher Scientific) allowed for the evaluation of the isolated RNA's concentration and purity. After the RNA samples were quantified, they were kept at -20 °C until they were used in cDNA synthesis.

2.15.2 cDNA Synthesis

Following manufacturer recommendations, cDNA synthesis has been done with iScriptTM cDNA Synthesis Kit. To synthesize 1000 ng of cDNA per reaction, an appropriate amount of

RNA had been added to the reaction mix. Until further use in qRT-PCR tests, synthesised cDNA was kept at +4°C.

2.15.3 qRT-PCR

mRNA expression levels were quantified using the LightCycler® 480 SYBR Green I Master Kit (Roche, Germany). Prior to amplification, all cDNA samples were diluted 1:4 (10 µL cDNA + 30 µL nuclease-free water). Primer working solutions were prepared from 100 µM stocks, diluted to 10 µM by combining 10 µL of forward primer, 10 µL of reverse primer, and 180 µL of nuclease-free water. This approach ensured uniform pipetting and avoided direct handling of concentrated primer stocks. Reactions were carried out in 96-well plates with a final volume of 10 µL per well, containing 3 µL nuclease-free water, 1 µL primer working solution, 5 µL SYBR Green Master Mix, and 1 µL diluted cDNA. A bulk master mix (excluding cDNA) was first prepared and dispensed into wells, followed by the addition of individual cDNA samples. Plates were sealed, centrifuged at 300 × g for 1 min to eliminate bubbles, and then subjected to qRT-PCR. Primer sequences are provided in Table 1. The thermal cycling program was as follows:

Initial denaturation (holding phase): ramp from 25 °C to 95 °C at 2.8 °C/s; hold at 95 °C for 5 min.

Amplification (40 cycles):

95 °C for 10 s (denaturation)

60 °C for 30 s (annealing; ramp rate 2.1 °C/s)

72 °C for 20 s (extension; ramp rate 2.1 °C/s)

Melt curve stage:

90 °C for 5 s (ramp rate 1.6 °C/s)

65 °C for 1 min

gradual increase to 97 °C at 0.05 °C/s, maintained for 15 s

Final cooling: 40 °C for 10 s (ramp rate 2.0 °C/s).

(Yıldız, 2021). All reactions were performed in technical triplicates. The relative gene expression levels were determined using the ΔCt method.

Table 1. List of primers and their corresponding sequences used in qRT-PCR.

F: forward, R: reverse

Gene	5′-Sequence-3′
GAPDH	F: GAAGGTGAAGGTCGGAGTCAA
	R: CTTCCCGTTCTCAGCCATGTA
StAR	F: AAACTTACGTGGCTACTCAGCATC
	R: GACCTGGTTGATGATGCTCTTG
CYP19A1 (Aromatase)	F: GCAAGCTCTCCTCATCAAACCA
	R: GGTCACCACGTTTCTCTGCT
3β-HSD	F: GCCTTCAGACCAGAATTGAGAGA
	R: TCCTTCAAGTACAGTCAGCTTGGT
PROG-R	F: GCCAGCCAGAGCCCACAATA
	R: TGTGCTGCCCTTCCATTGCC
CYP17A1	F: GTTTCAGCCGCACACCAACT
	R: ACTCACCGATGCTGGAGTCA
LH-R	F: TTCAATGGGACGACACTGACTT
	R: TGTGCATCTTCTCCAGATGTACGT
FSH-R	F: TTGAACTGAGGTTTGTCCTCACCA
	R: GGCCTCAGGGTTGATGTAGAGC
ESR1	F: GAGGGCTGCAAGGCCTTCTT
	R: TCCCACCTTTCATCATTCCCAC
ESR2	F: AGGCCATGATCCTGCTCAAT
	R: CCATGCCCTTGTTACTCGCA

2.16 Hormone Assays

2.16.1 AMH

The production of AMH is carried out by the granulosa cells that found in the preantral and small antral follicles. It is therefore associated with the functional ovarian pool, however there is disagreement about its relationship to the overall pool of primordial follicles (Cedars, 2022).

Aiming to evaluate the effect of PARP inhibition on functional ovarian reserve, AMH levels were evaluated from spent culture media of ovarian cortex tissues. 1 ml of the used medium was taken and preserved at -20°C for hormone analysis before tissue specimens were collected for further studies. The levels of AMH were measured using electrochemiluminescence immunoassay (ECLIA). Manufacturer instructions guided the use of an AMH-specific commercial kit (Elecsys® AMH, Roche Diagnostics). The Cobas® 801 analytical unit (Roche) was used for all analyses. Age affects the quantifiable range of AMH values. While for women aged 35–40 years the reference range was 0.1–7.5 ng/mL, those between 30–35 years it was 0.6–8.1 ng/mL. The assessment used just these reference periods because all ovarian tissue samples utilized in this research were from individuals between the ages of 30 and 40.

2.16.2 Estradiol and Progesterone

Human luteal granulosa cells synthesize estrogen, and progesterone, even at their basal activity, as they are steroidogenic cells. To study PARP inhibition impact on steroidogenesis in HLGCs, estrogen and progesterone levels were measured from spent culture medium, as these hormones are secreted into the medium by the cells. After different treatment periods for PARP inhibition were completed, 1 ml of the spent medium from each well was gathered and kept at -20°C for hormone analysis. The amount of estradiol and progesterone within the culture medium were measured using ECLIA. The culture medium was analyzed for progesterone and estradiol hormone levels using ECLIA kits specifically designed for this purpose (Elecsys Progesterone II, Cobas for progesterone and Elecsys Estradiol II, Cobas for estradiol). The measurements were conducted following the directions provided by the manufacturer. All analyses were conducted using the Cobas® 801 analytical instrument. The minimum detection limits were 5.00 pg/ml (18.4 pmol/L) for estradiol and 0.05 ng/ml (0.159 nmol/L) for progesterone.

2.16.3 Testosterone

In order to evaluate the influence of PARP inhibition on testosterone secretion, human testicular tissue samples were utilized. Before the collection and fixation of tissues for other experimental procedures, 1 ml of conditioned medium was retrieved and stored at −20 °C for subsequent hormonal analysis. Testosterone concentrations were measured using ECLIA. Quantification was performed with a testosterone-specific kit (Elecsys Testosterone II, Cobas) following the

manufacturer's protocol, and analyses were carried out on the Cobas® 801 analyzer. The assay sensitivity allowed detection of testosterone levels as low as 0.025 ng/ml (0.087 nmol/L).

2.17 Statistical Analysis

The statistical studies were conducted with Python (version 3.12) and GraphPad Prism (version 10). In Python, the pandas library was utilized for data organization and preprocessing, NumPy for numerical operations, SciPy.stats for hypothesis testing (including t-tests, ANOVA, and non-parametric tests), correlation analysis, and descriptive statistics, and statsmodels for regression analyses and advanced modeling. Data visualization was performed with matplotlib.pyplot and seaborn. GraphPad Prism was additionally used for standard statistical analyses, dose–response curve fitting, and the preparation of publication-ready figures. Significance of model parameters was determined using p-values with a threshold set at $p < 0.05$.

CHAPTER 3
RESULTS

3.1 Effects of PARP Inhibitors on Human Granulosa Cell Lines

3.1.1 Cell Viability and Proliferation

Real-Time Proliferation Analysis in COV434 and HGrC1 Cell Lines

Niraparib and Olaparib were administered to COV434 and HGRC1 cell lines at increasing dosages (0.5, 2.5, 5, 10, 20, and 40 μM) for 96 hours to assess the impact of PARP inhibition on cell proliferation and viability. Then, real-time cellular monitoring was conducted with the xCELLigence system, and the normalized cell index and slope data were evaluated. Normalized Cell Index (CI) values were obtained from real-time cell impedance measurements using the xCELLigence RTCA platform. Each condition (drug dose and timepoint) was assessed across replicates. CI values were aggregated by calculating the mean Cell Index per dose and timepoint. At 96 hours, a noticeable, dose-dependent inhibition of cell proliferation was seen at 10 μM, 20 μM, and 40 μM, with the most substantial decreases occurring at the highest concentrations in Niraparib-treated COV434 cells (Figure 20). Interestingly, cell index and slope values of 0.5 and 2.5 μM remained elevated above control levels after 96 hours, but 5 μM was similar to control.

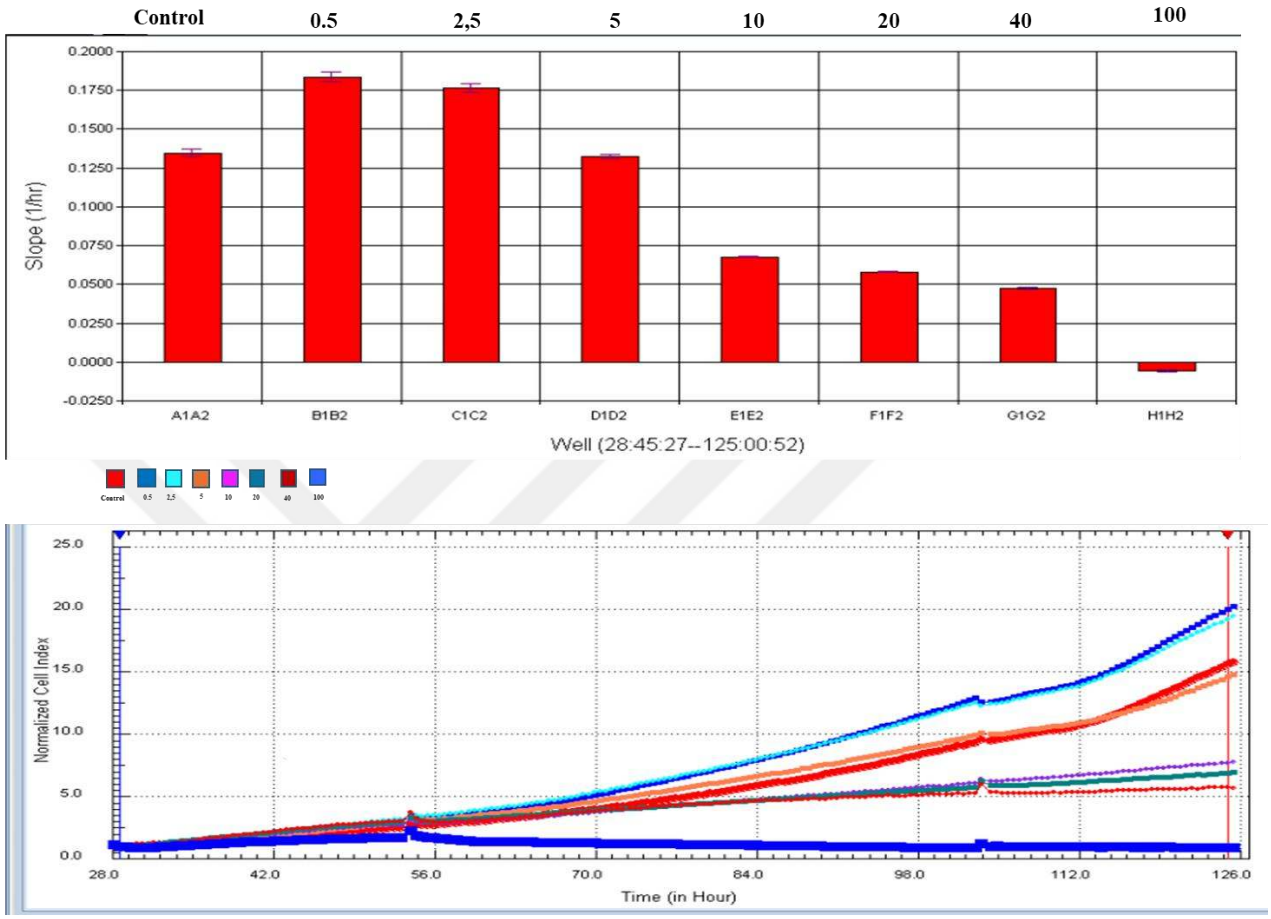

Figure 20. Normalized cell index and slope values for COV434 cells treated with increasing concentrations of Niraparib at 96 hours.

In HGrC1 cells, the cell index of all treatment groups aligned with control values, with the exception of a little decrease seen at 40 µM at 96 hours (Figure 21)**.**

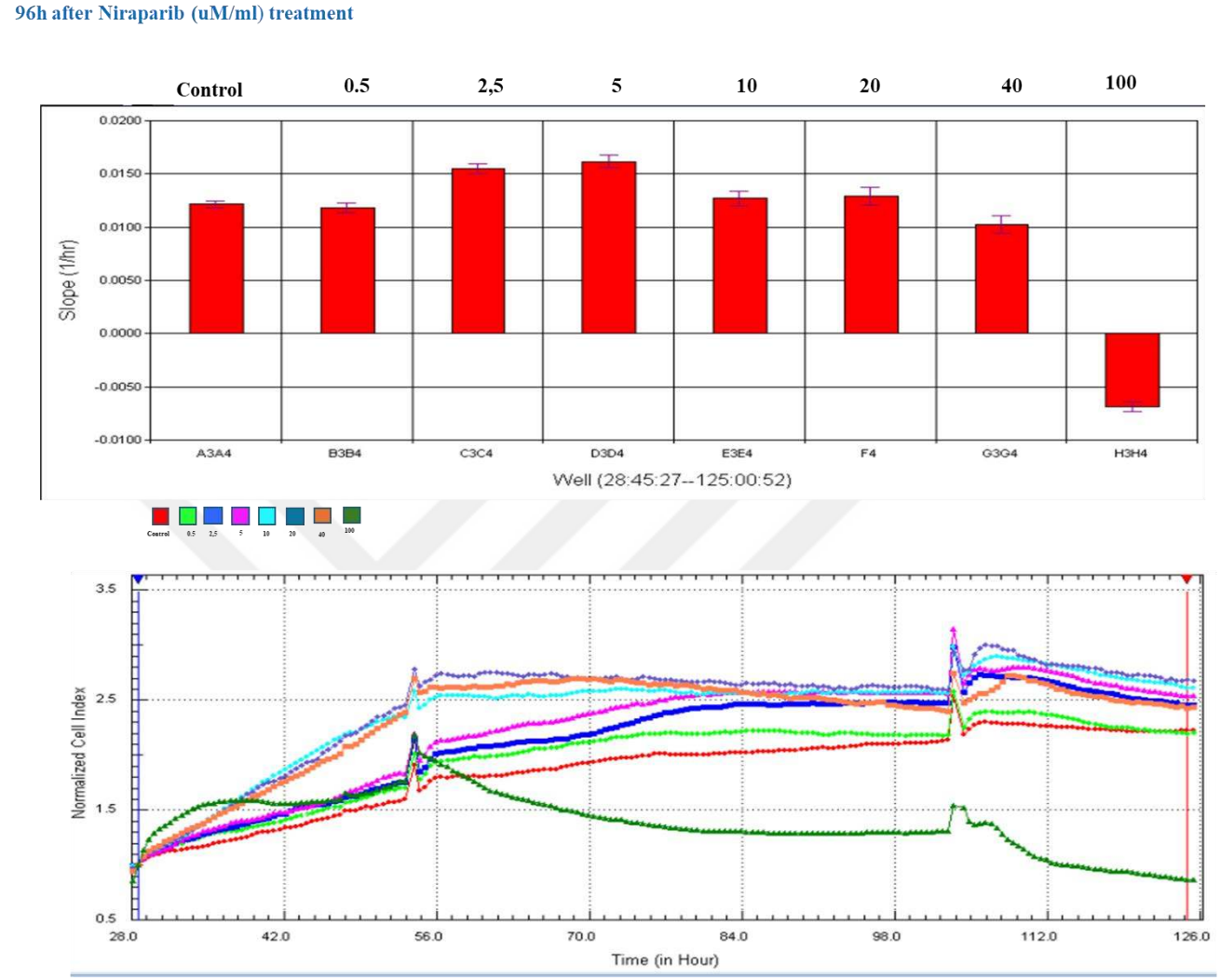

Figure 21. Slope and normalized cell index values for HGrC1 cells treated with increasing concentrations of Niraparib at 96 hours

In COV434 cells, Olaparib administration caused a significant, dose-dependent decrease in normalized cell index and slope. This impact was seen in all treatment groups, with higher dosages leading to a more significant reduction in cell proliferation and viability relative to the control group (Figure 22). The inhibitory impact of Olaparib on cell proliferation intensified with time, highlighting the compound's strong cytostatic and cytotoxic properties in this cell line.

96h after Olaparib (uM/ml) treatment

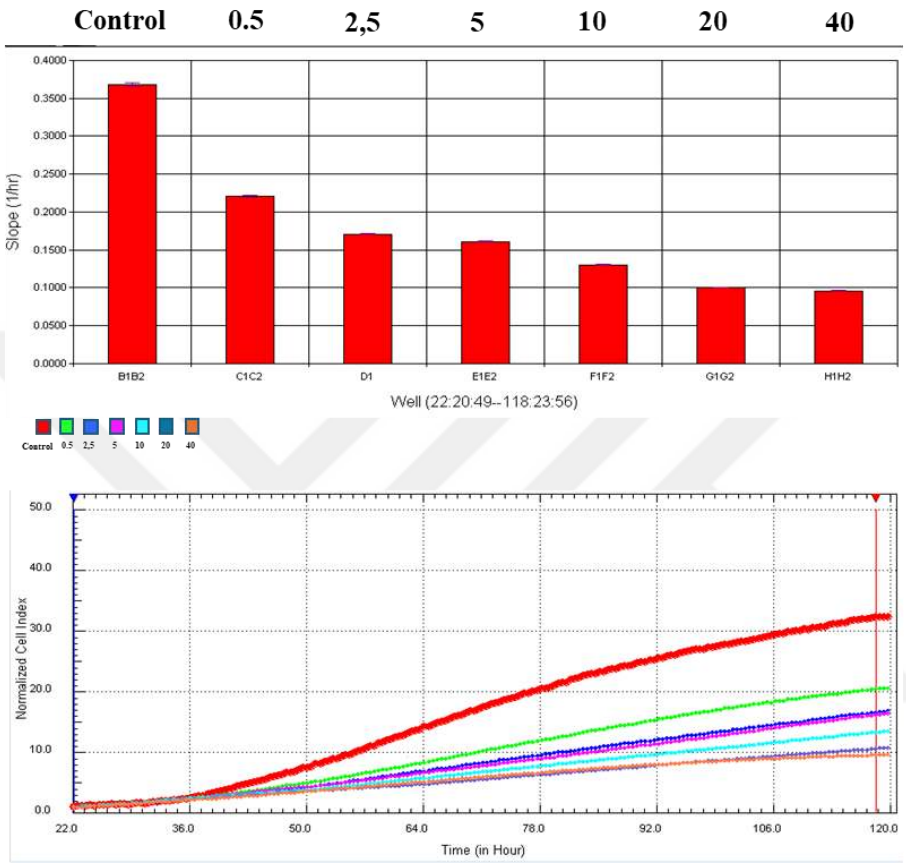

Figure 22. Normalized cell index and slope values for COV434 cells treated with increasing concentrations of Olaparib at 96 hours.

After 96 hours, Olaparib administration led to a drop in the normalized cell index at all dosages in a dose-dependent manner, and the largest decrease was seen at 5 µM, 10 µM, 20 µM, and 40 µM in HGrC1 cells (Figure 23).

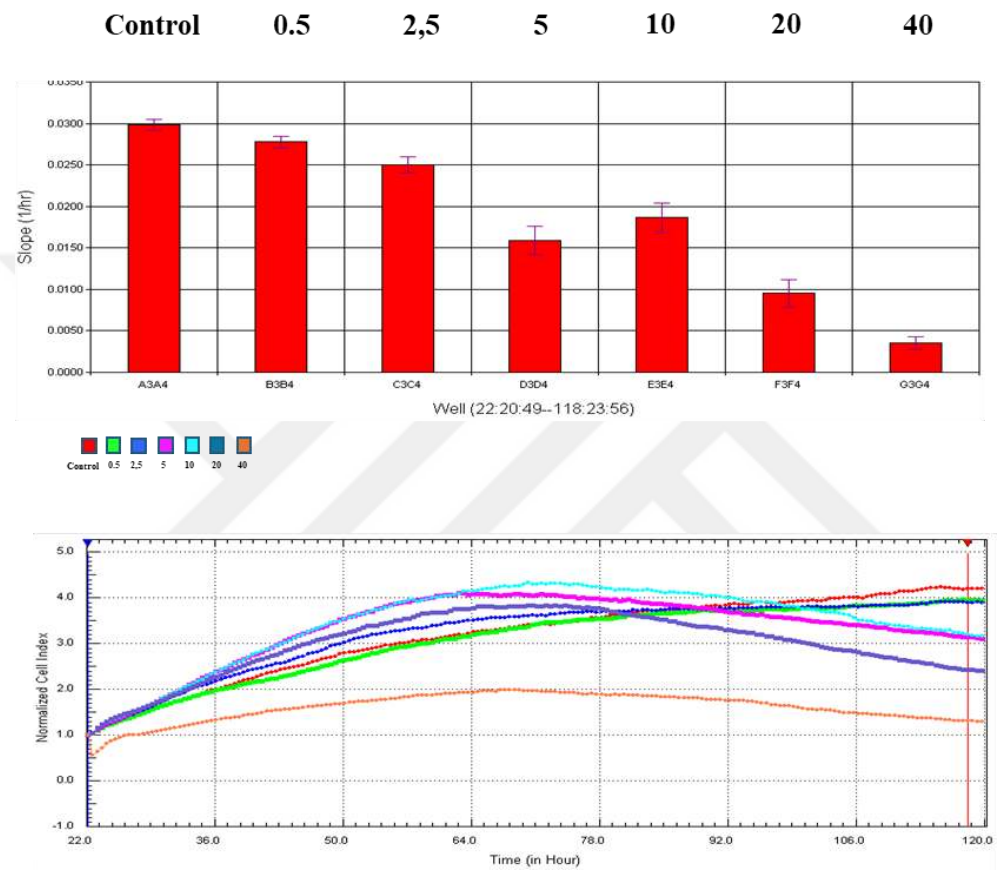

Figure 23. Slope and normalized cell index values for HGrC1 cells treated with increasing concentrations of Olaparib at 96 hours.

Dose and Time-Dependent Effects of Niraparib on HGrC1 Cell Proliferation

SRB assays were performed after treating HGrC1 cells with various doses (2,5–40 µM) of Niraparib for varying durations (24–72 hours) to study the cytotoxic impact of PARPi. Then, SRB assay data were analyzed using Linear Mixed-Effects Models (LMM) to assess normalized cell viability across different dose and time combinations. The model incorporated both main effects and their interaction (Dose × Time) as fixed effects, while biological replicates were

considered as random effects to account for replicate-to-replicate variability. Following the mixed-effects modelling, pairwise comparisons between all dose-time groups were conducted using Tukey's Honest Significant Difference (HSD) post-hoc test to identify specific group differences. Tukey's test results were sorted and clearly summarized based on adjusted p-values. The results were visualized using a heatmap of mean viability differences (Figure 36).

Several conditions showed robust and statistically significant reductions in cell viability compared to baseline. Specifically, treatment with 40 µM for 24 h resulted in a ~34% decrease in viability relative to untreated controls at all timepoints (adjusted $p < 0.001$) (Figure 23). Similar reductions were observed for 40 µM at 72 h (−33.5%) and 20 µM at 24–48 h (−27.2%), all with adjusted p-values below 0.01. These clusters of strong negative differences highlight early and sustained cytotoxicity at higher concentrations. Notably, low-dose exposures (e.g., 2.5 µM and 5 µM) did not show significant reductions compared to untreated conditions, consistent with a threshold-like viability loss at ≥10 µM.

The heatmap revealed a symmetrical pattern, with the largest viability reductions concentrated in the comparisons involving high-dose, early-exposure groups (particularly 40 µM at 24 h). These findings indicate a sharp dose-dependent effect that manifests early and remains consistent over time, supporting the presence of a strong cytostatic response at specific concentrations.

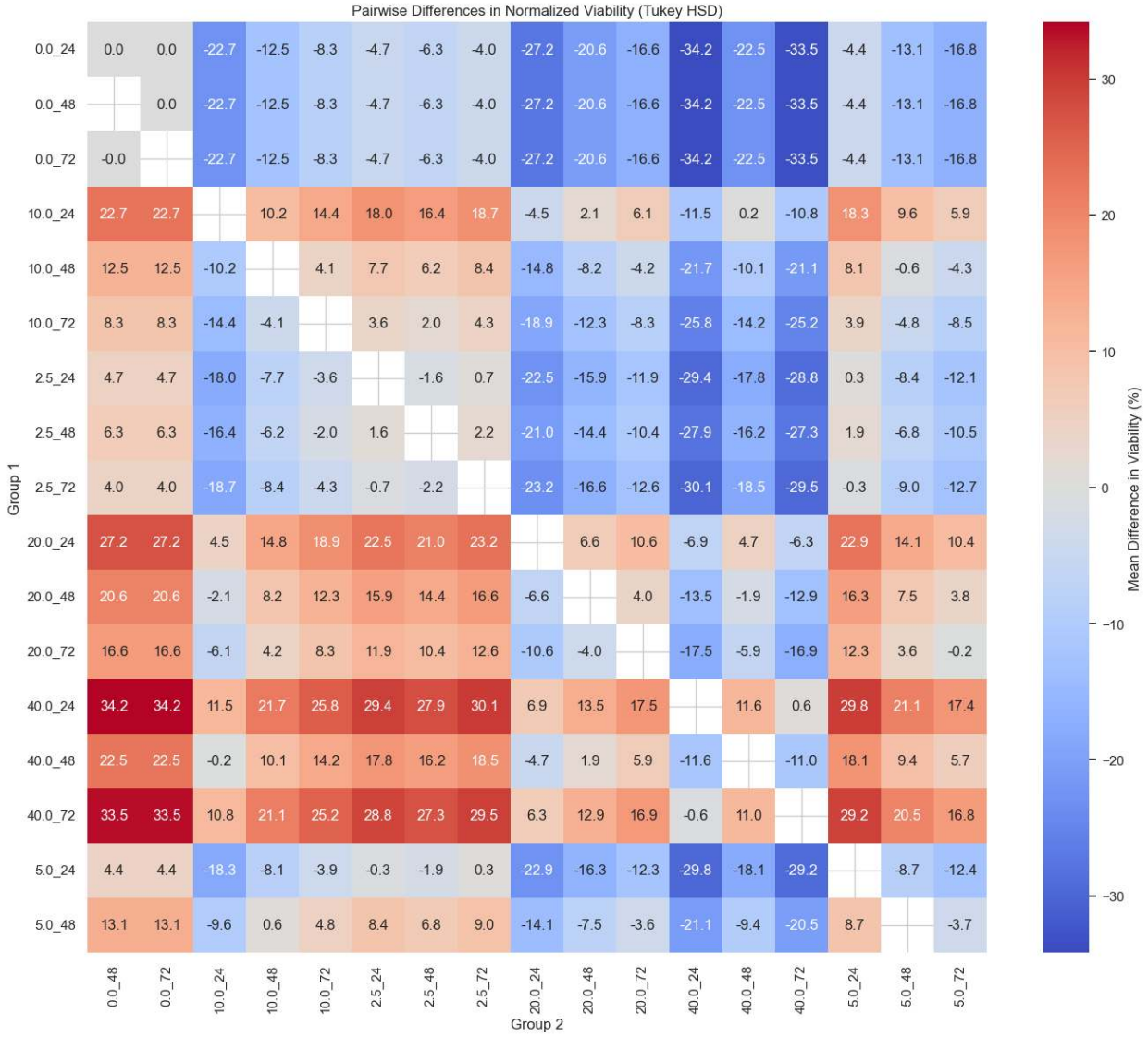

Figure 24. Heatmap visualization of pairwise differences in normalized SRB viability across all niraparib dose and timepoint combinations in HGrC1 cells. Mixed effects modelling of normalized SRB viability data, followed by Tukey's HSD post-hoc analysis, was used to assess pairwise differences across all dose-timepoint combinations

Table 2. The most significant changes in the HGRC1 cell line treated with Niraparib. Groups: Drug dose and timepoint for condition (format: Dose(µM)_Time(h))

Adjusted p-value: Tukey-adjusted p-value indicating significance of the comparison

Group 1	Group 2	Mean Difference (Viability %)	p value
0.0_72	40.0_72	-33.542	< 0.001
0.0_24	40.0_72	-33.542	< 0.001
0.0_24	40.0_24	-34.160	< 0.001
0.0_72	40.0_24	-34.160	< 0.001
0.0_48	40.0_72	-33.542	< 0.001
0.0_48	40.0_24	-34.160	< 0.001
2.5_72	40.0_24	-30.120	< 0.001
2.5_72	40.0_72	-29.502	< 0.001
40.0_24	5.0_24	29.784	< 0.001
2.5_24	40.0_24	-29.448	< 0.001
40.0_72	5.0_24	29.166	< 0.001
2.5_24	40.0_72	-28.830	< 0.001
2.5_48	40.0_24	-27.890	< 0.001

Dose-Dependent Effects of Niraparib and Olaparib on Primary Human Luteal Granulosa Cell Viability

After 72 and 96 hours of treatment with increasing doses of niraparib or olaparib, HLGCs were tested for cell viability using the MTT assay. This allowed to determine the dose- and time-dependent effects of these drugs on cell viability (Figure 25).

At 72 hours, cell viability showed a moderate decline across all treatment groups.

At 96 hours, a clearer dose-response pattern emerged. While the untreated control maintained the highest mean absorbance (indicating metabolic activity), exposure to Olaparib or Niraparib at 20 µM and 40 µM resulted in most reduced viability.

Cell viability progressively decreased with higher doses of Niraparib, with the 40 µM group showing the most pronounced reduction in formazan production compared to control (Figure 25.a.) Olaparib treatment led to a time- and dose-dependent reduction in metabolic activity, with the effect becoming more prominent at 96 hours, particularly at 40 µM (Figure 25.b.). These findings support a cumulative cytotoxic effect of Niraparib and Olaparib over time.

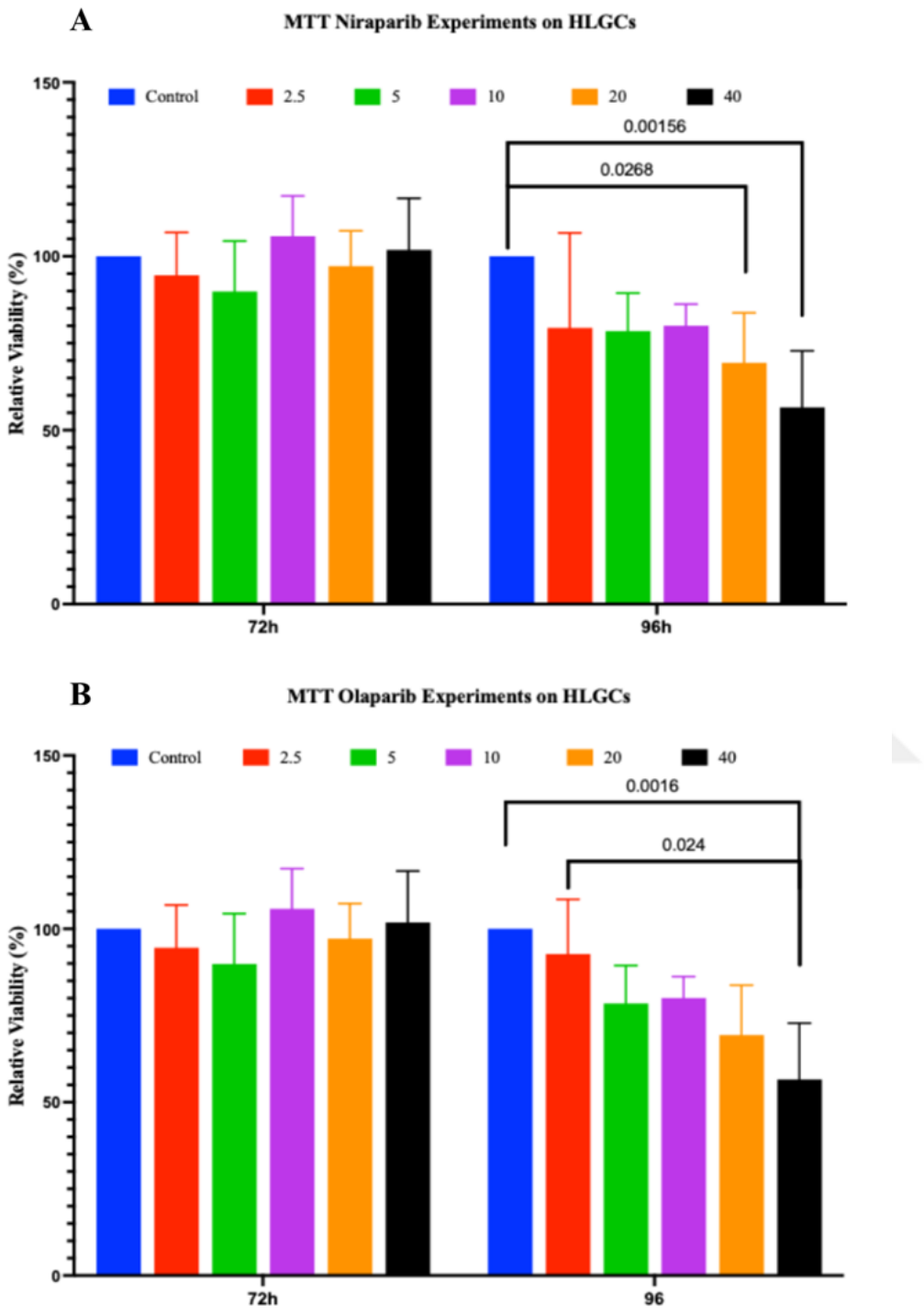

Figure 25. Dose- and Time-Dependent Effect of Niraparib and Olaparib on HLGCs Viability Assessed by MTT Assay.

After cells had been exposed to Niraparib (A) or Olaparib (B) at gradually increased concentrations (2.5–40 μM) for 96 hours, the MTT test was used to determine cell viability. The data from the MTT assay were analyzed using One-way Analysis of Variance (ANOVA) to evaluate differences in cell viability across treatment groups. Prior to ANOVA, data were assessed for normality using Shapiro-Wilk's test to confirm the appropriateness of parametric analyses. Cell viability rates were normalized against untreated controls (set at 100%) to standardize across biological replicates and minimize variability.

Olaparib-Induced Changes in Live and Dead Cell Fluorescence Signals in Primary Human Luteal Granulosa Cells

HLGCs were exposed to escalating doses of Olaparib for a duration of 96 hours. Cell viability and mortality were evaluated using quantitative fluorescence imaging with calcein (for living cells) and propidium iodide (PI; for dead cells) staining. Background removal and quantification were conducted for each fluorescence channel separately in ImageJ. The quantification of calcein fluorescence intensity demonstrated a significant dose-dependent reduction in live cell signal as Olaparib concentrations increased (Figure 26). Calcein intensity was considerably decreased at 20 μM ($P < 0.0001$) and 40 μM ($P < 0.0001$) compared to the control, and both concentrations were also significantly lower than 10 μM Olaparib ($P < 0.0001$ for all relevant pairwise comparisons). The fluorescence intensity of PI, indicative of the percentage of deceased or membrane-compromised cells, was considerably changed by Olaparib. The PI signal exhibited a substantial increase at 20 μM in comparison to the control ($P = 0.0006$). Unexpectedly, PI intensity at 40 μM was significantly lower than at 20 μM ($P < 0.0001$), showing a surprising decrease in signal from membrane-compromised cells at the greatest Olaparib concentration. The decrease in both signals at 40 μM may indicate significant cell death (resulting in insufficient cells for staining), alterations in dye absorption, or technical limitations arising from severe cytotoxicity. These findings underscore the intricate impact of high-dose Olaparib on granulosa cell survival and membrane integrity.

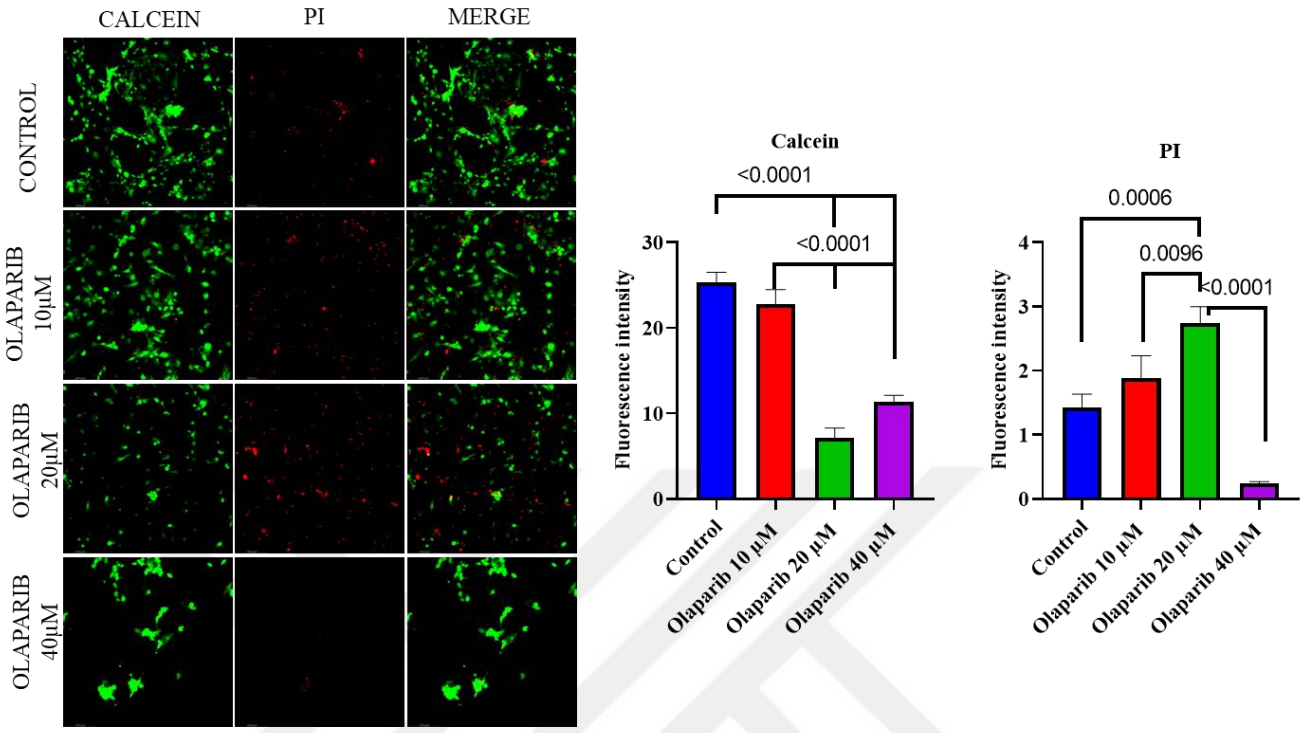

Figure 26. Representative Microscopy Images and Quantitative Assessment of Calcein and PI Signals in Olaparib-Treated HLGCs.

3.1.2 Cell Cycle Progression and Apoptosis

Cell Cycle Analysis via Flow Cytometry in COV434 and HGrC1 and Cell Lines

To examine the impact of PARPi on cell cycle progression, HGrC1 and COV434 human cell lines have been exposed to either Niraparib or Olaparib at doses of 2.5 µM, 5 µM, 10 µM, 20 µM, and 40 µM for durations of 24, 48, 72, and 96 hours. Post-treatment, cell cycle distribution was evaluated using flow cytometry to determine possible modifications in cell cycle dynamics resulting from escalating dosages and durations of PARP inhibition. Data derived from flow cytometry experiments were structured into a long format suitable for linear modelling, with variables including dose, exposure time, and cell cycle phases (G0/G1, S, G2/M) along with the proportion of dead cells. Ordinary Least Squares (OLS) regression models were fitted independently for each feature (Dead cells, G0/G1, S, G2/M), evaluating the main effects of dose and time, as well as their interaction terms. Model performance was assessed through R-squared and adjusted R-squared metrics.

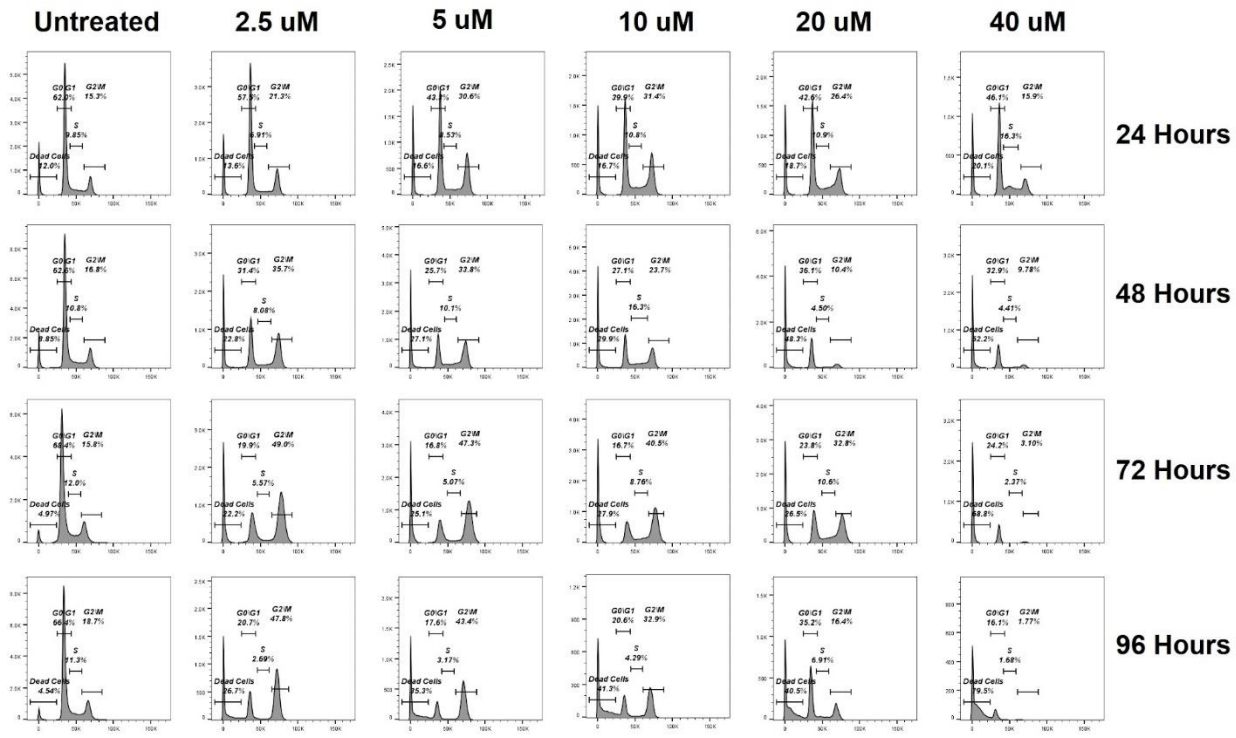

Figure 27. Cell cycle analysis of COV434 cells treated with Niraparib

In COV434 cells treated with Niraparib, the proportion of dead cells (Table 3) significantly increased at 96 hours (coefficient = +59.49 ± 4.88, $p < 0.001$), and a dose-dependent effect was also detected (coefficient = +0.869 ± 0.259, $p = 0.004$), with a model R^2 of 0.970.

Table 3. Linear model coefficients for dose- and time-dependent cell-cycle analysis of COV434 cells treated with Niraparib.

Outcome	Time effect at 96h (Coefficient ± SE)	Dose main effect (p)	Dose × Time at 96h (Coefficient ± SE, p)	Model R^2
Dead Cells	+59.49 ± 4.88 ($p < 0.001$)	0.933	+0.869 ± 0.259 ($p = 0.004$)	0.970

Outcome	Time effect at 96h (Coefficient ± SE)	Dose main effect (p)	Dose × Time at 96h (Coefficient ± SE, p)	Model R^2
G0/G1 phase	−41.86 ± 4.96 ($p < 0.001$)	0.343	−0.818 ± 0.263 ($p = 0.007$)	0.942
G2/M phase	−11.48 ± 2.37 ($p < 0.001$)	0.422	NS ($p = 0.621$)	0.818
S phase	−6.96 ± 1.17 ($p < 0.001$)	−0.122 ($p = 0.013$)	NS ($p = 0.666$)	0.881

The G0/G1 phase decreased significantly over time (coefficient = −41.86 ± 4.96, $p < 0.001$) and also exhibited a significant dose-dependent reduction (coefficient = −0.818 ± 0.263, $p = 0.007$), with a model R^2 of 0.942. G2/M phase showed a time-dependent decline (coefficient = −11.48 ± 2.37, $p < 0.001$) without any significant dose-dependent change ($p = 0.621$), with a model R^2 of 0.818. S phase also declined over time (coefficient = −6.96 ± 1.17, $p < 0.001$), without significant dose modulation ($p = 0.666$), and had a model R^2 of 0.881 (Table 3).

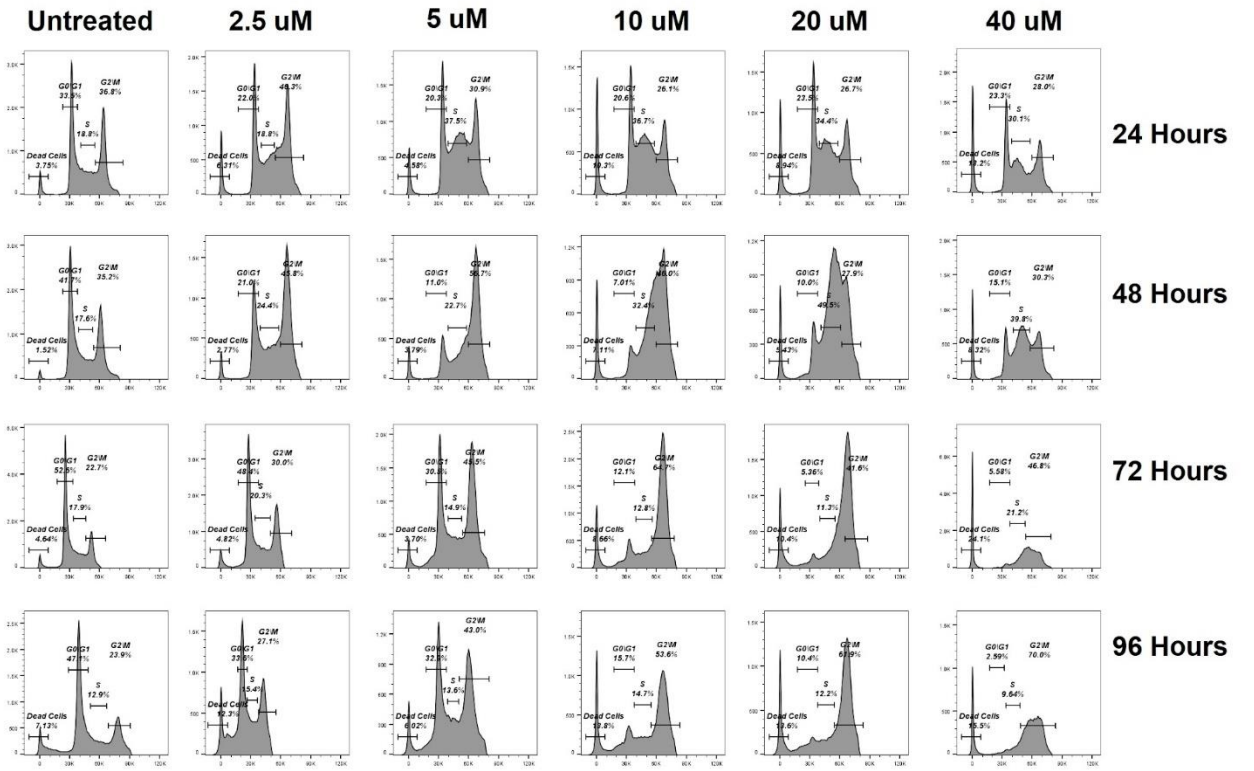

Figure 28. Cell cycle analysis of HGrC1 cells treated with Niraparib

In Niraparib-treated HGRC1 cells, the percentage of dead cells increased at 96 hours (coefficient = +3.86 ± 1.73, p = 0.041) and with dose (coefficient = +0.213 ± 0.065, p = 0.005), with a significant dose × time interaction at 72 hours (coefficient = +0.284 ± 0.092, p = 0.007), and a model R^2 of 0.875. G0/G1 phase showed no main effect of time or dose but exhibited a dose × time interaction at 72 hours (coefficient = −1.049 ± 0.463, p = 0.038) and a borderline effect at 96 hours (coefficient = −0.909 ± 0.463, p = 0.067), with a model R^2 of 0.598. S phase decreased significantly over time (coefficient = −12.47 ± 5.54, p = 0.039), with no significant dose or interaction effects, and a model R^2 of 0.722. G2/M phase showed no significant main effects of time or dose but demonstrated a significant dose × time interaction at 96 hours (coefficient = +1.375 ± 0.452, p = 0.008), with a model R^2 of 0.567 (Table 4).

Table 4. Linear model coefficients for dose- and time-dependent cell-cycle analysis of HGRC1 cells treated with Niraparib.

Outcome	Time effect at 96h (Coefficient ± SE, *p*)	Dose main effect (*p*)	Dose × Time at 96h (Coefficient ± SE, *p*)	Model R^2
Dead Cells	+3.86 ± 1.73 (*p* = 0.041)	+0.21 ± 0.07 (*p* = 0.005)	NS (−0.02 ± 0.09), (*p* = 0.801)	0.875
G0/G1 phase	NS (+11.46 ± 8.72), (*p* = 0.207)	NS(−0.08 ± 0.33), (*p* = 0.821)	−0.91 ± 0.46 (*p* = 0.067)	0.598
S phase	−12.47 ± 5.54 (*p* = 0.039)	NS(+0.19 ± 0.21), (*p* = 0.371)	NS (−0.30 ± 0.29), (*p* = 0.320)	0.722
G2/M phase	NS(−3.34 ± 8.52), (*p* = 0.700)	NS(−0.29 ± 0.32), (*p* = 0.376)	+1.38 ± 0.45 (*p* = 0.008)	0.567

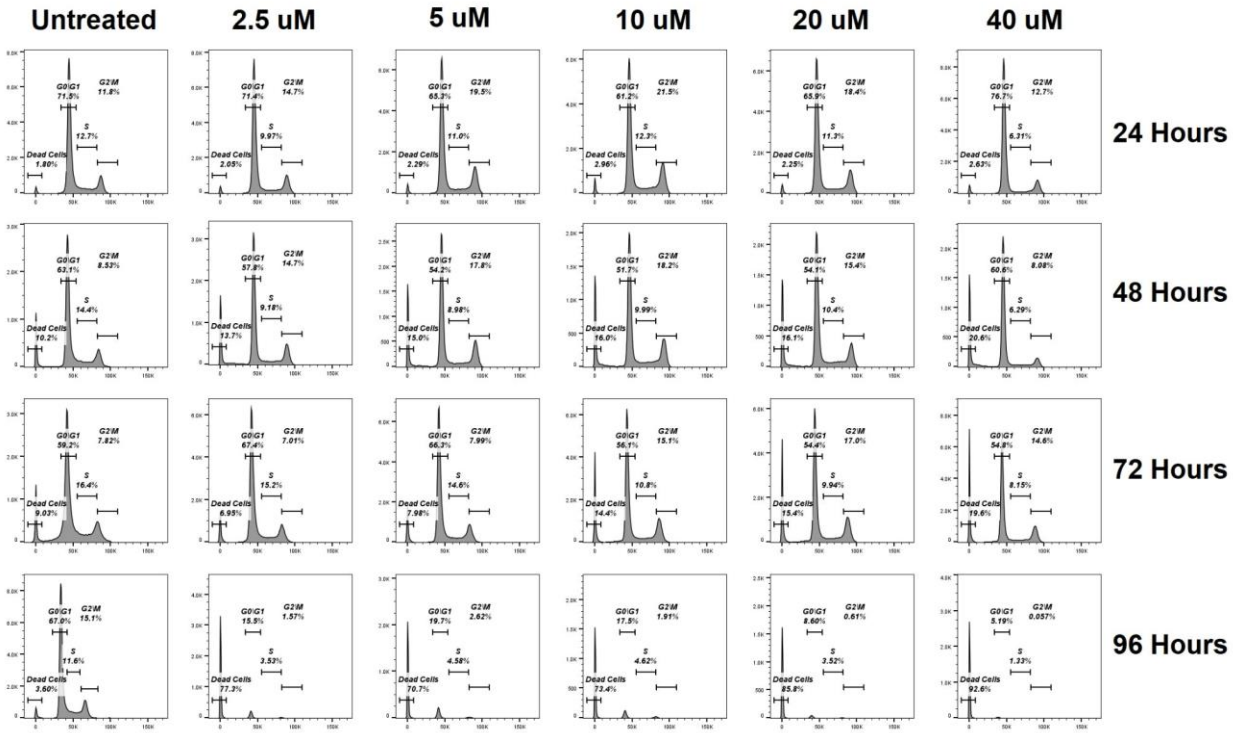

Figure 29. Cell cycle analysis of COV434 cells treated with Olaparib

Olaparib treatment in COV434 cells led to increased dead cell accumulation at 96 hours (coefficient = +48.05 ± 11.31, $p < 0.001$), along with a dose-dependent effect (coefficient = +1.31 ± 0.60, $p = 0.045$), with a model R^2 of 0.843. G0/G1 phase decreased over time (coefficient = −32.55 ± 8.73, $p = 0.002$) and with dose (coefficient = −1.07 ± 0.46, $p = 0.034$), with a model R^2 of 0.815. S phase exhibited a time-dependent decrease (coefficient = −4.99 ± 1.64, $p = 0.008$), while dose had no significant effect ($p = 0.336$), with a model R^2 of 0.810. G2/M phase declined over time (coefficient = −10.69 ± 3.57, $p = 0.009$) but was not significantly influenced by dose ($p = 0.404$), with a model R^2 of 0.671.

Table 5. Linear model coefficients for dose- and time-dependent cell-cycle analysis of COV434 cells treated with Olaparib.

Outcome	Time effect at 96h (Coefficient ± SE, *p*)	Dose main effect (*p*)	Dose × Time at 96h (Coefficient ± SE, *p*)	Model R^2
Dead Cells	+48.05 ± 11.31 (*p* < 0.001)	0.974	+1.31 ± 0.60 (*p* = 0.045)	0.843
G0/G1 phase	−32.55 ± 8.73 (*p* = 0.002)	0.631	−1.07 ± 0.46 (*p* = 0.034)	0.815
S phase	−4.99 ± 1.64 (*p* = 0.008)	0.281	NS (*p* = 0.336)	0.810
G2/M phase	−10.69 ± 3.57 (*p* = 0.009)	0.753	NS (*p* = 0.404)	0.671

In HGRC1 cells, Olaparib exposure led to a significant increase in dead cells by 96 hours (coefficient = +6.40 ± 0.90, $p < 0.001$), with a strong dose-dependent effect (coefficient = +0.343 ± 0.047, $p < 0.001$), and a model R^2 of 0.974. G0/G1 phase increased over time (coefficient = +10.02 ± 4.03, $p = 0.024$) but decreased with dose (coefficient = −0.424, $p = 0.013$), with no significant dose × time interaction at 96 hours ($p = 0.656$), and a model R^2 of 0.733. G2/M phase declined over time (coefficient = −21.76 ± 3.59, $p < 0.001$) and increased with dose (coefficient = +0.466, $p = 0.003$), with no significant interaction term ($p = 0.056$), and a model R^2 of 0.892. S

phase also decreased over time (coefficient = −1.41 ± 0.44, p = 0.005), with a modest dose-dependent decline (coefficient = −0.037, p = 0.038), and no interaction at 96 hours (p = 0.756), with a model R^2 of 0.912.

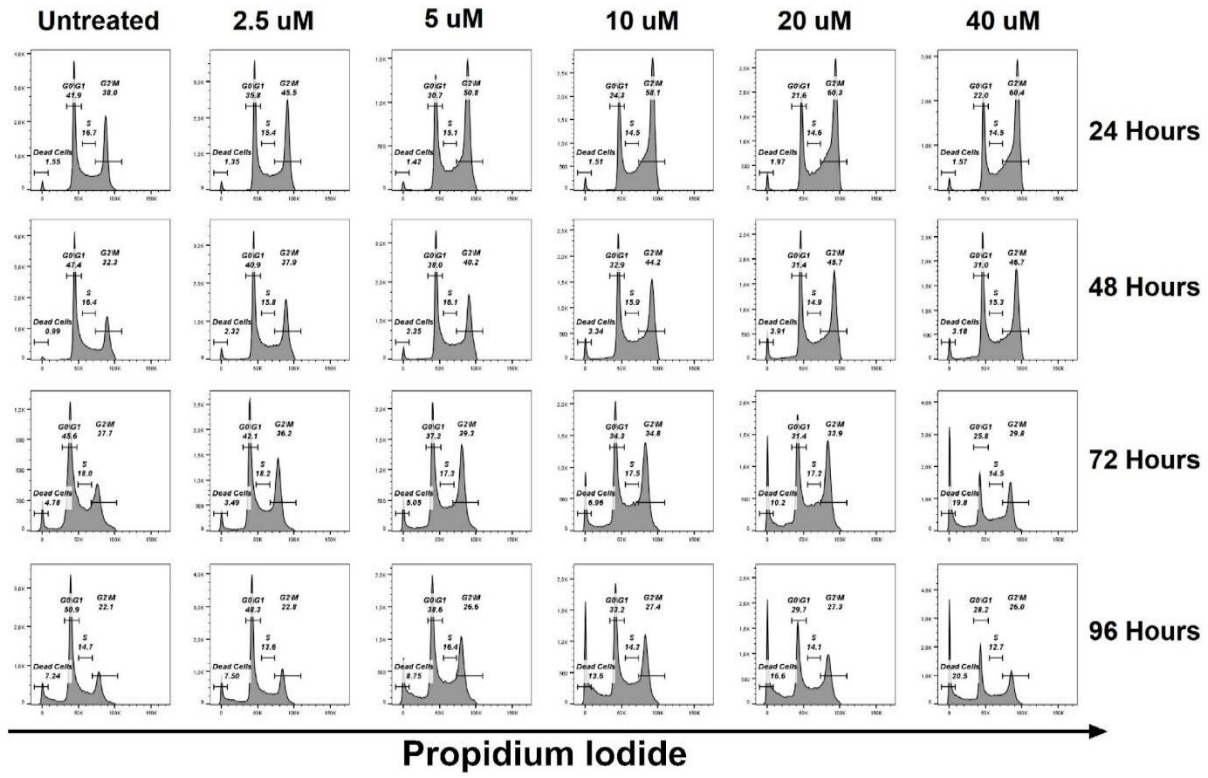

Figure 30. Cell cycle analysis of HGrC1 cells treated with Olaparib

Table 6. Linear model coefficients for dose- and time-dependent cell-cycle analysis of HGRC1 cells treated with Olaparib

Outcome	Time effect at 96h (Coefficient ± SE)	Dose main effect (p)	Dose × Time at 96h (Coefficient ± SE, p)	Model R^2
Dead Cells	+6.35 ± 0.89 (p < 0.001)	0.895	+0.343 ± 0.047 (p < 0.001)	0.974
G0/G1 phase	+10.02 ± 4.03 (p = 0.024)	−0.424 (p = 0.013)	NS (p = 0.656)	0.733

Outcome	Time effect at 96h (Coefficient ± SE)	Dose main effect (p)	Dose × Time at 96h (Coefficient ± SE, p)	Model R^2
G2/M phase	−21.76 ± 3.59 ($p < 0.001$)	+0.466 ($p = 0.003$)	NS ($p = 0.056$)	0.892
S phase	−1.41 ± 0.44 ($p = 0.005$)	−0.037 ($p = 0.038$)	NS ($p = 0.756$)	0.912

Apoptosis and Viability Assessment in Primary Human Luteal Granulosa Cells by Flow Cytometry

In an effort to evaluate the influence of PARP inhibition on apoptosis and cellular mortality, HLGCs were subjected to escalating doses of Olaparib for a duration of 72 hours. Post-treatment, flow cytometric analysis was conducted to evaluate apoptosis using the measurement of cleaved PARP expression and to assess cell viability with the Zombie dye. Dose-response relationships for variables such as cleaved PARP (cPARP) and dead cell rates were evaluated using pairwise Δ/Δ slope analysis. The Δ/Δ slopes were calculated by assessing differences in response relative to incremental dose increases between specified intervals. Results were visualized graphically, highlighting the observed responses and corresponding slope values between intervals.

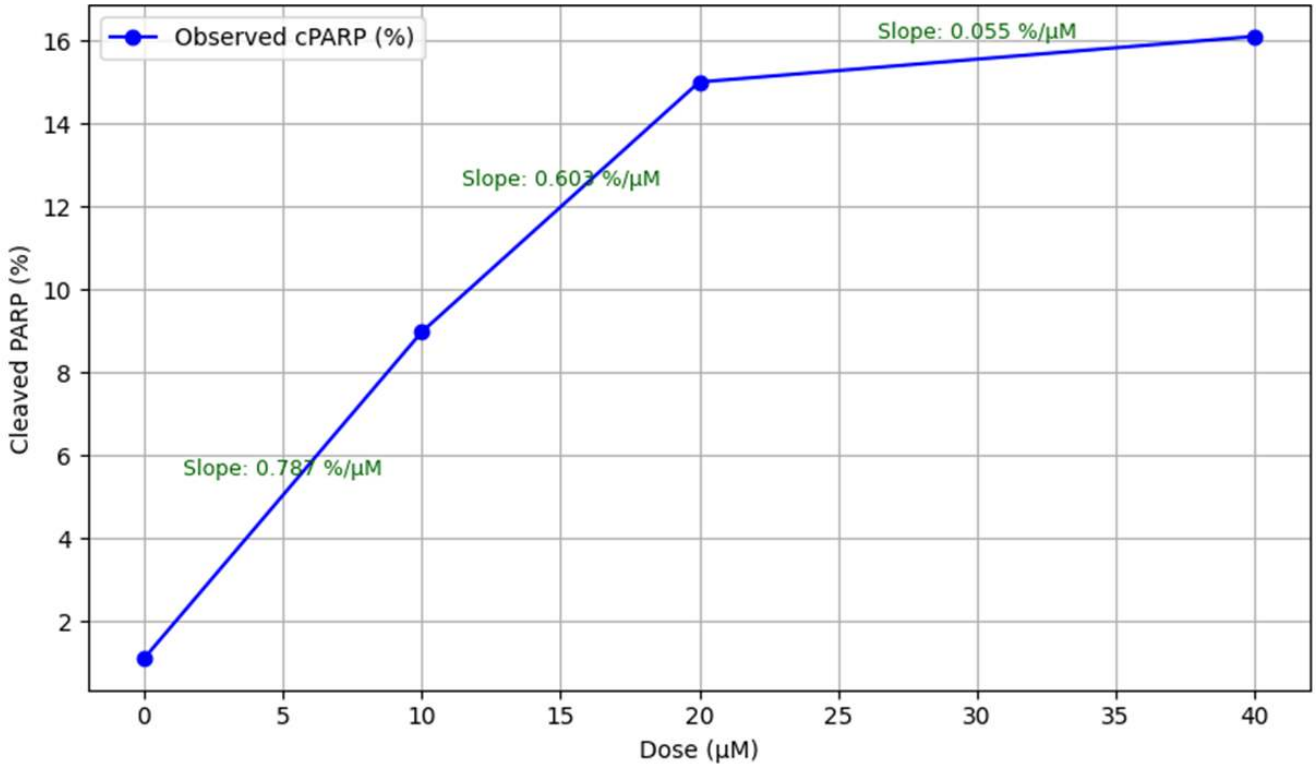

Figure 31. Pairwise Δ/Δ slope visualization showing the change in cleaved PARP (%) between 10 µM, 20 µM, and 40 µM Olaparib.

A dose-dependent increase was observed in both apoptosis marker. For cleaved PARP (%), the increase was most pronounced between 0 and 10 µM, with a slope of 0.78%/µM from 0 to 10 µM and 0.60%/µM between 10 and 20 µM, indicating a steep induction of apoptosis at lower doses. Between 20 and 40 µM, the slope plateaued to 0.055%/µM, suggesting a saturation effect at higher concentrations (Figure 31).

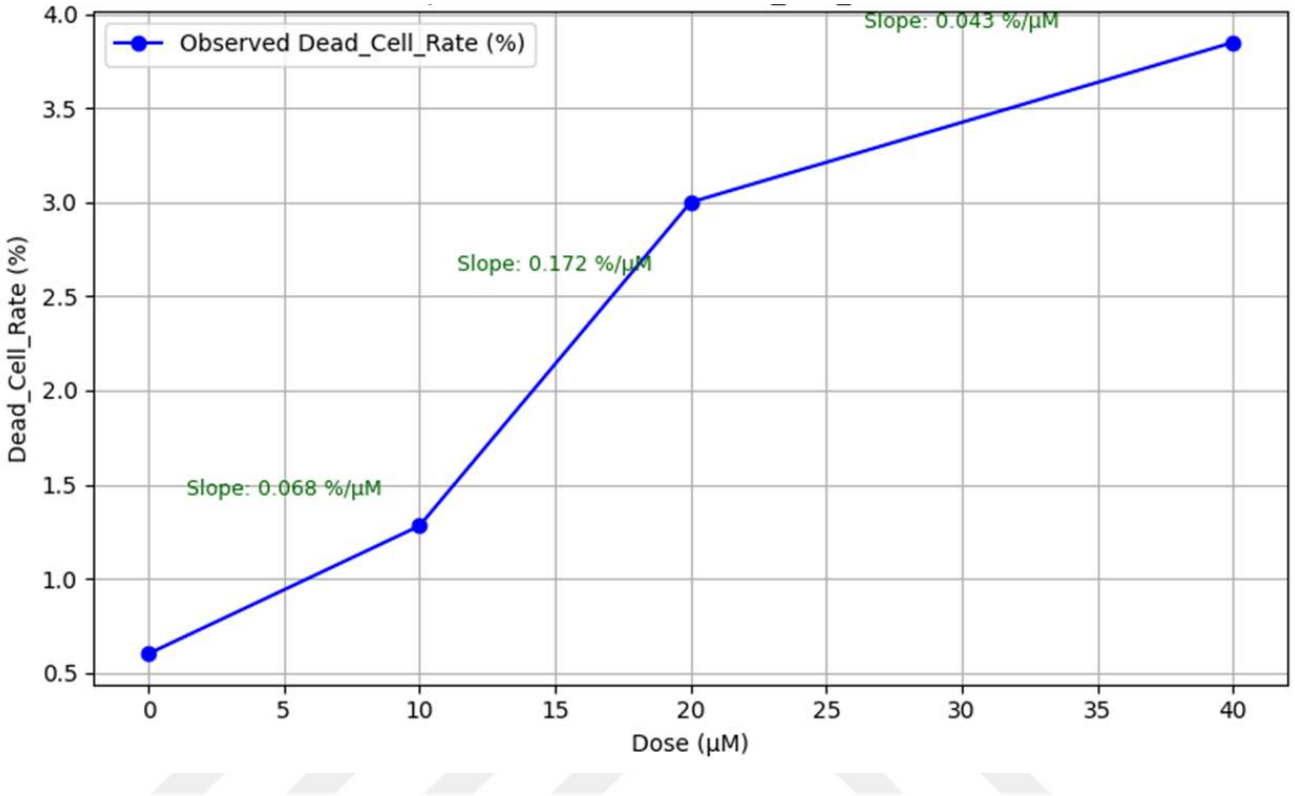

Figure 32. Pairwise Δ/Δ slope visualization showing the change in Dead Cell Rate (%) between 10 µM, 20 µM, and 40 µM Olaparib

Similarly, dead cell rates increased with Olaparib dose, with a maximal slope of 0.172%/µM between 10 and 20 µM, preceded by a 0.068%/µM slope from 0 to 10 µM, and tapering off to 0.043%/µM at the 20–40 µM range (Figure 32). These findings suggest that luteal cells respond robustly to intermediate concentrations of Olaparib, with diminishing incremental effects observed beyond 20 µM, consistent with a saturation of apoptotic and cytotoxic mechanisms.

Detection of Apoptosis-Related Proteins by Western Blot in Human Granulosa Cell Lines

Following 72 and 96 hours of HGrC1 cell exposure to Olaparib at doses of 2,5 µM, 5 µM, 10 µM, 20 µM, and 40 µM, Western blot analysis was conducted to assess the expression of cleaved PARP. No recognizable signal for either protein was seen in the untreated control, but all Olaparib-treated groups had clear bands (Figures 33 and 34). Nonetheless, quantitative intensity

analysis indicated no statistically significant changes between the treatment groups at any time point.

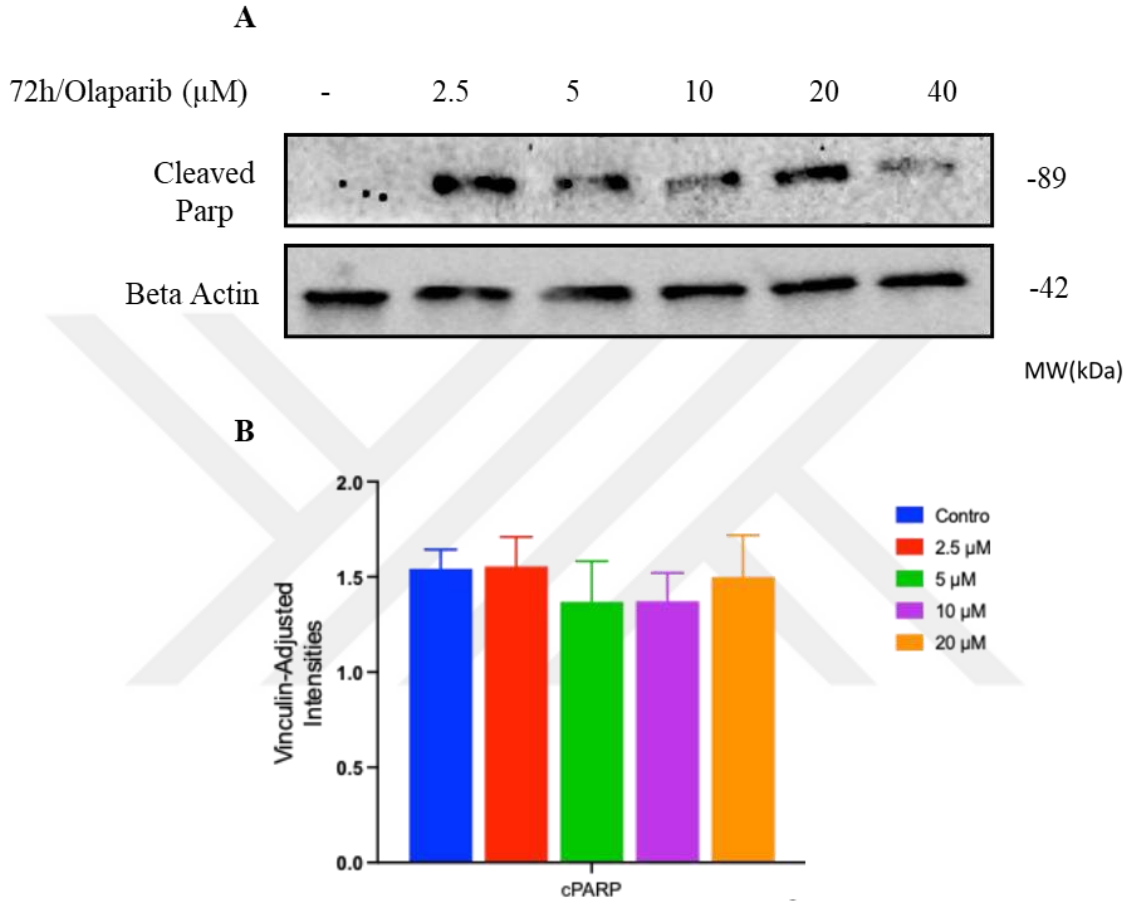

Figure 33. Expression of cleaved PARP in HrGC1 after 72 hours of exposure to Olaparib. (A) Representative Western blot images showing cleaved PARP expression across different Olaparib concentrations (2,5 µM, 5 µM, 10 µM, 20 µM, and 40 µM) compared with the untreated control. (B) Quantification of cleaved PARP band intensities normalized to Beta Actin. Data are presented as mean ± SEM.

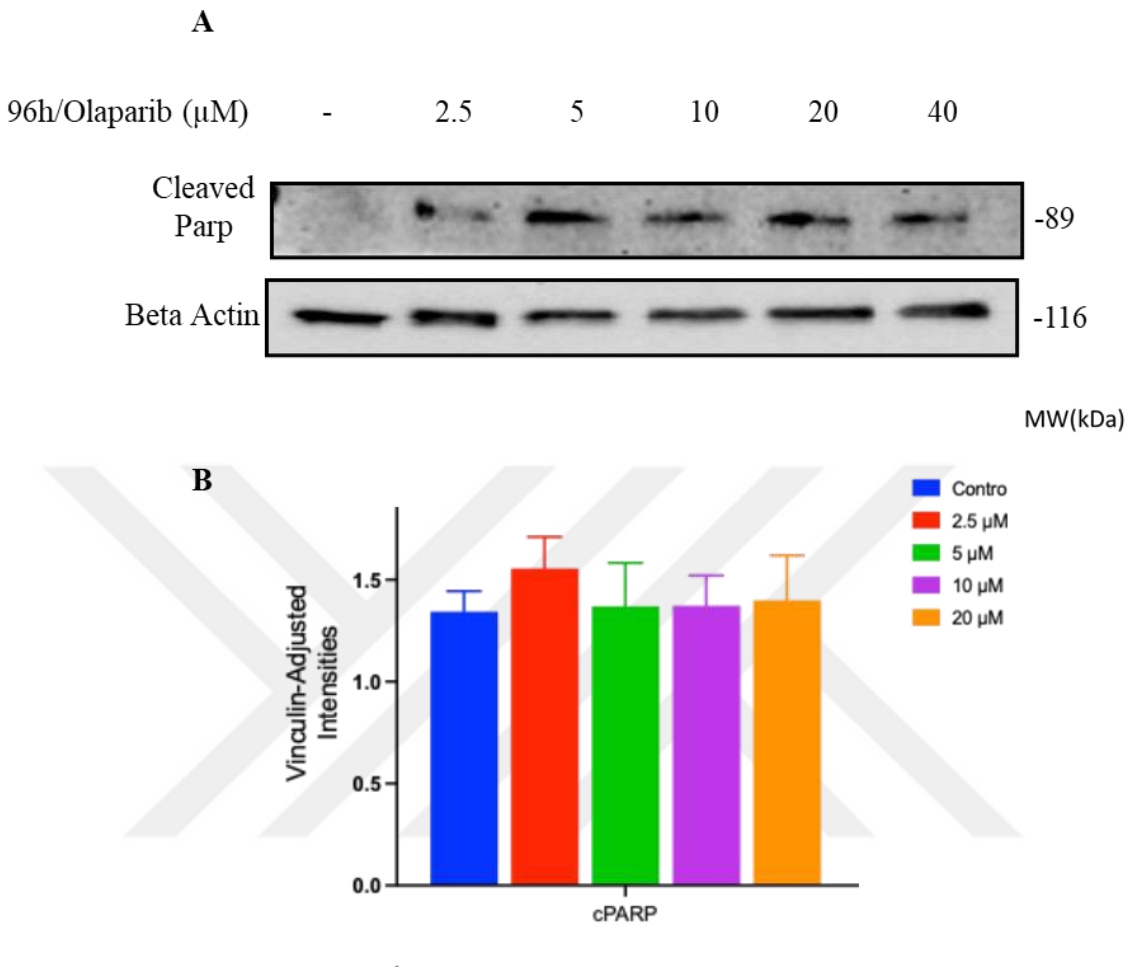

Figure 34. Expression cleaved PARP in HrGC1 after 96 hours of exposure to Olaparib. (A) Representative Western blot images showing cleaved PARP expression across different Olaparib concentrations compared with control. (B) Quantification of cleaved PARP band intensities normalized to Beta Actin. Data are expressed as mean ± SEM.

Following 72 hours exposure of HLGCs cells to Niraparib at concentrations of 2,5 µM, 5 µM, 10 µM, 20 µM, and 40 µM, Western blot analysis revealed a clear rise in cleaved PARP expression compared with the untreated control. This elevation was statistically significant at 2.5 µM ($p = 0.029$) and 5 µM ($p = 0.004$), and highly significant at 10, 20, and 40 µM ($p < 0.0001$) (Figure 35).

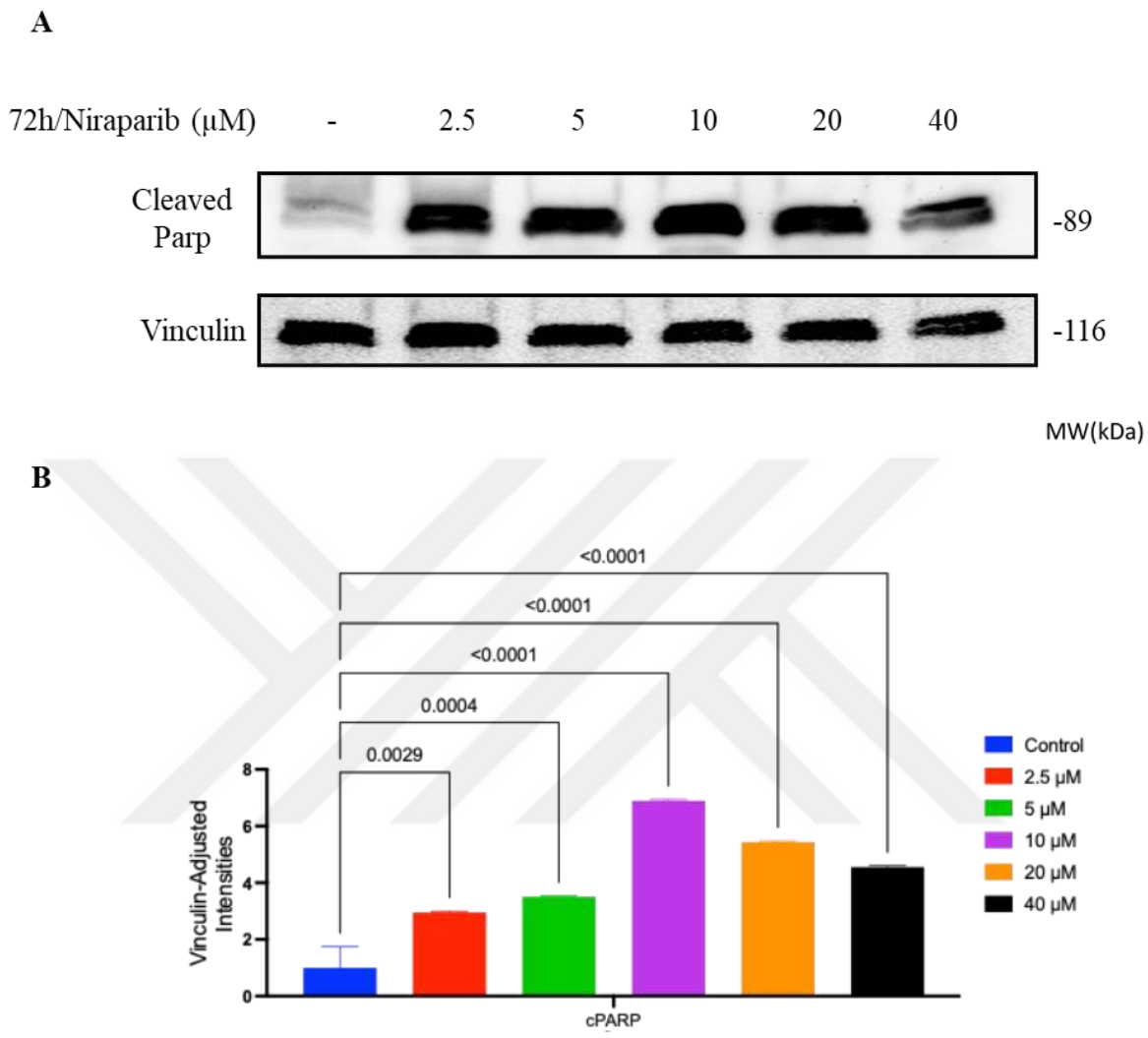

Figure 35. Cleaved PARP expression in HLGCs after 72 hours exposure to Niraparib. (A) Representative Western blot images showing cleaved PARP expression across different Niraparib concentrations (2,5 µM, 5 µM, 10 µM, 20 µM, and 40 µM) compared with the untreated control. (B) Quantification of cleaved PARP band intensities normalized to vinculin. Data are presented as mean ± SEM.

When HLGCs cells were exposed to Olaparib for 96 hours at 20 µM and 40 µM, Western blot analysis revealed a marked increase in total PARP expression at both concentrations, with statistical significance ($p < 0.0001$) compared with the untreated control (Figure 36). Cleaved PARP levels showed a slight upward trend in the treated groups; however, there was no statistically significant change in these variables.

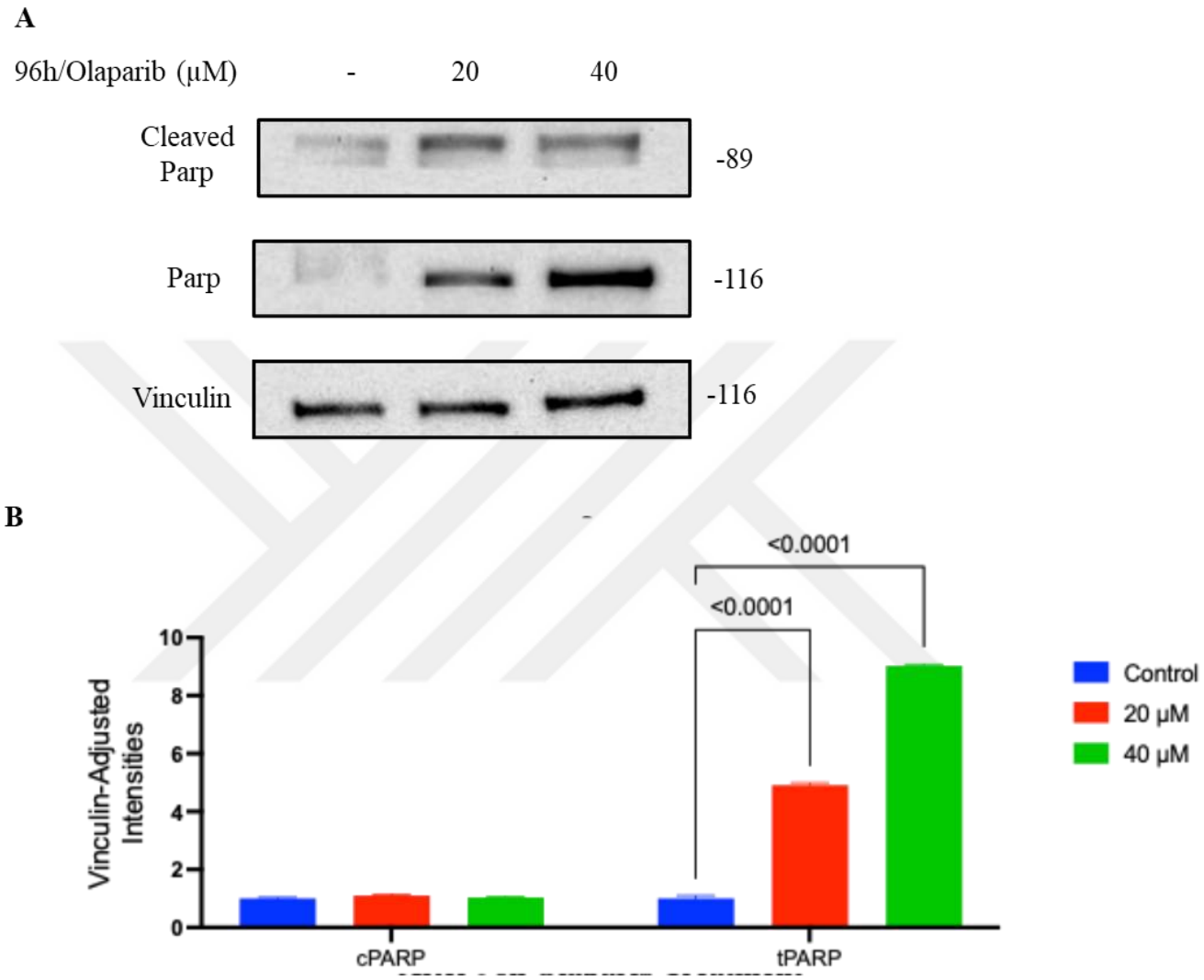

Figure 36. Cleaved PARP and total PARP expression in HGLCs after 96 hours exposure to Olaparib. (A) Representative Western blot images showing total PARP and cleaved PARP expression in control, 20 μM, and 40 μM Olaparib-treated groups. (B) Quantification of cleaved PARP and total PARP band intensities normalized to vinculin. Data are expressed as mean ± SEM.

3.1.3 Steroidogenic Activity and Hormone Secretion in Human Luteal Granulosa Cells

Regulation of Steroidogenic Gene and Protein Expression

The possible transcriptional effects of Olaparib were investigated using PCR analysis on HLGCs treated with 40 µM for 72 hours. GAPDH served as the housekeeping gene, and fold changes were determined in relation to untreated controls. An unpaired t-test was used for statistical analysis.

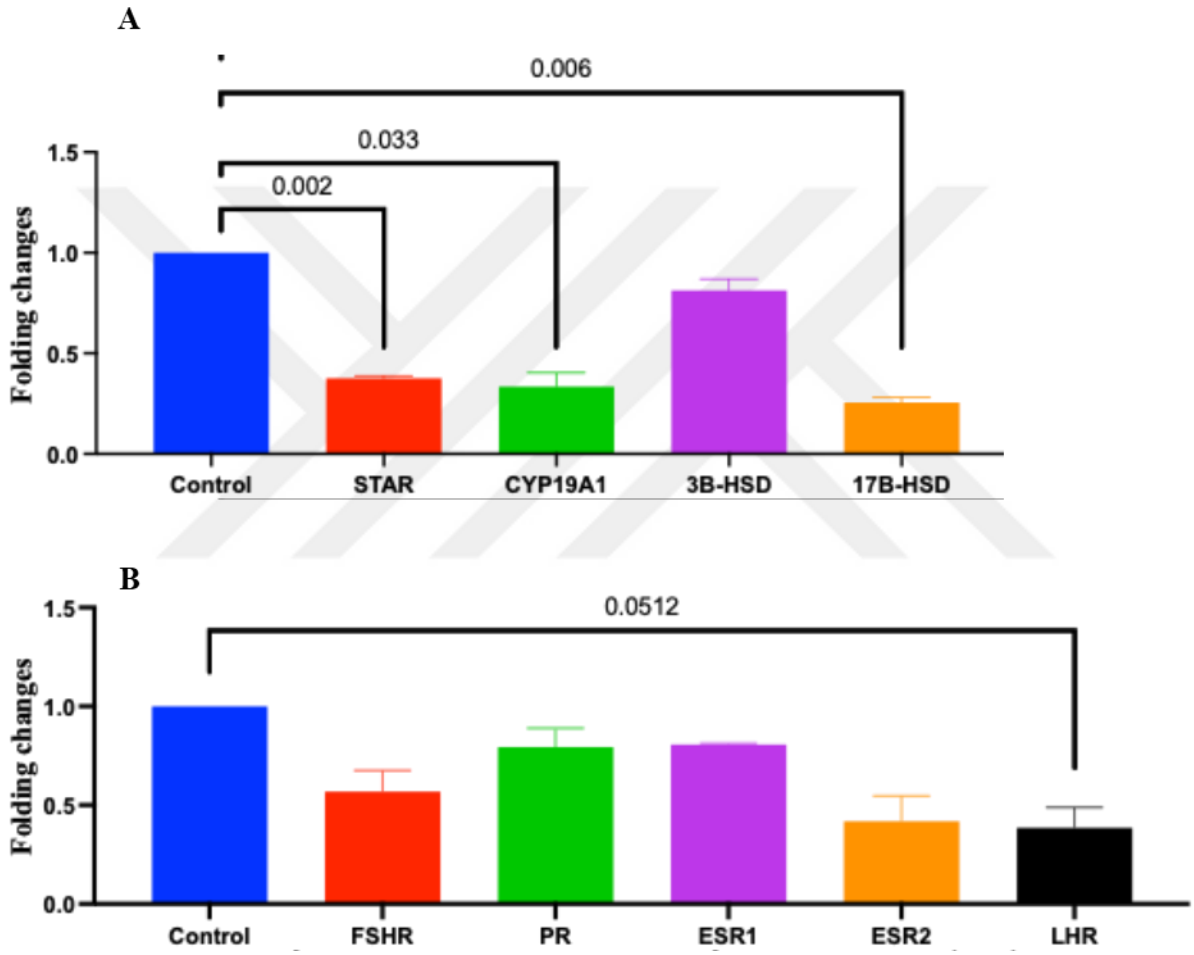

Figure 37. Relative mRNA expression (fold change versus control, normalized to GAPDH) of key (A) steroidogenic genes (StAR, CYP19A1, 17β-HSD, 3β-HSD) and (B) hormone receptors (FSHR, PR, ESR1, ESR2, LHR) in control and Olaparib-treated cells for 72 hours, measured by qPCR.

The expression of essential steroidogenic genes was evaluated (Figure 37.a.). In comparison to controls, Olaparib therapy markedly decreased the expression of STAR (P = 0.002), CYP19A1 (P = 0.033), and 17β-HSD (P = 0.006). The expression of 3β-HSD was decreased in the therapy

group; however, this decrease did not achieve statistical significance. The expression of gonadotropin and steroid hormone receptors, including FSHR, PR, ESR1, ESR2, and LHR, was assessed (Figure 37.b.). All targets exhibited reduced
expression in the Olaparib-treated cohort relative to controls, with only LHR nearing statistical significance (P = 0.0512).

To further evaluate whether the transcriptional alterations observed at the mRNA level are reflected at the protein level, Western blot analysis was performed in HLGCs following 72 hours and 96 hours of Olaparib treatment. When HLGCs were treated with Olaparib (20 and 40 µM) for 72 hours, Western blot analysis showed some protein-specific alterations in steroidogenic markers. 3β-HSD expression remained unchanged at both concentrations compared with the untreated control. StAR levels were reduced in both treated groups, with the decrease at 40 µM reaching statistical significance ($p = 0.0086$). Aromatase expression was unaltered at 20 µM but, interestingly, significantly increased at 40 µM ($p = 0.0018$) relative to control (Figure 38).

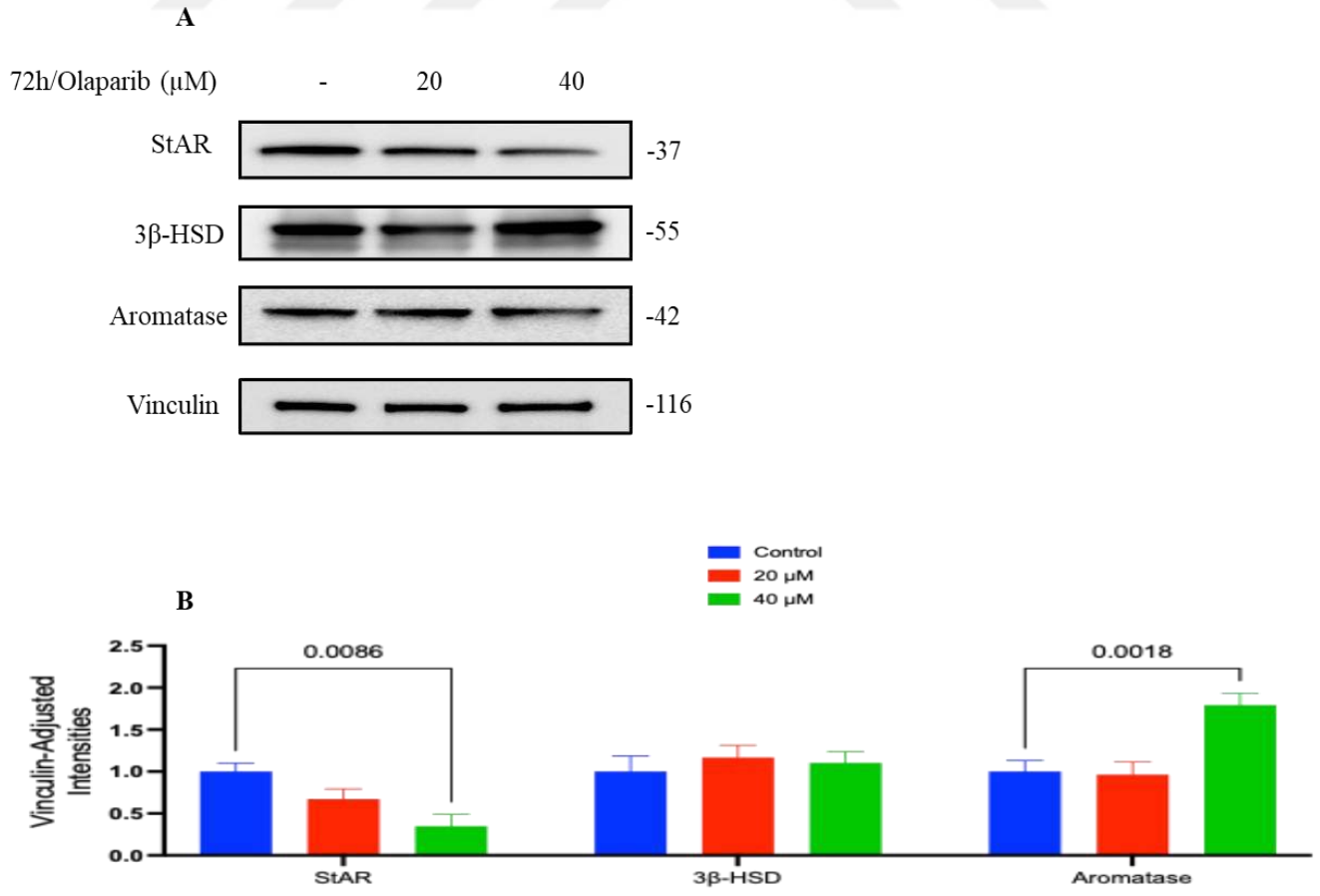

Figure 38. Expression of StAR, 3β-HSD, and aromatase proteins in HLGCs after 72 hours exposure to Olaparib. (A) Representative Western blot images showing StAR, 3β-HSD, and aromatase expression in control, 20 µM, and 40 µM Olaparib-treated groups. (B) Quantification of StAR, 3β-HSD, and aromatase band intensities normalized to vinculin. Data are expressed as mean ± SEM.

Extending Olaparib exposure to 96 h produced a similar overall pattern. 3β-HSD levels again showed no change at either concentration, and StAR expression was significantly reduced only at 40 µM ($p = 0.0481$). Aromatase expression remained unaltered at 20 µM, while a slight, non-significant increase was observed at 40 µM (Figure 39).

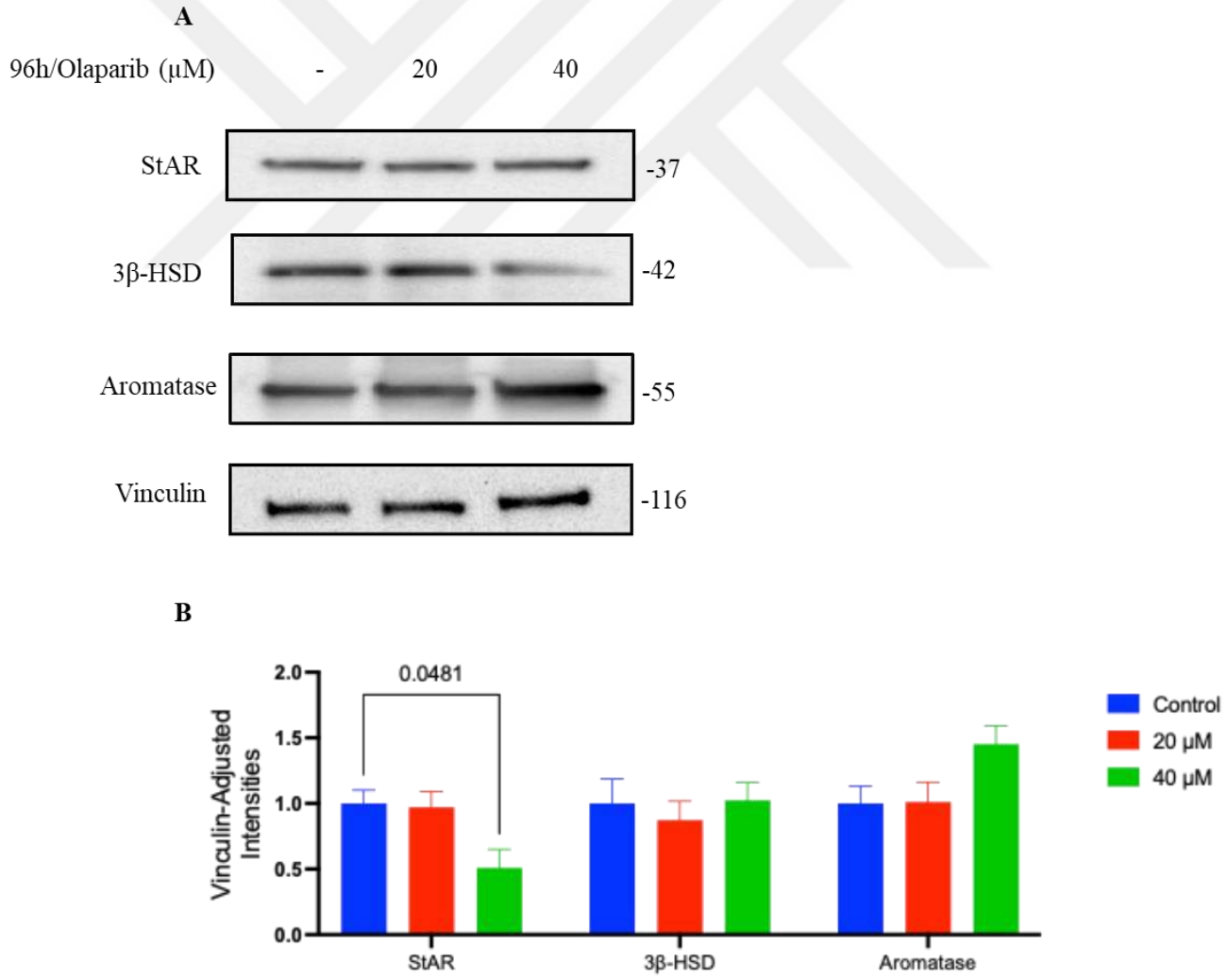

Figure 39. Expression of StAR, 3β-HSD, and aromatase proteins in HLGCs after 96 hours exposure to Olaparib. (A) Representative Western blot images showing StAR, 3β-HSD, and

aromatase expression in control, 20 μM, and 40 μM Olaparib-treated groups. (B) Quantification of StAR, 3β-HSD, and aromatase band intensities normalized to vinculin. Data are expressed as mean ± SEM.

Effects on Hormone Secretion

In order to assess the effects of PARP inhibition on the generation of estradiol, HLGCs were exposed to Niraparib or Olaparib at doses of 20 μM and 40 μM for a duration of 96 hours. The assessment of estradiol concentrations in the culture media indicated no substantial variations among the treatment groups. Niraparib and Olaparib, at the evaluated doses, did not affect estradiol secretion relative to untreated controls (Figure 40.a). To investigate the effect of PARPi on progesterone production, HLGCs were exposed to 20 μM or 40 μM doses of Niraparib or Olaparib for 96 hours. One-way ANOVA revealed substantial differences in progesterone production between the treatment groups ($p < 0.0001$). It was found by post-hoc analysis that, except for the comparison between 40 μM Olaparib and 20 μM Niraparib, there were statistically significant results from every pairwise comparison between treatment groups ($p < 0.05$). Data demonstrate that both PARPi, at different doses, exert significant impacts on progesterone production in granulosa cells (Figure 40.b).

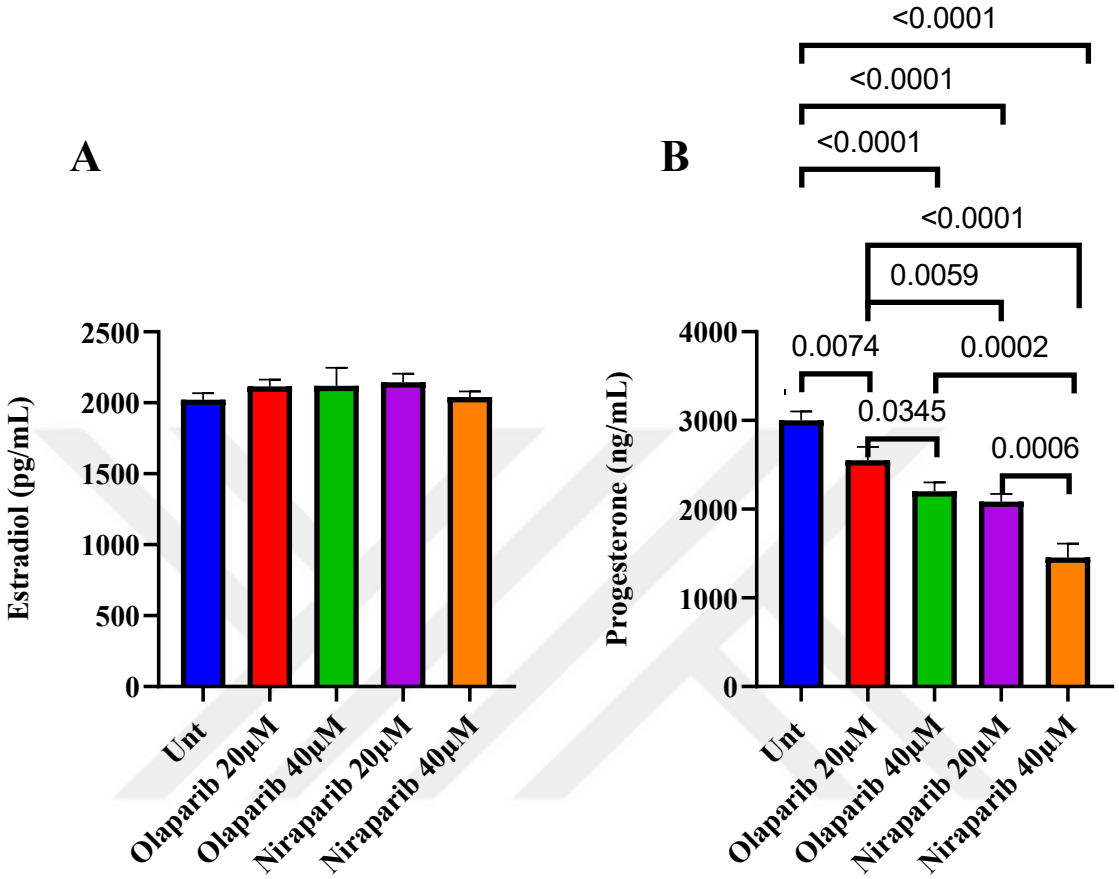

Figure 40. Effects of 96-hour PARPi treatment on steroid hormone secretion in primary granulosa cells (A) Effect of Niraparib and Olaparib on estradiol secretion in HLGCs after 96 hours of treatment. (B) Effect of Niraparib and Olaparib on progesterone secretion in HLGCs after 96 hours of treatment. A one-way ANOVA and Tukey's multiple comparisons test were used for statistical analysis. Mean ± SD is how the data is presented.

The prior research concentrated on assessing the effects of elevated and clinically relevant doses (20 and 40 µM) of Niraparib and Olaparib throughout an extended 96-hour treatment duration. Although these settings facilitated the discovery of significant changes in Progesterone synthesis at high PARPi dosages, it remained uncertain whether lower concentrations or shorter exposures might similarly affect steroidogenesis in HLGCs. A comprehensive dose-response investigation using a wider spectrum of niraparib concentrations (2.5–40 µM) across a 72-hour incubation period was conducted. This method facilitated the evaluation of the threshold and dynamics of

niraparib's impact on progesterone and estradiol secretion. The assessment of estradiol levels revealed no statistically significant variations across treatment groups, suggesting that shorter exposure to Niraparib also does not influence estradiol secretion under these settings (Figure 41.a). Conversely, the examination of progesterone levels demonstrated a significant and dose-dependent decrease in secretion at all Niraparib doses relative to the untreated (one-way ANOVA, $p < 0.0001$). Subsequent research revealed that all groups treated with Niraparib had markedly reduced progesterone levels compared to the untreated group (Tukey's test, $p < 0.0001$ for all comparisons). Progesterone secretion varied substantially across multiple intermediate dosage groups, with the most substantial decrease seen at 10 µM, 20 µM, and 40 µM Niraparib (Figure 41.b).

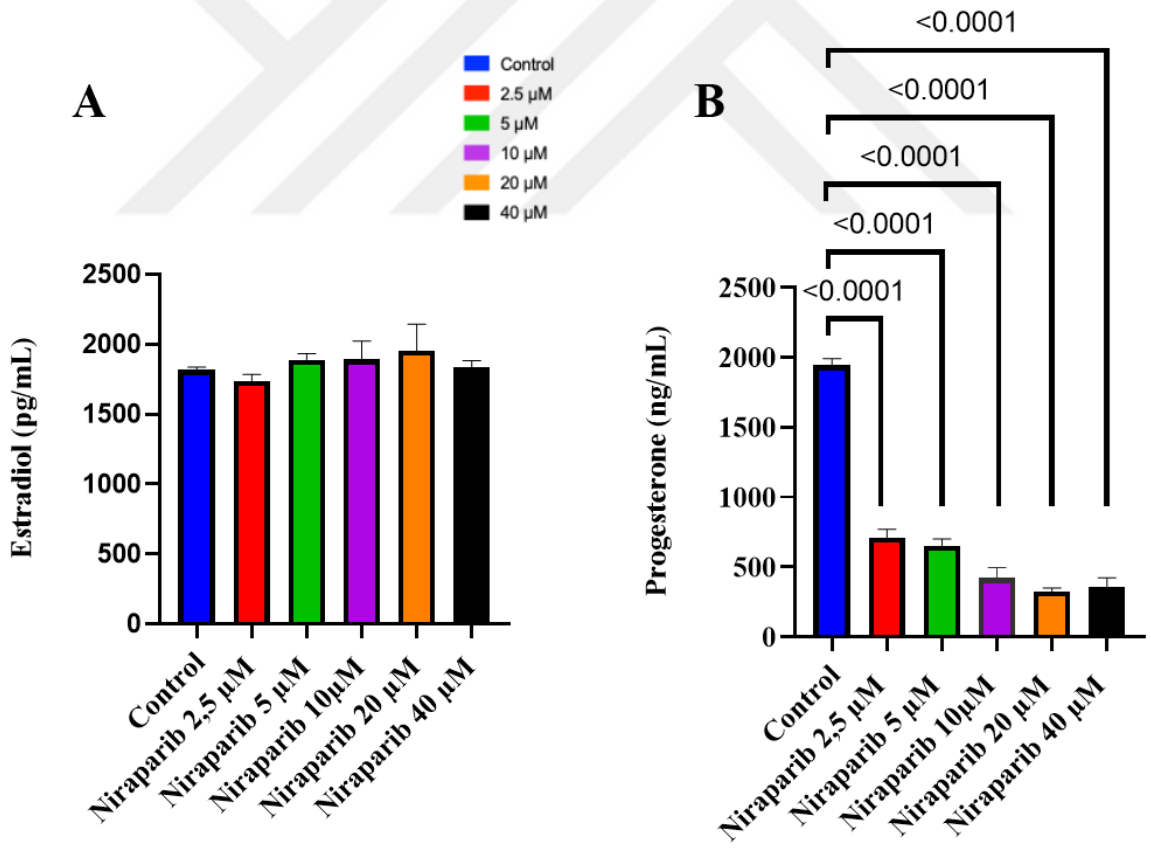

Figure 41. Effects of 72-hour, dose-dependent Niraparib treatment on steroid hormone secretion in HLGCs (A) Estradiol levels after 72-hour treatment. (B) Progesterone levels after

72-hour treatment. The cells were exposed to niraparib at doses ranging from 2.5 to 40 μM for a period of 72 hours. By the conclusion of the therapy, the hormone concentrations in the culture media have been assessed. A one-way ANOVA and Tukey's multiple comparisons test were used for statistical analysis. Mean ± SD is how the data is presented.

3.2 Effects of PARP Inhibitors on Human Ovarian Tissue In Vitro

3.2.1 Effects on Estradiol and AMH Production

The impact of PARPi on ovarian hormone synthesis was evaluated by quantifying AMH and estradiol levels in the culture medium of human ovarian cortex tissues exposed to either Olaparib or Niraparib (40 μM) for 72 or 96 hours (Figure 42).

Two-way ANOVA for AMH indicated no significant interaction between the type of PARP inhibitor and treatment duration ($P = 0.4497$), and the particular PARP inhibitor (Olaparib vs. Niraparib) did not significantly impact AMH levels ($P = 0.9719$) (Figure 42.a). Only the treatment time significantly influenced AMH concentrations ($P = 0.0194$), accounting about 33.34% of the overall variation observed. Likewise, for estradiol, two-way ANOVA revealed no significant interaction between the type of PARP inhibitor and treatment time ($P = 0.7382$), while the type of PARP inhibitor alone did not substantially influence estrogen secretion ($P = 0.8052$) (Figure 42.b). The length of therapy significantly influenced estrogen levels ($P = 0.0146$), accounting for approximately 38.33% of the overall variation. Ultimately, the results show that in human ovarian tissue cultures, prolonged incubation increased AMH and estrogen secretion (as confirmed by two-way ANOVA and post-hoc Tukey's test), but Olaparib and Niraparib had no apparent impact on hormone production under the tested circumstances.

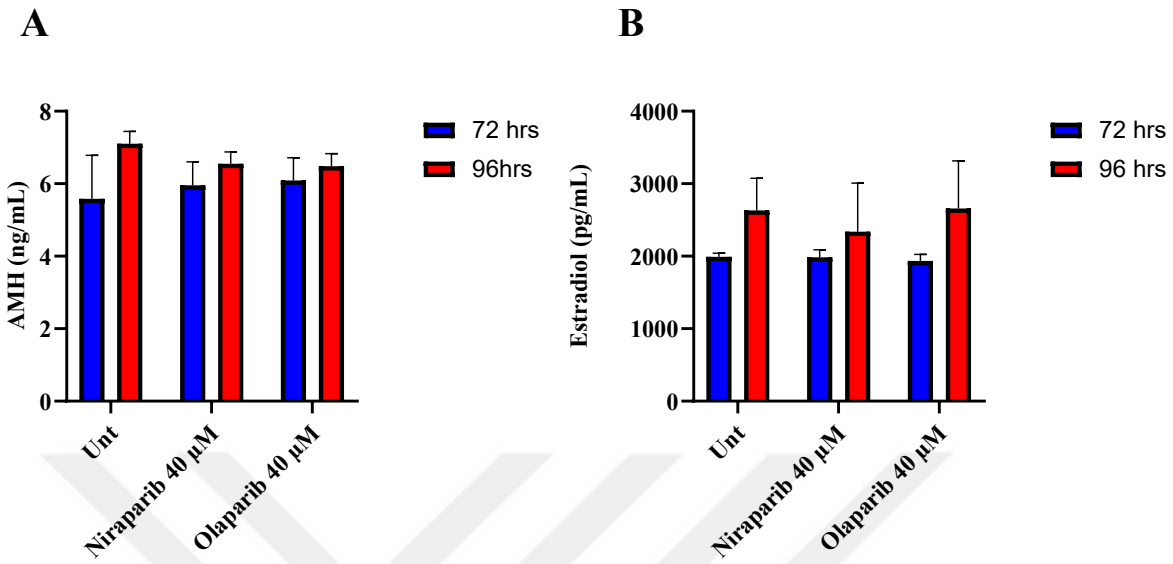

Figure 42. Effect of PARPi on AMH and Estradiol Secretion in Human Ovarian Tissue Cultures at 72 and 96 Hours (A) AMH and (B) Estadiol concentrations in the culture media of human ovarian cortical tissues after treatment with Olaparib or Niraparib (40 µM) for 72 or 96 hours. A two-way ANOVA was used, complemented by a post-hoc Tukey's test, to compare hormone levels. The data is presented as the mean ± SD.

Expression of Apoptosis-Related and Steroidogenic Proteins

Following 72 hours of exposure of ovarian tissues to 40 µM Niraparib, the expression of proteins associated to cell death was evaluated using Western blotting. Levels of PARP ($p = 0.000498$), cleaved PARP ($p = 0.001491$), and BAX ($p = 0.000498$) have been significantly elevated in comparison to the untreated control. BCL2 expression was markedly reduced ($p = 0.000498$) (Figure 43). Thus, the BAX/BCL2 ratio—a frequently used marker of pro-apoptotic shift—has been significantly increased compared to the untreated ($p = 0.0003$), signifying increased apoptotic signaling after high-dose Niraparib administration.

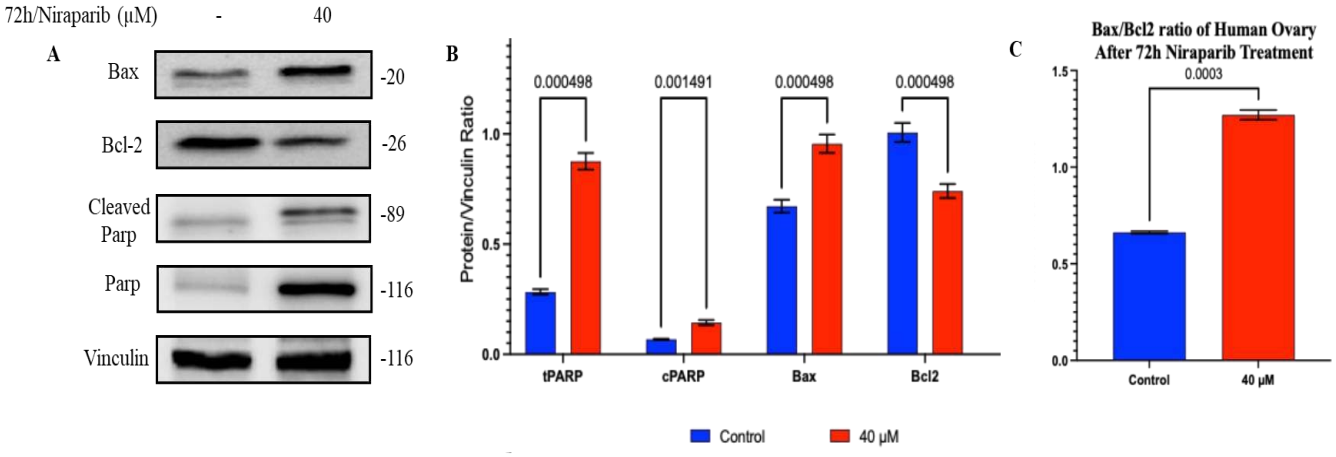

Figure 43. Effects of 40 μM Niraparib on apoptosis-related protein expression in ovarian tissues after 72 hours of exposure. (A) Representative Western blot images showing PARP, cleaved PARP, BAX, and BCL2 protein expression in untreated and Niraparib-treated groups. Vinculin is shown as a loading control. (B) Quantification of individual protein band intensities normalized to vinculin. (C) BAX/BCL2 ratio. Data are presented as mean ± SEM.

At the same ovarian tissue samples, the expression levels of key steroidogenic enzymes, including CYP11A1, 3β-HSD, CYP17A1, STAR, and 17β-HSD, were assessed by Western blot. CYP11A1 expression showed a decrease compared with control, whereas 3β-HSD, CYP17A1, StAR, and 17β-HSD exhibited an upward trend in the Niraparib-treated group (Figure 44). However, none of these changes reached statistical significance.

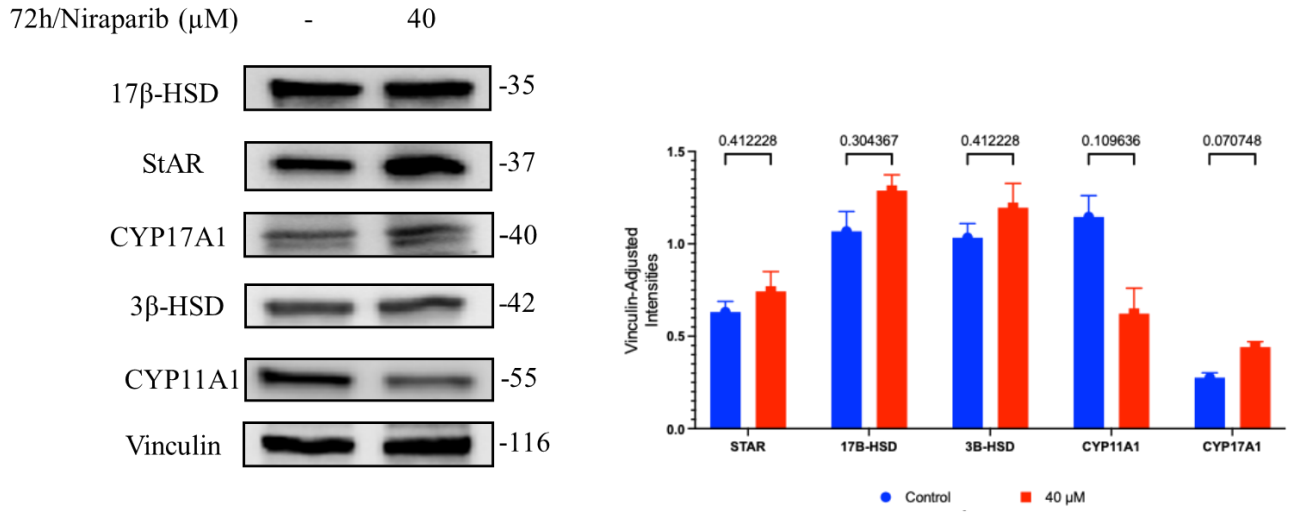

Figure 44. Impact of 40 µM Niraparib on steroidogenic protein expression in ovarian tissues after 72 hours of treatment. (A)Representative Western blot images showing the expression of CYP11A1, 3β-HSD, CYP17A1, StAR, and 17β-HSD in control and Niraparib-treated groups. (B) Quantification of steroidogenic protein band intensities, adjusted to vinculin. The data are presented as the mean ± SEM.

3.3 Effects of PARP Inhibitors on Human Testicular Tissue In Vitro

3.3.1 Expression of Cleaved Parp

Western blotting analyses were performed to evaluate the expression of cleaved PARP protein, subsequent to testicular tissue treatment with Niraparib (2,5 µM, 5 µM, 10 µM, 20 µM, and 40 µM) for 96 hours. The untreated control did not exhibit any detectable signal for cleaved PARP, whereas all Niraparib-treated groups exhibited specific bands. At 10 µM, 20 µM, and 40 µM, cleaved PARP levels were significantly increased when normalized to the 2.5 µM group, with all increases meeting high statistical significance ($p < 0.001$). (Figure 45).

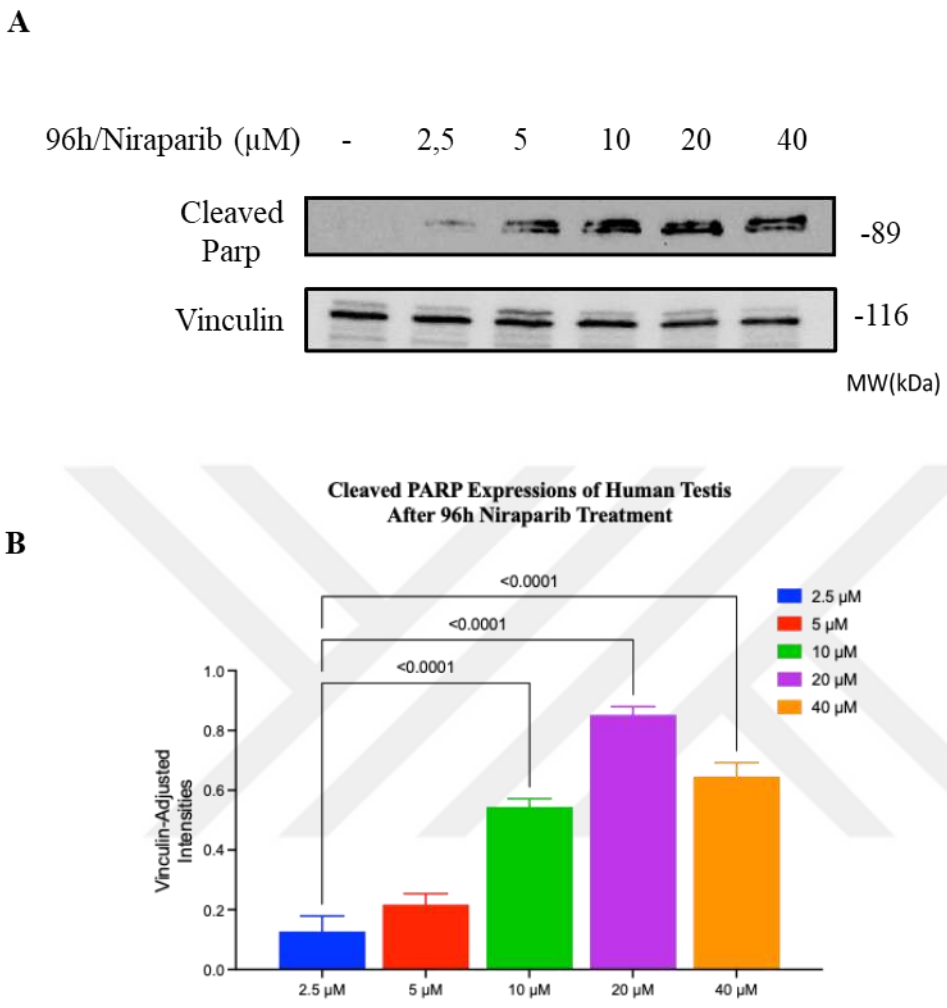

Figure 45. Effects of Niraparib on cleaved PARP expression in testicular tissues after 96 hours exposure. (A) Representative Western blot images showing cleaved PARP protein expression across different Niraparib concentrations compared with untreated control. (B) Quantification of cleaved PARP band intensities normalized to vinculin. Data are presented as mean ± SEM.

3.3.2 Assessment of Testosterone Secretion

Testicular tissue samples from healthy people were cultured and exposed to rising dosages of Olaparib for 96 hours. Testosterone concentrations in the culture media were quantified post-treatment, and statistical evaluation was conducted utilizing one-way ANOVA accompanied by Tukey's multiple comparisons test. Statistical analysis revealed no significant differences within

the therapeutic categories (Figure 46). The results demonstrate that a 96-hour exposure to different dosages of Olaparib does not substantially affect testosterone secretion in healthy human testicular tissue under the specified experimental circumstances.

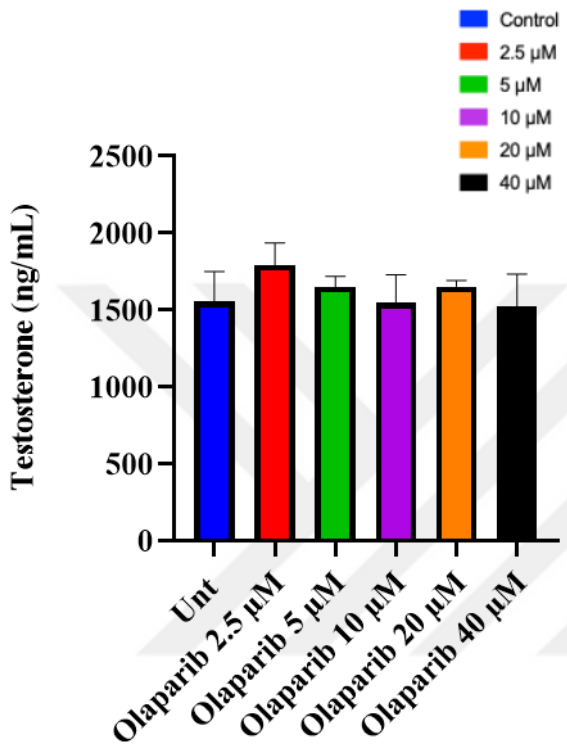

Figure 46. Testosterone levels in human testis tissue after 96-hour Olaparib treatment
Tissues were treated with rising dosages of Olaparib (2.5–40 µM) for 96 hours. Testosterone concentrations in the culture medium were measured at the end of treatment. The data is presented as the mean ±SD.

3.4 Confocal Immunofluorescence Analyses

3.4.1 Immunofluorescence Detection of Cleaved PARP and Steroidogenic Enzymes in Primary Human Luteal Granulosa Cells

HLGCs were subjected to Niraparib treatment (10 µM, 20 µM, or 40 µM) for 96 hours, followed by immunofluorescence labeling to quantify cleaved PARP and 3β-HSD (Figure 47). Quantitative

examination of normalized fluorescence intensity revealed a substantial increase in cleaved PARP signal at all doses of Niraparib compared to the control (10 μM: $p = 0.0158$; 20 μM: $p = 0.0111$; 40 μM: $p = 0.0089$, Tukey's multiple comparisons test). No significant variations were seen across the various dosages of Niraparib, indicating a plateau in apoptotic activation above the minimum therapeutic dose. Niraparib administration, in contrast to the findings of Olaparib, caused a significant, dose-dependent decrease at 3β-HSD fluorescence intensity. All tested values exhibited markedly reduced levels of 3β-HSD in comparison to the control (10 μM: $p = 0.0038$; 20 μM: $p = 0.0062$; 40 μM: $p = 0.0010$). In addition, 40 μM Niraparib resulted in a substantial decrease relative to 20 μM ($p = 0.0336$), demonstrating a gradual decline in steroidogenic enzyme expression with escalating dosage. Data are expressed as mean ± SD.

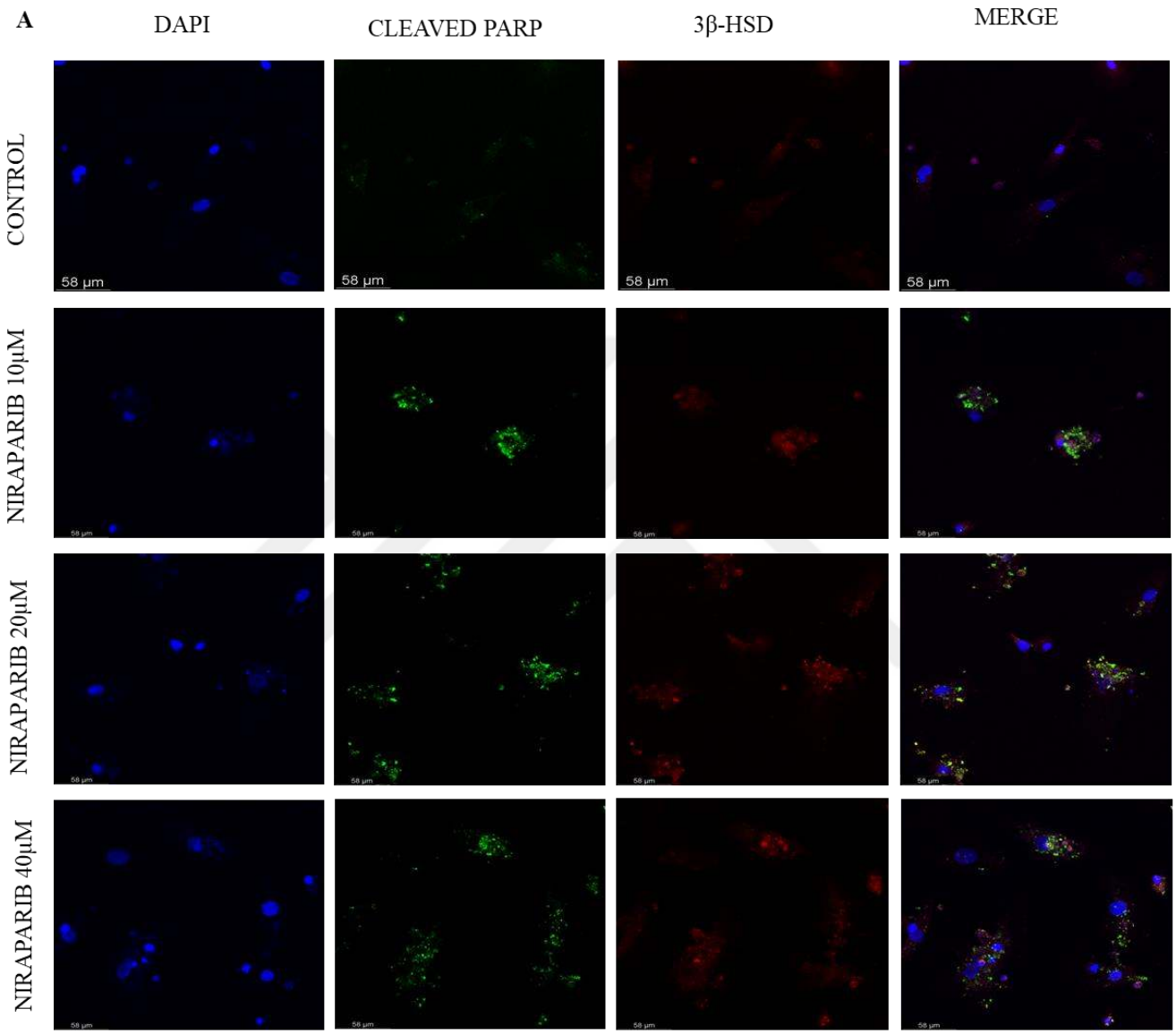
A
DAPI
CLEAVED PARP
3β-HSD
MERGE
CONTROL
NIRAPARIB 10μM
NIRAPARIB 20μM
NIRAPARIB 40μM
58 μm

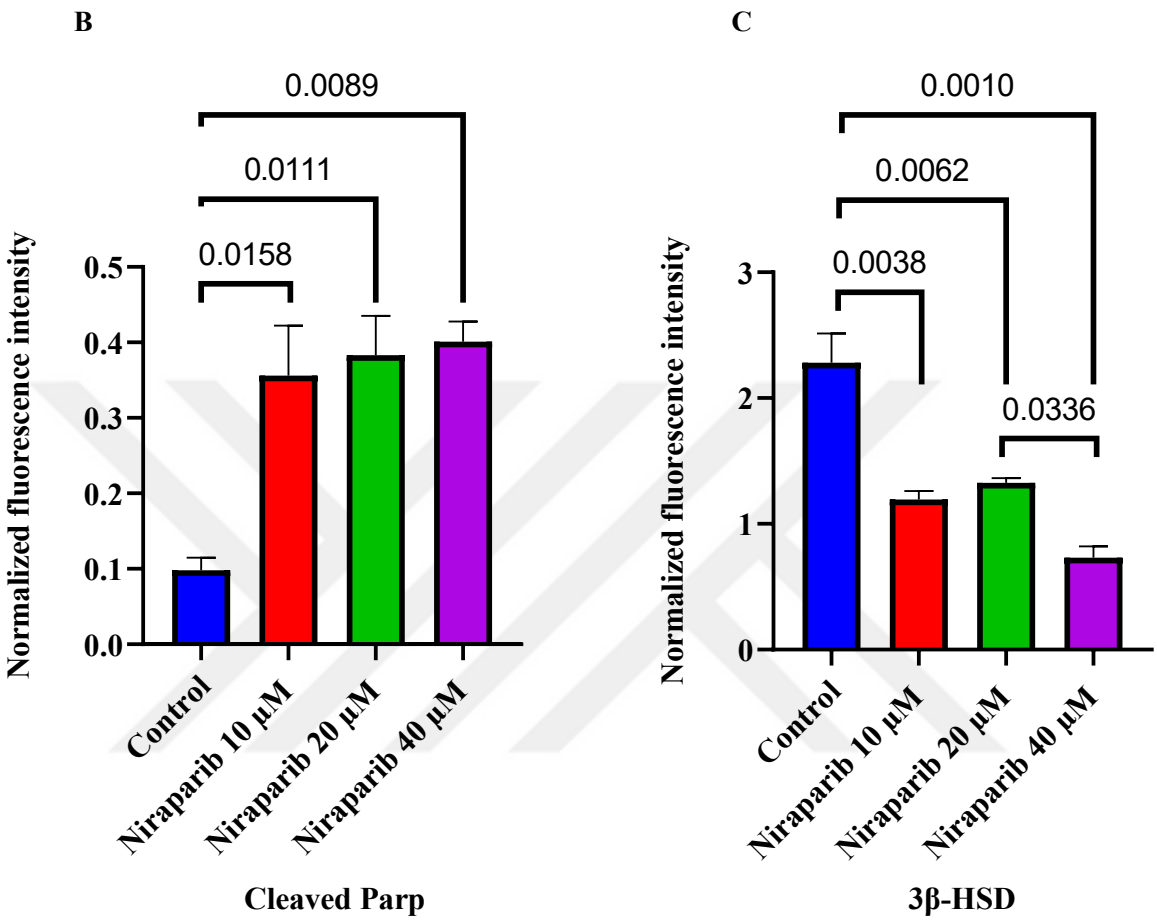

Figure 47. Representative immunofluorescence images (A) and quantification of normalized fluorescence intensity for cleaved PARP (B) and 3β-HSD (C) in HLGCs after a 96-hour treatment with Niraparib at concentrations of 10 µM, 20 µM, and 40 µM.

To further examine the impact of PARP inhibition on apoptosis and steroidogenic enzyme production, the same experimental methodology was used with Olaparib instead of Niraparib. HLGCs had been exposed to Olaparib treatment (10µM, 20µM, or 40µM) for 96 hours, subsequent to which immunofluorescence staining has been conducted to assess cleaved PARP and 3β-HSD protein expressions (Figure 48). The quantitative measurement of normalized fluorescence intensity demonstrated a dose-dependent increase in cleaved PARP signal corresponding to increasing doses of Olaparib. The 10 µM and 20 µM groups demonstrated increased cleaved PARP

fluorescence relative to the control, however these variations lacked statistical significance. On the other hand, treatment with 40 µM Olaparib significantly elevated cleaved PARP fluorescence intensity compared to the untreated ($p = 0.0024$), as well as to the 10 µM ($p = 0.0046$) and 20 µM ($p = 0.0125$) groups. Furthermore, a trend was seen indicating a decrease in normalized fluorescence intensity of 3β-HSD, particularly at 20 µM and 40 µM Olaparib; however, these alterations did not possess statistical significance. Results demonstrate that elevated concentrations of Olaparib significantly cause apoptosis, as seen by enhanced cleaved PARP fluorescence intensity, although lower dosages may trigger early apoptotic signaling without achieving statistical significance. The impact on 3β-HSD fluorescence intensity was less significant under identical experimental circumstances. Data have been reported as mean ± SD.

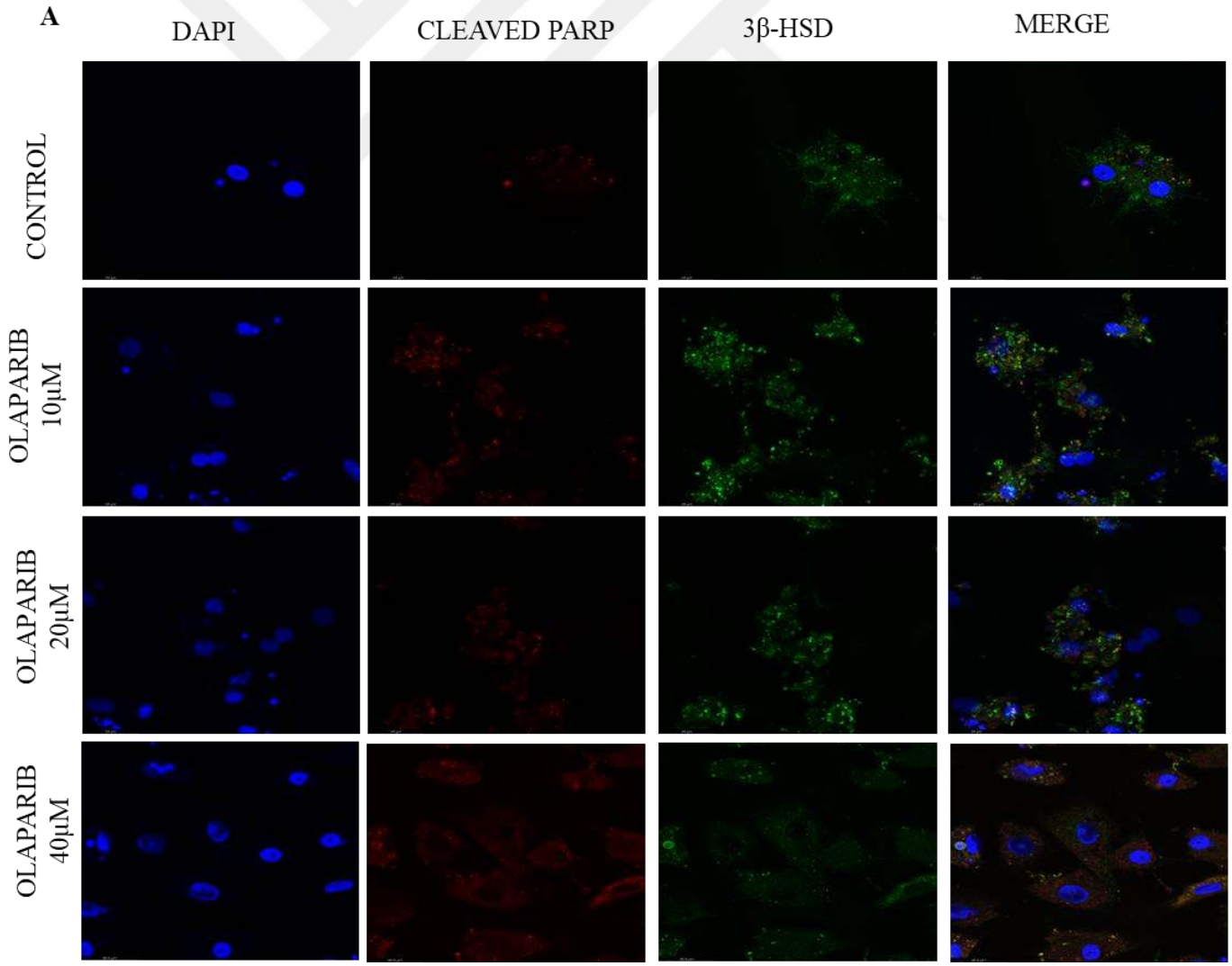

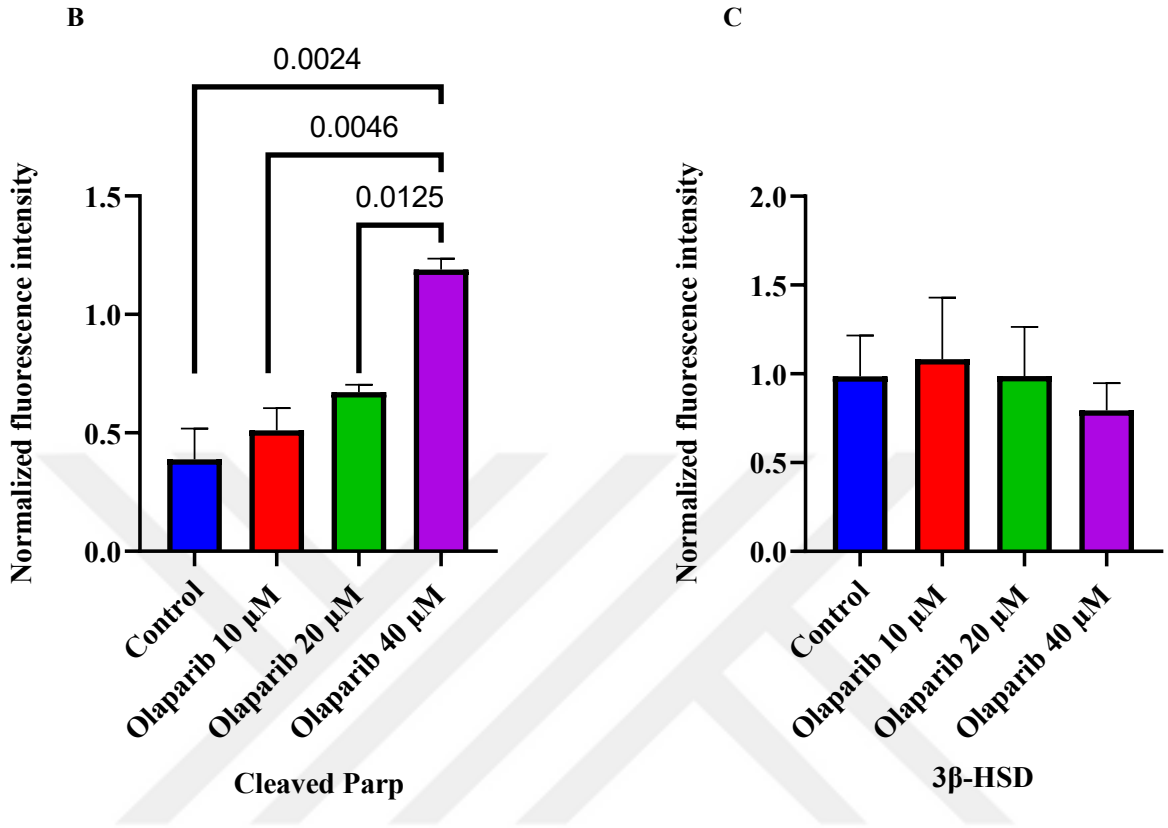

Figure 48. Representative immunofluorescence images (A) and quantification of normalized fluorescence intensity for cleaved PARP (B) and 3β-HSD (C) in HLGCs after a 96-hour treatment with Olaparib at concentrations of 10 µM, 20 µM, and 40 µM.

Both PARP inhibitors elevated cleaved PARP expression; however, Niraparib elicited a more pronounced apoptotic response at reduced doses and demonstrated a greater, dose-dependent inhibition of 3β-HSD relative to Olaparib under similar experimental settings.

3.4.2 Immunofluorescence Detection of Cleaved PARP, Steroidogenic Enzymes, and Basement Membrane Protein in Human Testicular Tissue

To assess the influence of PARPi on steroidogenic enzyme expression in human testicular tissue, testis tissue explants were administered Olaparib at rising dosages for a duration of 96 hours. Immunofluorescence staining was conducted for laminin to confirm tissue integrity and architecture, and for CYP17A1 as a marker of steroidogenic Leydig cells (Figure 49). Laminin

staining validated the anatomical identity and integrity of testicular tissue sections across all groups, indicating that the experimental materials were of testicular origin and were intact during the incubation period.

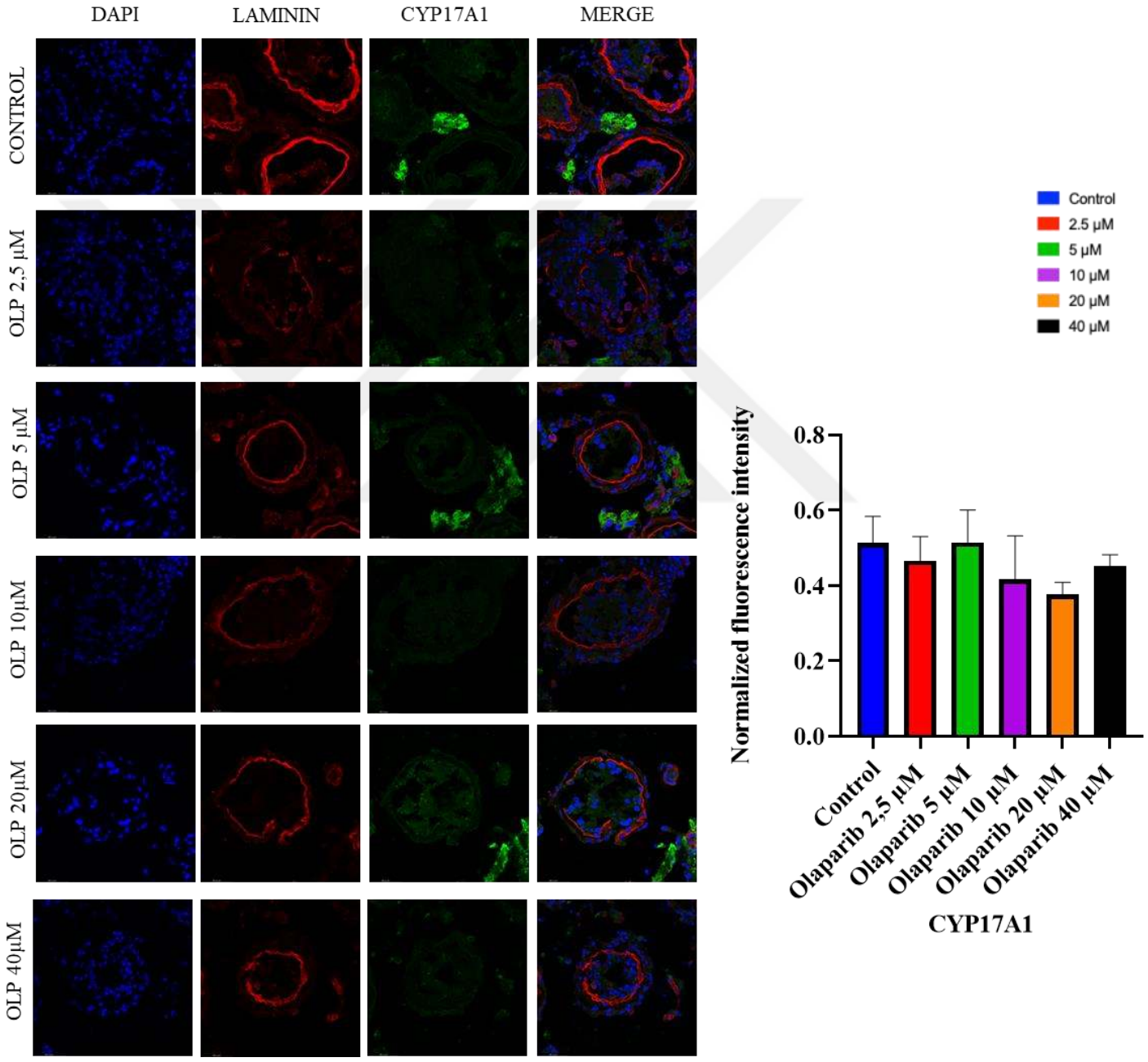

Figure 49. Representative immunofluorescence images of human testis tissue sections stained for laminin (to verify tissue identity and integrity) and CYP17A1 (as a marker of

steroidogenic Leydig cells) after a 96-hour treatment with increasing doses of Olaparib.
OLP = Olaparib The data are reported as the mean ± SD from independent investigations

The quantitative examination of CYP17A1 normalized fluorescence intensity indicated a reduction in CYP17A1 signal in Olaparib treated groups relative to the untreated. Nevertheless, these reductions did not attain statistical significance. Taken together, the data suggest that, under the examined circumstances, Olaparib exposure correlated with a non-significant trend of reduced CYP17A1 expression in testicular tissue, whereas the overall tissue architecture was preserved, as seen by laminin staining.

After validating the anatomical identity and integrity of testicular tissue sections, further immunofluorescence labeling was conducted to evaluate alterations in StAR and Cleaved PARP expression (Figure 50). The quantification of normalized fluorescence intensity for StAR exhibited no consistent nor statistically significant variation across the Olaparib-treated groups relative to the control. Conversely, the fluorescence intensity of cleaved PARP exhibited a significant and dose-dependent increase in testis tissue treated with Olaparib. Marked increases were seen at all dosages relative to the control (2.5 μM: $P = 0.0120$; 5 μM: $P = 0.0388$; 10 μM: $P = 0.0002$; 20 μM: $P < 0.0001$; 40 μM: $P < 0.0001$, Tukey's test). Pairwise comparisons across treatment groups demonstrated incremental increases, peaking at 40 μM Olaparib. Ultimately, the data reveal that Olaparib administration significantly promotes apoptosis, as seen by elevated cleaved PARP levels in testis tissue, whereas its impact on STAR expression is not statistically significant under the same circumstances.

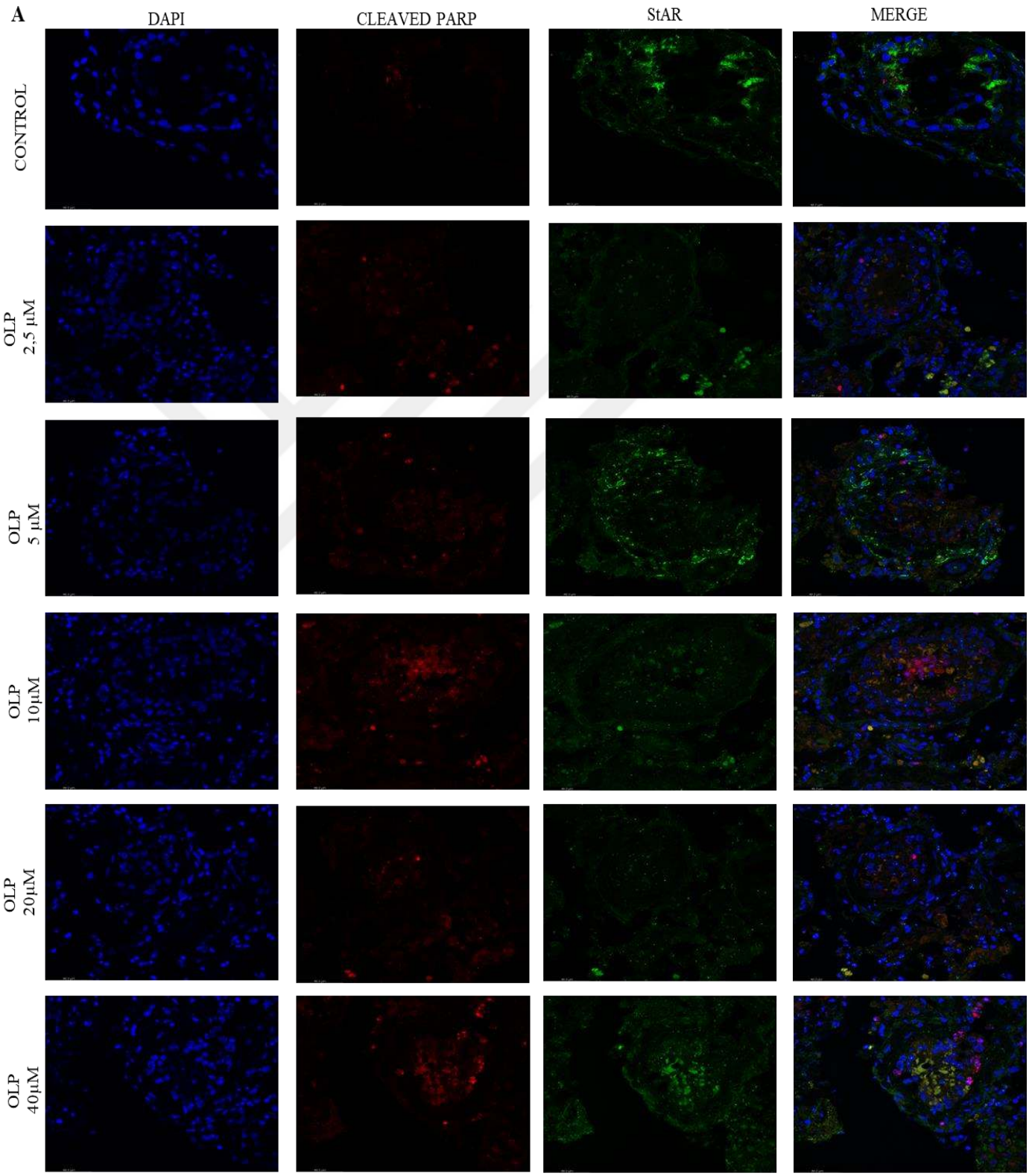
A
DAPI
CLEAVED PARP
StAR
MERGE
CONTROL
OLP 2,5 µM
OLP 5 µM
OLP 10µM
OLP 20µM
OLP 40µM

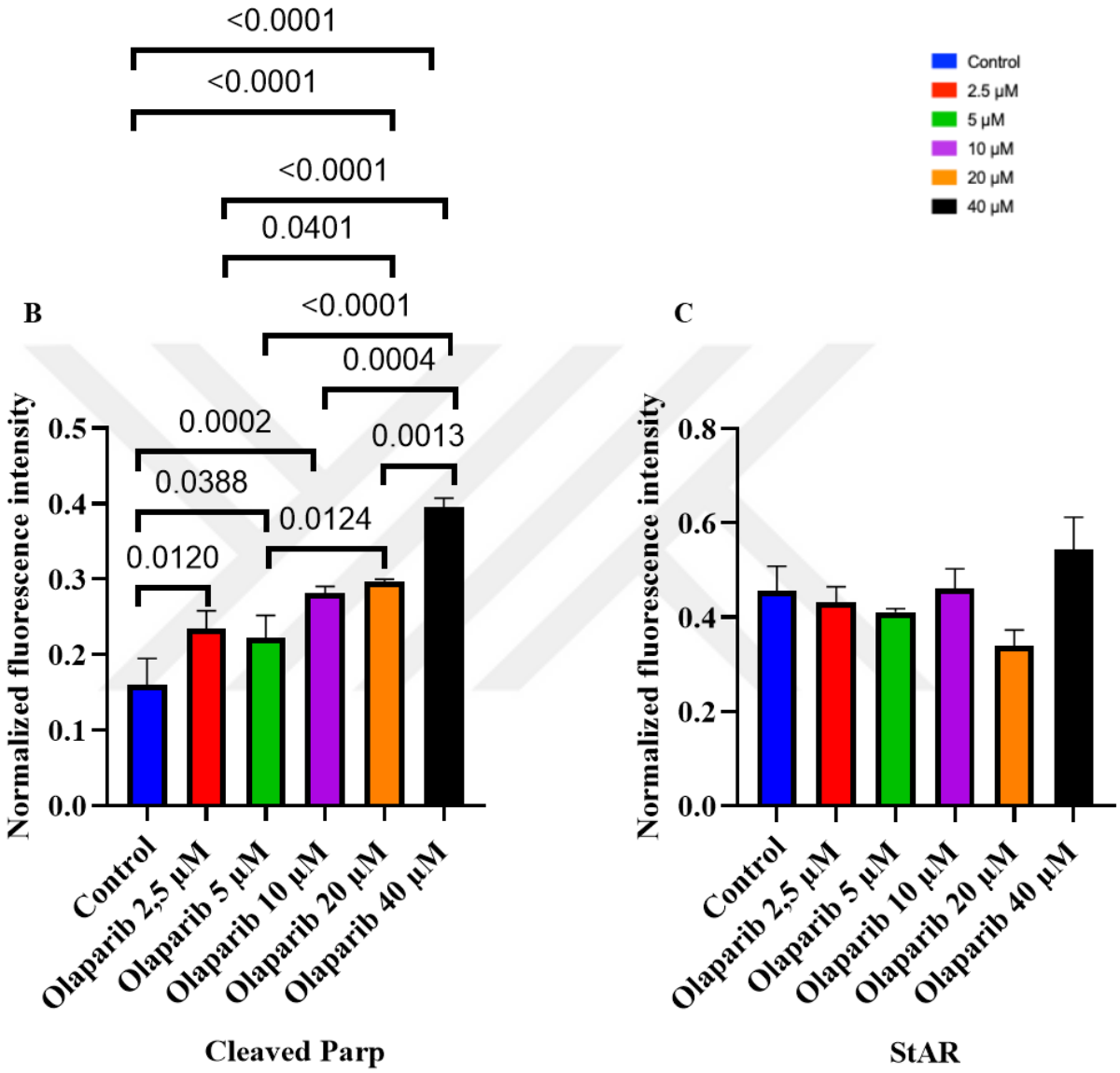

Figure 50. Representative immunofluorescence images and quantification of normalized fluorescence intensity for StAR and Cleaved PARP in human testis tissue after 96-hour treatment with increasing concentrations of Olaparib. OLP = Olaparib Data are presented as mean ± SD from independent experiments.

CHAPTER 4
DISCUSSION

PARPi have been acknowledged not just as effective anticancer drugs but also as substances that may influence reproductive biology, although their specific effects on gonadal function are yet to be determined. This research offers a thorough assessment of two therapeutically significant PARP inhibitors, Olaparib and Niraparib, on human ovarian and testicular cells in vitro. The results reported here contribute to the development of literature that emphasizes the dual role of PARP inhibition in cytotoxicity and reproductive regulation by incorporating real-time proliferation monitoring, cell viability assays, apoptosis profiling, hormone analyses, and evaluations of steroidogenic pathways.

This research demonstrates a significant dose- and time-dependent reduction in cell proliferation, especially at doses of ≥10 μM for both Olaparib and Niraparib. This finding corroborates previous studies that showed the cytostatic and cytotoxic effects of PARP inhibition in granulosa cells (Nakamura et al., 2020; Winship et al., 2020). This is important that low dosages of Niraparib (0.5–2.5 μM) occasionally increased proliferation measures beyond control values, but larger doses consistently inhibited proliferation. This biphasic pattern indicates that PARP inhibitors may have context-dependent effects, perhaps due to varying activation of DNA repair and stress-response pathways at low and high exposure levels. This occurrence highlights the significance of dose in evaluating the off-target reproductive effects of PARP inhibition.

Both inhibitors caused dose-dependent rises in apoptotic signaling, as seen by the buildup of cleaved PARP, higher BAX/BCL2 ratios, and more Zombie dye/PI positive cells. The slope studies of apoptosis induction demonstrated a pronounced increase at lower dosages (10–20 μM), followed by a plateau at higher concentrations, indicative of the saturation of apoptotic pathways. A significant focus of the current study was to examine how steroidogenesis is affected by PARP inhibition. In granulosa cells, treatment with Olaparib significantly decreased the transcripts for important steroidogenic enzymes such as STAR, CYP19A1, and 17β-HSD. Protein-level analysis showed lower StAR expression, no effect on 3β-HSD expression, and different effects on aromatase expression. Niraparib administration, on the other hand, consistently and dose-dependently lowered the levels of 3β-HSD.

These molecular disruptions were reflected at the functional level, resulting in a substantial reduction in progesterone synthesis across all concentrations of Niraparib in granulosa cells. Estradiol and AMH levels, however, remained generally unchanged in both ovarian cells and tissues, suggesting that progesterone production pathways are selectively susceptible to PARP inhibition. In testicular tissue, Olaparib caused a large and dose-dependent rise in cleaved PARP expression, which shows that apoptosis is happening. Nevertheless, testosterone secretion remained unchanged. Reducing progesterone release from granulosa cells is especially significant, given progesterone's critical involvement in follicular maturation, luteal support, and implantation. Consequently, decreased progesterone production may signify a mechanism via which PARPi impair fertility, irrespective of their effects on estradiol. On the other hand, the fact that testosterone synthesis in testicular tissue is so strong may mean that there are compensatory mechanisms that work only in certain cell types or that Leydig cells have a greater threshold for disruption. Moreover, these findings indicate varying sensitivity between ovarian and testicular cells. Granulosa cells consistently showed decreases in steroidogenic gene expression and hormone production, while testicular cells mainly displayed apoptotic changes without significant variations in steroid output. This differentiation prompts compelling inquiries about tissue-specific modulation of PARP activity in reproductive biology, necessitating more exploration into sex-specific susceptibilities. Findings of this study partially overlap with previous reports as (Winship et al., 2020) showed that Olaparib significantly depleted primordial follicles in mice but did not alter serum AMH, corpora lutea counts, or estrous cycling, which is consistent with this observation of unchanged AMH levels in human ovarian tissue. On the other hand, (Nakamura et al., 2020) reported that Olaparib impaired estradiol production, downregulated granulosa cell markers, and induced abnormal granulosa cell morphology in cultured granulosa cells. Unlike their results, estradiol secretion in this human ovarian model was not significantly affected, suggesting possible species- or model-specific differences. The pronounced reduction of progesterone induced by Olaparib and Niraparib corresponds with findings that associate PARP inhibition with decreased steroidogenic gene expression, while further enhancing these findings by measuring functional hormone secretion in human-derived cells. The findings of this study in testicular tissue expand upon previous studies investigating PARP inhibition in the male germline. Pharmacological blockade of PARP has been reported to delay DNA repair in spermatocytes and spermatids, with spermatids showing particular

vulnerability (Atorino et al., 2001). Moreover, depending on the context, PARP inhibition has been shown to modulate apoptotic responses: it increases late apoptotic fractions, particularly in immature sperm (Mahfouz et al., 2009). Additional evidence demonstrates that PARP activity interacts with DNA strand break–inducing enzymes such as TOP2B in spermatids (Meyer-Ficca et al., 2011) and that pharmacological PARP suppression may protect against oxidative stress–induced apoptosis in testicular tissue (Gungor-Ordueri et al., 2019).

In light of these findings, results of this study provide new insights into the testicular response to PARP inhibition. Specifically, Olaparib administration significantly promoted apoptosis, as evidenced by increased cleaved PARP levels, whereas StAR and CYP17A1 expression and testosterone production remained unchanged under the same conditions. These observations suggest that, in testicular tissue, PARP inhibition primarily drives germ cell loss through apoptosis rather than via direct suppression of steroidogenic pathways.

This work is limited by its in vitro methodology, which fails to adequately emulate the complexity of in vivo gonadal physiology, including vascular, stromal, and immunological interactions. The doses of Olaparib and Niraparib used in this study correspond to the top clinical plasma levels; however, prolonged, lower-dose exposures may provide different effects not seen under acute culture circumstances. Furthermore, while apoptosis and steroidogenesis have been thoroughly investigated, additional reproductive endpoints, including angiogenesis, fibrosis, and oocyte/sperm functional competence, have yet to be addressed. Subsequent studies need to integrate organoid and animal models to corroborate these results and to investigate prolonged reproductive consequences. This makes it crucial to investigate the mechanisms behind the selective vulnerability of progesterone production and the variations in how male and female gonads respond to PARP inhibition.

Another limitation of the present study is that ovarian reserve was only assessed indirectly through AMH levels, which did not reveal significant alterations following PARP inhibitor exposure. However, AMH alone may not fully capture the impact of PARP inhibition on ovarian reserve. A more definitive evaluation would require direct quantification of primordial follicles, which represent the true reservoir of ovarian potential. Future studies incorporating histological analysis of follicle numbers are therefore essential to determine whether PARP inhibition compromises the primordial follicle pool in human ovarian tissue.

CHAPTER 5
CONCLUSION

This research shows that PARPi have strong cytotoxic effects on human reproductive cells that depend on the dosage and the duration. Niraparib is the more potent drug that harms HLGCs' steroidogenesis. Olaparib also lowered the levels of steroidogenic enzymes, although its effect on hormone release was not as strong. In contrast, testicular tissues exhibited significant apoptotic activation without substantial impairment of testosterone synthesis. These findings underscore the intricate, cell-type-specific ramifications of PARP inhibition on human reproductive physiology, emphasizing the necessity of meticulously evaluating potential reproductive risks when contemplating PARPi in younger patients or in scenarios of fertility preservation.

BIBLIOGRAPHY

Abraham L. Kierszenbaum, L. T. (2019). *Histology and Cell Biology: An Introduction to Pathology* (5th Edition ed.).

Adamowicz, M., Hailstone, R., Demin, A. A., Komulainen, E., Hanzlikova, H., Brazina, J., . . . Caldecott, K. W. (2021). XRCC1 protects transcription from toxic PARP1 activity during DNA base excision repair. *Nature Cell Biology, 23*(12), 1287-1298.

Agarwal, A., Mahfouz, R. Z., Sharma, R. K., Sarkar, O., Mangrola, D., & Mathur, P. P. (2009). Potential biological role of poly (ADP-ribose) polymerase (PARP) in male gametes. *Reproductive Biology and Endocrinology, 7*, 1-20.

Agarwal, A. K., & Auchus, R. J. (2005). Minireview: cellular redox state regulates hydroxysteroid dehydrogenase activity and intracellular hormone potency. *Endocrinology, 146*(6), 2531-2538.

Albertini, D. F., Combelles, C., Benecchi, E., & Carabatsos, M. J. (2001). Cellular basis for paracrine regulation of ovarian follicle development. *Reproduction, 121*(5), 647-653.

Alharbi, H., Alshehri, A. S., Ahmad, M., & Guo, W. W. (2021). Promising anti-cervical carcinoma and inflammatory agent, resveratrol targets poly (ADP-ribose) polymerase 1 (PARP-1) induced premature ovarian failure with a potent enzymatic modulatory activity. *Journal of Reproductive Immunology, 144*, 103272.

Allinson, S., Dianova, I., & Dianov, G. (2003). Poly (ADP-ribose) polymerase in base excision repair: always engaged, but not essential for DNA damage processing. *Acta Biochimica Polonica, 50*(1), 169-179.

Ashworth, A., & Lord, C. J. (2018). Synthetic lethal therapies for cancer: what's next after PARP inhibitors? *Nature reviews Clinical oncology, 15*(9), 564-576.

Ashworth, A., Lord, C. J., & Reis-Filho, J. S. (2011). Genetic interactions in cancer progression and treatment. *Cell, 145*(1), 30-38.

Atorino, L., Di Meglio, S., Farina, B., Jones, R., & Quesada, P. (2001). Rat germinal cells require PARP for repair of DNA damage induced by γ-irradiation and H2O2 treatment. *European journal of cell biology, 80*(3), 222-229.

Bayasula, Iwase, A., Kiyono, T., Takikawa, S., Goto, M., Nakamura, T., . . . Kobayashi, H. (2012). Establishment of a human nonluteinized granulosa cell line that transitions from the gonadotropin-independent to the gonadotropin-dependent status. *Endocrinology, 153*(6), 2851-2860.

Bhattacharya, I., & Dey, S. (2023). Emerging concepts on Leydig cell development in fetal and adult testis. *Frontiers in endocrinology, 13*, 1086276.

Bildik, G., Akin, N., Esmaeilian, Y., Hela, F., Yildiz, C. S., Iltumur, E., . . . Oktem, O. (2020). Terminal differentiation of human granulosa cells as luteinization is reversed by activin-A through silencing of Jnk pathway. *Cell death discovery, 6*(1), 93. Retrieved from https://www.nature.com/articles/s41420-020-00324-9.pdf

Bird, C., & Kirstein, S. (2009). Real-time, label-free monitoring of cellular invasion and migration with the xCELLigence system. In: Nature Publishing Group US New York.

Bouwman, P., Aly, A., Escandell, J. M., Pieterse, M., Bartkova, J., Van Der Gulden, H., . . . Yang, Q. (2010). 53BP1 loss rescues BRCA1 deficiency and is associated with triple-negative and BRCA-mutated breast cancers. *Nature structural & molecular biology, 17*(6), 688-695.

Bremer, A. A., & Miller, W. L. (2014). Regulation of steroidogenesis. In *Cellular endocrinology in health and disease* (pp. 207-227): Elsevier.

Bruin, M. A., Sonke, G. S., Beijnen, J. H., & Huitema, A. D. (2022). Pharmacokinetics and pharmacodynamics of PARP inhibitors in oncology. *Clinical pharmacokinetics, 61*(12), 1649-1675.

Caldecott, K. W. (2008). Single-strand break repair and genetic disease. *Nature Reviews Genetics, 9*(8), 619-631. Retrieved from https://www.nature.com/articles/nrg2380.pdf

Caldecott, K. W. (2019). XRCC1 protein; Form and function. *DNA repair, 81*, 102664.

Caldecott, K. W. (2020). Mammalian DNA base excision repair: Dancing in the moonlight. *DNA repair, 93*, 102921.

Caldecott, K. W. (2022). DNA single-strand break repair and human genetic disease. *Trends in cell biology, 32*(9), 733-745.

Cameron, D. (2007). Structure and Function of the Male Reproductive System.

Cantó, C., Sauve, A. A., & Bai, P. (2013). Crosstalk between poly (ADP-ribose) polymerase and sirtuin enzymes. *Molecular aspects of medicine, 34*(6), 1168-1201.

Caracciolo, D., Riillo, C., Di Martino, M. T., Tagliaferri, P., & Tassone, P. (2021). Alternative non-homologous end-joining: error-prone DNA repair as cancer's achilles' heel. *Cancers, 13*(6), 1392.

Ceccaldi, R., Liu, J. C., Amunugama, R., Hajdu, I., Primack, B., Petalcorin, M. I., . . . Boulton, S. J. (2015). Homologous-recombination-deficient tumours are dependent on Polθ-mediated repair. *Nature, 518*(7538), 258-262.

Cedars, M. I. (2022). Evaluation of female fertility—AMH and ovarian reserve testing. *The Journal of Clinical Endocrinology & Metabolism, 107*(6), 1510-1519.

Celik-Ozenci, C., & Tasatargil, A. (2013). Role of poly (ADP-ribose) polymerases in male reproduction. *Spermatogenesis, 3*(2), e24194.

Celik-Ozenci, C., Tasatargil, A., Tekcan, M., Sati, L., Gungor, E., Isbir, M., & Demir, R. (2011). Effects of abamectin exposure on male fertility in rats: potential role of oxidative stress-mediated poly (ADP-ribose) polymerase (PARP) activation. *Regulatory Toxicology and Pharmacology, 61*(3), 310-317.

Chapman, J. R., Taylor, M. R., & Boulton, S. J. (2012). Playing the end game: DNA double-strand break repair pathway choice. *Molecular cell, 47*(4), 497-510.

Chen, C.-C., Feng, W., Lim, P. X., Kass, E. M., & Jasin, M. (2018). Homology-directed repair and the role of BRCA1, BRCA2, and related proteins in genome integrity and cancer. *Annual review of cancer biology, 2*(1), 313-336.

Chen, M., Huang, J., Yang, X., Liu, B., Zhang, W., Huang, L., . . . Lu, R. (2012). Serum starvation induced cell cycle synchronization facilitates human somatic cells reprogramming. *PloS one, 7*(4), e28203.

Chen, W., E, Q., Sun, B., Zhang, P., Li, N., Fei, S., . . . Zhang, X. (2023). PARP1-catalyzed PARylation of YY1 mediates endoplasmic reticulum stress in granulosa cells to determine primordial follicle activation. *Cell Death & Disease, 14*(8), 524.

Cheng, Q., Barboule, N., Frit, P., Gomez, D., Bombarde, O., Couderc, B., . . . Calsou, P. (2011). Ku counteracts mobilization of PARP1 and MRN in chromatin damaged with DNA double-strand breaks. *Nucleic acids research, 39*(22), 9605-9619.

Chornenkyy, Y., Agnihotri, S., Yu, M., Buczkowicz, P., Rakopoulos, P., Golbourn, B., . . . Rutka, J. T. (2015). Poly-ADP-ribose polymerase as a therapeutic target in pediatric

diffuse intrinsic pontine glioma and pediatric high-grade astrocytoma. *Molecular cancer therapeutics, 14*(11), 2560-2568.

Christenson, L. K., & Devoto, L. (2003). Cholesterol transport and steroidogenesis by the corpus luteum. *Reproductive Biology and Endocrinology, 1*, 1-9.

Cook, S. A., & Tinker, A. V. (2019). PARP inhibitors and the evolving landscape of ovarian cancer management: a review. *BioDrugs, 33*(3), 255-273.

Dang, Y., Wang, X., Hao, Y., Zhang, X., Zhao, S., Ma, J., . . . Chen, Z.-J. (2018). MicroRNA-379-5p is associated with biochemical premature ovarian insufficiency through PARP1 and XRCC6. *Cell Death & Disease, 9*(2), 106.

Dantzer, F., de la Rubia, G., Ménissier-de Murcia, J., Hostomsky, Z., de Murcia, G., & Schreiber, V. (2000). Base excision repair is impaired in mammalian cells lacking Poly (ADP-ribose) polymerase-1. *Biochemistry, 39*(25), 7559-7569.

Dantzer, F., Mark, M., Quenet, D., Scherthan, H., Huber, A., Liebe, B., . . . de Murcia, G. (2006). Poly (ADP-ribose) polymerase-2 contributes to the fidelity of male meiosis I and spermiogenesis. *Proceedings of the National Academy of Sciences, 103*(40), 14854-14859.

Degroot, L. J., Jameson, J. L., & De Kretser, D. M. (2016). *Endocrinology: adult and pediatric*: Elsevier Saunders.

Demin, A. A., Hirota, K., Tsuda, M., Adamowicz, M., Hailstone, R., Brazina, J., . . . Zha, S. (2021). XRCC1 prevents toxic PARP1 trapping during DNA base excision repair. *Molecular cell, 81*(14), 3018-3030. e3015.

Di Meglio, S., Denegri, M., Tramontano, F., Scovassi, A. I., & Quesada, P. (2003). Poly (ADPR) polymerase-1 and poly (ADPR) glycohydrolase level and distribution in differentiating rat germinal cells. *Molecular and cellular biochemistry, 248*, 85-91.

Edelsztein, N. Y., & Rey, R. A. (2019). Importance of the androgen receptor signaling in gene transactivation and transrepression for pubertal maturation of the testis. *Cells, 8*(8), 861.

Edson, M. A., Nagaraja, A. K., & Matzuk, M. M. (2009). The mammalian ovary from genesis to revelation. *Endocrine reviews, 30*(6), 624-712.

El-Domyati, M. M., Al-Din, A.-B. M., Barakat, M. T., El-Fakahany, H. M., Xu, J., & Sakkas, D. (2009). Deoxyribonucleic acid repair and apoptosis in testicular germ cells of aging fertile men: the role of the poly (adenosine diphosphate-ribosyl) ation pathway. *Fertility and sterility, 91*(5), 2221-2229.

ELCİK, G. B. (2019). *DNA damage-induced and TAp63-mediated oocyte apoptosis is not associated with c-Abl activation in human ovary.* (PhD). Koç University, Retrieved from https://tez.yok.gov.tr/UlusalTezMerkezi/tezSorguSonucYeni.jsp (551222)

Esmaeilian, Y., Hela, F., Bildik, G., İltumur, E., Yusufoglu, S., Yildiz, C. S., . . . Oktem, O. (2023). Autophagy regulates sex steroid hormone synthesis through lysosomal degradation of lipid droplets in human ovary and testis. *Cell Death & Disease, 14*(5), 342.

Esmaeilian, Y., Yusufoglu, S., Iltumur, E., Bildik, G., & Oktem, O. (2024). Visualizing Lipophagy as a New Mechanism of the Synthesis of Sex Steroids in Human Ovary and Testis Using Immunofluorescence Staining Method. In: Springer.

Eustermann, S., Wu, W.-F., Langelier, M.-F., Yang, J.-C., Easton, L. E., Riccio, A. A., . . . Neuhaus, D. (2015). Structural basis of detection and signaling of DNA single-strand breaks by human PARP-1. *Molecular cell, 60*(5), 742-754.

Evans, T. J., & Ganjam, V. K. (2017). Reproductive anatomy and physiology. In *Reproductive and developmental toxicology* (pp. 7-37): Elsevier.

Fietz, D., & Bergmann, M. (2017). Functional anatomy and histology of the testis. In *Endocrinology of the testis and male reproduction* (pp. 313-341): Springer.

Flück, C. E., Miller, W. L., & Auchus, R. J. (2003). The 17, 20-lyase activity of cytochrome P450c17 from human fetal testis favors the Δ5 steroidogenic pathway. *The Journal of Clinical Endocrinology & Metabolism, 88*(8), 3762-3766.

Flück, C. E., & Pandey, A. V. (2014). *Steroidogenesis of the testis–new genes and pathways.* Paper presented at the Annales d'endocrinologie.

Fraser, H. M. (2006). Regulation of the ovarian follicular vasculature. *Reproductive Biology and Endocrinology, 4*, 1-9.

Friedlander, M., Matulonis, U., Gourley, C., Du Bois, A., Vergote, I., Rustin, G., . . . Safra, T. (2018). Long-term efficacy, tolerability and overall survival in patients with platinum-sensitive, recurrent high-grade serous ovarian cancer treated with maintenance olaparib capsules following response to chemotherapy. *British journal of cancer, 119*(9), 1075-1085.

Gizer, M., Önen, S., & Korkusuz, P. (2024). The Evolutionary Route of in vitro Human Spermatogenesis: What is the Next Destination? *Stem Cell Reviews and Reports, 20*(6), 1406-1419.

Gougeon, A. (2010). *Human ovarian follicular development: from activation of resting follicles to preovulatory maturation.* Paper presented at the Annales d'endocrinologie.

Griswold, M. D. (2016). Spermatogenesis: the commitment to meiosis. *Physiological reviews, 96*(1), 1-17.

Gu, M., Wang, Y., & Yu, Y. (2024). Ovarian fibrosis: molecular mechanisms and potential therapeutic targets. *Journal of Ovarian Research, 17*(1), 139.

Gungor-Ordueri, N. E., Kuscu, N., Tasatargil, A., Burgucu, D., Karacan, M., & Celik-Ozenci, C. (2019). Doxorubicin-induced testicular damage is related to PARP-1 signaling molecules in mice. *Pharmacological Reports, 71*(4), 591-602.

Gupta, R., Somyajit, K., Narita, T., Maskey, E., Stanlie, A., Kremer, M., . . . Nussenzweig, A. (2018). DNA repair network analysis reveals shieldin as a key regulator of NHEJ and PARP inhibitor sensitivity. *Cell, 173*(4), 972-988. e923.

Gura, M. A., & Freiman, R. N. (2018). Primordial follicle.

Gwynne, J. T., & Strauss, J. F. (1982). The role of lipoproteins in steroidogenesis and cholesterol metabolism in steroidogenic glands. *Endocr Rev, 3*(3), 299-329.

Haggstrom, M. (2014). Diagram of the pathways of human steroidogenesis. *WikiJournal of medicine, 1*(1), 1-5.

Haince, J.-F., Kozlov, S., Dawson, V. L., Dawson, T. M., Hendzel, M. J., Lavin, M. F., & Poirier, G. G. (2007). Ataxia telangiectasia mutated (ATM) signaling network is modulated by a novel poly (ADP-ribose)-dependent pathway in the early response to DNA-damaging agents. *Journal of Biological Chemistry, 282*(22), 16441-16453.

Haince, J.-F., McDonald, D., Rodrigue, A., Déry, U., Masson, J.-Y., Hendzel, M. J., & Poirier, G. G. (2008). PARP1-dependent kinetics of recruitment of MRE11 and NBS1 proteins to multiple DNA damage sites. *Journal of Biological Chemistry, 283*(2), 1197-1208.

Hall, P. F. (1986). Cytochromes P-450 and the regulation of steroid synthesis. *Steroids, 48*(3-4), 131-196.

Hanzlikova, H., Gittens, W., Krejcikova, K., Zeng, Z., & Caldecott, K. W. (2017). Overlapping roles for PARP1 and PARP2 in the recruitment of endogenous XRCC1 and PNKP into oxidized chromatin. *Nucleic acids research, 45*(5), 2546-2557.

Hillier, S. G., Whitelaw, P. F., & Smyth, C. D. (1994). Follicular oestrogen synthesis: the 'two-cell, two-gonadotrophin'model revisited. *Molecular and cellular endocrinology, 100*(1-2), 51-54.

Hu, Y., Petit, S. A., Ficarro, S. B., Toomire, K. J., Xie, A., Lim, E., . . . Scully, R. (2014). PARP1-driven poly-ADP-ribosylation regulates BRCA1 function in homologous recombination–mediated DNA repair. *Cancer discovery, 4*(12), 1430-1447.

Huber, A., Bai, P., De Murcia, J. M., & De Murcia, G. (2004). PARP-1, PARP-2 and ATM in the DNA damage response: functional synergy in mouse development. *DNA repair, 3*(8-9), 1103-1108.

Jha, R., Agarwal, A., Mahfouz, R., Paasch, U., Grunewald, S., Sabanegh, E., . . . Sharma, R. (2009). Determination of Poly (ADP-ribose) polymerase (PARP) homologues in human ejaculated sperm and its correlation with sperm maturation. *Fertility and sterility, 91*(3), 782-790.

Jiang, K., & Jorgensen, J. S. (2024). Fetal Leydig cells: What we know and what we don't. *Molecular Reproduction and Development, 91*(3), e23739.

Jinno, M. (2025). Ovarian stimulation by promoting basal follicular growth. *Reproductive Biology and Endocrinology, 23*(1), 35.

John E. Hall, M. E. H. (2020). *Guyton and Hall Textbook of Medical Physiology* (14th Edition ed.).

Joshi, A., Mahfooz, S., Maurya, V. K., Kumar, V., Basanna, C. S., Kaur, G., . . . Jha, R. K. (2014). PARP1 during embryo implantation and its upregulation by oestradiol in mice. *Reproduction, 147*(6), 765-780.

Ju, B.-G., Lunyak, V. V., Perissi, V., Garcia-Bassets, I., Rose, D. W., Glass, C. K., & Rosenfeld, M. G. (2006). A topoisomerase IIβ-mediated dsDNA break required for regulated transcription. *Science, 312*(5781), 1798-1802.

Kent, T., Chandramouly, G., McDevitt, S. M., Ozdemir, A. Y., & Pomerantz, R. T. (2015). Mechanism of microhomology-mediated end-joining promoted by human DNA polymerase θ. *Nature structural & molecular biology, 22*(3), 230-237.

Kim, D. H., Lee, H. R., Kim, M. G., Lee, J. S., Jin, S. J., & Lee, H. T. (2017). The effect of poly (ADP-ribosyl) ation inhibition on the porcine cumulus-oocyte complex during in vitro maturation. *Biochemical and Biophysical Research Communications, 483*(1), 752-758.

Kondratska, O., Grushka, N., Pavlovych, S., Krasutska, N., Tsyhankov, S., & Yanchii, R. (2021). Effects of poly (ADP-ribose) polymerase inhibition on DNA integrity and gene expression in ovarian follicular cells in mice with endotoxemia. *Iranian Biomedical Journal, 26*(1), 44.

Konstantinopoulos, P. A., & Matulonis, U. A. (2018). PARP inhibitors in ovarian cancer: a trailblazing and transformative journey. *Clinical Cancer Research, 24*(17), 4062-4065.

Kopeika, J., Kopeika, E., Zhang, T., Rawson, D. M., & Holt, W. V. (2004). Effect of DNA repair inhibitor (3-aminobenzamide) on genetic stability of loach (Misgurnus fossilis) embryos derived from cryopreserved sperm. *Theriogenology, 61*(9), 1661-1673.

Kubeil, C., Yeung, J. C. I., Tuckey, R. C., Rodgers, R. J., & Martin, L. L. (2016). Membrane-Mediated Protein–Protein Interactions of Cholesterol Side-Chain Cleavage Cytochrome P450 with its Associated Electron Transport Proteins. *ChemPlusChem, 81*(9), 995-1002.

Kummar, S., Chen, A., Parchment, R. E., Kinders, R. J., Ji, J., Tomaszewski, J. E., & Doroshow, J. H. (2012). Advances in using PARP inhibitors to treat cancer. *BMC medicine, 10*, 1-5.

Kuzminov, A. (2001). Single-strand interruptions in replicating chromosomes cause double-strand breaks. *Proceedings of the National Academy of Sciences, 98*(15), 8241-8246.

Langelier, M.-F., Eisemann, T., Riccio, A. A., & Pascal, J. M. (2018). PARP family enzymes: regulation and catalysis of the poly (ADP-ribose) posttranslational modification. *Current opinion in structural biology, 53*, 187-198.

Langelier, M.-F., Ruhl, D. D., Planck, J. L., Kraus, W. L., & Pascal, J. M. (2010). The Zn3 domain of human poly (ADP-ribose) polymerase-1 (PARP-1) functions in both DNA-dependent poly (ADP-ribose) synthesis activity and chromatin compaction. *Journal of Biological Chemistry, 285*(24), 18877-18887.

Lee, H. R., Gupta, M. K., Kim, D. H., Hwang, J. H., Kwon, B., & Lee, H. T. (2016). Poly (ADP-ribosyl) ation is involved in pro-survival autophagy in porcine blastocysts. *Molecular Reproduction and Development, 83*(1), 37-49.

Li, J., Li, Q., Zhang, L., Zhang, S., & Dai, Y. (2023). Poly-ADP-ribose polymerase (PARP) inhibitors and ovarian function. *Biomedicine & Pharmacotherapy, 157*, 114028.

Lindahl, T., & Barnes, D. (2000). *Repair of endogenous DNA damage.* Paper presented at the Cold Spring Harbor symposia on quantitative biology.

Lobb, D. K., & Younglai, E. V. (2006). Ontario, Canada: A simplified method for preparing IVF granulosa cells for culture. *Journal of Assisted Reproduction and Genetics, 23*, 93-95.

Lord, C. J., & Ashworth, A. (2017). PARP inhibitors: the first synthetic lethal targeted therapy. *Science (New York, NY), 355*(6330), 1152.

Luijsterburg, M. S., de Krijger, I., Wiegant, W. W., Shah, R. G., Smeenk, G., de Groot, A. J., . . . Shah, G. M. (2016). PARP1 links CHD2-mediated chromatin expansion and H3. 3 deposition to DNA repair by non-homologous end-joining. *Molecular cell, 61*(4), 547-562.

Ma, L., Shen, W., Zhang, J., Ma, L., Shen, W., Shen, W., . . . Zhang, J. (2023). The life cycle of the ovary. In *Ovarian aging* (pp. 7-33): Springer.

Macklon, N. S., & Fauser, B. C. (2001). Follicle-stimulating hormone and advanced follicle development in the human. *Archives of medical research, 32*(6), 595-600.

Magoffin, D. A. (2005). Ovarian theca cell. *The international journal of biochemistry & cell biology, 37*(7), 1344-1349.

Mahfouz, R. Z., Sharma, R. K., Poenicke, K., Jha, R., Paasch, U., Grunewald, S., & Agarwal, A. (2009). Evaluation of poly (ADP-ribose) polymerase cleavage (cPARP) in ejaculated human sperm fractions after induction of apoptosis. *Fertility and sterility, 91*(5), 2210-2220.

Makogon, N., Voznesenskaya, T., Bryzgina, T., Sukhina, V., Grushka, N., & Alexeyeva, I. (2010). Poly (ADP–ribose) polymerase inhibitor, 3–aminobenzamide, protects against experimental immune ovarian failure in mice. *Reproductive biology, 10*(3), 215-226.

Malewicz, M., Kadkhodaei, B., Kee, N., Volakakis, N., Hellman, U., Viktorsson, K., . . . van Gent, D. C. (2011). Essential role for DNA-PK-mediated phosphorylation of NR4A nuclear orphan receptors in DNA double-strand break repair. *Genes & development, 25*(19), 2031-2040.

Marteijn, J. A., Lans, H., Vermeulen, W., & Hoeijmakers, J. H. (2014). Understanding nucleotide excision repair and its roles in cancer and ageing. *Nature reviews Molecular cell biology, 15*(7), 465-481.

Martinez-Serra, J., Gutierrez, A., Muñoz-Capó, S., Navarro-Palou, M., Ros, T., Amat, J. C., . . . Suquia, A. G. (2014). xCELLigence system for real-time label-free monitoring of growth and viability of cell lines from hematological malignancies. *OncoTargets and therapy*, 985-994.

Matveeva, E. A., Al-Tinawi, Q. M., Rouchka, E. C., & Fondufe-Mittendorf, Y. N. (2019). Coupling of PARP1-mediated chromatin structural changes to transcriptional RNA polymerase II elongation and cotranscriptional splicing. *Epigenetics & chromatin, 12*, 1-18.

Maymon, B. B.-S., Cohen-Armon, M., Yavetz, H., Yogev, L., Lifschitz-Mercer, B., Kleiman, S. E., . . . Paz, G. (2006). Role of poly (ADP-ribosyl) ation during human spermatogenesis. *Fertility and sterility, 86*(5), 1402-1407.

McGee, E. A., & Hsueh, A. J. (2000). Initial and cyclic recruitment of ovarian follicles. *Endocrine reviews, 21*(2), 200-214.

Meroni, S. B., Galardo, M. N., Rindone, G., Gorga, A., Riera, M. F., & Cigorraga, S. B. (2019). Molecular mechanisms and signaling pathways involved in sertoli cell proliferation. *Frontiers in endocrinology, 10*, 224.

Mescher, A. L. (2024a). The Female Reproductive System. In *Junqueira's Basic Histology: Text and Atlas, 17th Edition*. New York, NY: McGraw Hill.

Mescher, A. L. (2024b). The Male Reproductive System. In *Junqueira's Basic Histology: Text and Atlas, 17th Edition*. New York, NY: McGraw Hill.

Meyer-Ficca, M. L., Lonchar, J., Credidio, C., Ihara, M., Li, Y., Wang, Z.-Q., & Meyer, R. G. (2009). Disruption of poly (ADP-ribose) homeostasis affects spermiogenesis and sperm chromatin integrity in mice. *Biology of reproduction, 81*(1), 46-55.

Meyer-Ficca, M. L., Lonchar, J. D., Ihara, M., Meistrich, M. L., Austin, C. A., & Meyer, R. G. (2011). Poly (ADP-ribose) polymerases PARP1 and PARP2 modulate topoisomerase II beta (TOP2B) function during chromatin condensation in mouse spermiogenesis. *Biology of reproduction, 84*(5), 900-909.

Meyer-Ficca, M. L., Meyer, R. G., Jacobson, E. L., & Jacobson, M. K. (2005). Poly (ADP-ribose) polymerases: managing genome stability. *The international journal of biochemistry & cell biology, 37*(5), 920-926.

Meyer-Ficca, M. L., Scherthan, H., Bürkle, A., & Meyer, R. G. (2005). Poly (ADP-ribosyl) ation during chromatin remodeling steps in rat spermiogenesis. *Chromosoma, 114*, 67-74.

Michelena, J., Lezaja, A., Teloni, F., Schmid, T., Imhof, R., & Altmeyer, M. (2018). Analysis of PARP inhibitor toxicity by multidimensional fluorescence microscopy reveals mechanisms of sensitivity and resistance. *Nature communications, 9*(1), 2678.

Miller, W. (2008). Steroidogenic enzymes. *Endocrine development, 13*(R), 1.

Miller, W. L. (2007). Steroidogenic acute regulatory protein (StAR), a novel mitochondrial cholesterol transporter. *Biochimica et Biophysica Acta (BBA)-Molecular and Cell Biology of Lipids, 1771*(6), 663-676. Retrieved from https://www.sciencedirect.com/science/article/abs/pii/S1388198107000431?via%3Dihub

Miller, W. L. (2013). Steroid hormone synthesis in mitochondria. *Molecular and cellular endocrinology, 379*(1-2), 62-73.

Miller, W. L., & Auchus, R. J. (2011). The molecular biology, biochemistry, and physiology of human steroidogenesis and its disorders. *Endocrine reviews, 32*(1), 81-151.

Mital, P., Hinton, B. T., & Dufour, J. M. (2011). The blood-testis and blood-epididymis barriers are more than just their tight junctions. *Biology of reproduction, 84*(5), 851-858.

Mruk, D. D., & Cheng, C. Y. (2015). The mammalian blood-testis barrier: its biology and regulation. *Endocrine reviews, 36*(5), 564-591.

Murai, J., Huang, S.-Y. N., Das, B. B., Renaud, A., Zhang, Y., Doroshow, J. H., . . . Pommier, Y. (2012). Trapping of PARP1 and PARP2 by clinical PARP inhibitors. *Cancer research, 72*(21), 5588-5599.

Murdoch, W. (1998). Perturbation of sheep ovarian surface epithelial cells by ovulation: evidence for roles of progesterone and poly (ADP-ribose) polymerase in the restoration of DNA integrity. *Journal of endocrinology, 156*(3), 503-528.

Nakamura, K., Takae, S., Shiraishi, E., Shinya, K., Igualada, A. J., & Suzuki, N. (2020). Poly (ADP-ribose) polymerase inhibitor exposure reduces ovarian reserve followed by dysfunction in granulosa cells. *Scientific Reports, 10*(1), 17058.

Namwanje, M., & Brown, C. W. (2016). Activins and inhibins: roles in development, physiology, and disease. *Cold Spring Harbor perspectives in biology, 8*(7), a021881.

O'shaughnessy, P., Verhoeven, G., De Gendt, K., Monteiro, A., & Abel, M. (2010). Direct action through the sertoli cells is essential for androgen stimulation of spermatogenesis. *Endocrinology, 151*(5), 2343-2348.

Orellana, E. A., & Kasinski, A. L. (2016). Sulforhodamine B (SRB) assay in cell culture to investigate cell proliferation. *Bio-protocol, 6*(21), e1984-e1984. Retrieved from https://pmc.ncbi.nlm.nih.gov/articles/PMC5448418/pdf/nihms844985.pdf

Pawlina, W., & Ross, M. H. (2018). *Histology: a text and atlas: with correlated cell and molecular biology*: Lippincott Williams & Wilkins.

Plant, T., Ramaswamy, S., & De Gendt, K. (2016). Endocrine Control of Spermatogenesis.

Plant, T. M., & Zeleznik, A. J. (2014). *Knobil and Neill's physiology of reproduction*: Academic Press.

Polo, L. M., Xu, Y., Hornyak, P., Garces, F., Zeng, Z., Hailstone, R., . . . Pearl, L. H. (2019). Efficient single-strand break repair requires binding to both poly (ADP-ribose) and DNA by the central BRCT domain of XRCC1. *Cell reports, 26*(3), 573-581. e575.

Polo, S. E., & Jackson, S. P. (2011). Dynamics of DNA damage response proteins at DNA breaks: a focus on protein modifications. *Genes & development, 25*(5), 409-433.

Pommier, Y., O'Connor, M. J., & De Bono, J. (2016). Laying a trap to kill cancer cells: PARP inhibitors and their mechanisms of action. *Science translational medicine, 8*(362), 362ps317-362ps317.

Porter, F. D., & Herman, G. E. (2011). Malformation syndromes caused by disorders of cholesterol synthesis. *Journal of lipid research, 52*(1), 6-34.

Purnell, M. R., & Whish, W. (1980). Novel inhibitors of poly (ADP-ribose) synthetase. *Biochemical Journal, 185*(3), 775.

Purvis, K., & Hansson, V. (1978). Hormonal regulation of Leydig cell function. *Molecular and cellular endocrinology, 12*(2), 123-138.

Puttabyatappa, M., & Padmanabhan, V. (2018). Developmental programming of ovarian functions and dysfunctions. *Vitamins and hormones, 107*, 377-422.

Qian, H., Xu, J., Lalioti, M. D., Gulle, K., & Sakkas, D. (2010). Oocyte numbers in the mouse increase after treatment with 5-aminoisoquinolinone: a potent inhibitor of poly (ADP-ribosyl) ation. *Biology of reproduction, 82*(5), 1000-1007.

Rao, P. D., Sankrityayan, H., Srivastava, A., Kulkarni, Y. A., Mulay, S. R., & Gaikwad, A. B. (2020). 'PARP'ing fibrosis: repurposing poly (ADP ribose) polymerase (PARP) inhibitors. *Drug Discovery Today, 25*(7), 1253-1261.

Ray Chaudhuri, A., & Nussenzweig, A. (2017). The multifaceted roles of PARP1 in DNA repair and chromatin remodelling. *Nature reviews Molecular cell biology, 18*(10), 610-621.

Robinson, M., Sparanese, S., Witherspoon, L., & Flannigan, R. (2023). Human in vitro spermatogenesis as a regenerative therapy—where do we stand? *Nature Reviews Urology, 20*(8), 461-479.

Ronson, G. E., Piberger, A. L., Higgs, M. R., Olsen, A. L., Stewart, G. S., McHugh, P. J., . . . Lakin, N. D. (2018). PARP1 and PARP2 stabilise replication forks at base excision repair intermediates through Fbh1-dependent Rad51 regulation. *Nature communications, 9*(1), 746.

Said, R. S., El-Demerdash, E., Nada, A. S., & Kamal, M. M. (2016). Resveratrol inhibits inflammatory signaling implicated in ionizing radiation-induced premature ovarian failure through antagonistic crosstalk between silencing information regulator 1 (SIRT1) and poly (ADP-ribose) polymerase 1 (PARP-1). *Biochemical pharmacology, 103*, 140-150.

Said, R. S., Mantawy, E. M., & El-Demerdash, E. (2019). Mechanistic perspective of protective effects of resveratrol against cisplatin-induced ovarian injury in rats: emphasis on anti-inflammatory and anti-apoptotic effects. *Naunyn-Schmiedeberg's archives of pharmacology, 392*, 1225-1238.

Sakugawa, N., Miyamoto, T., Tsujimura, A., Koh, E., Miyagawa, Y., Sato, H., . . . Sengoku, K. (2009). LMTK2 and PARP-2 gene polymorphism and azoospermia secondary to meiotic arrest. *Journal of Assisted Reproduction and Genetics, 26*, 545-552.

Sartorius, C., Takimoto, G., Richer, J., Tung, L., & Horwitz, K. (2000). Association of the Ku autoantigen/DNA-dependent protein kinase holoenzyme and poly (ADP-ribose) polymerase with the DNA binding domain of progesterone receptors. *Journal of Molecular Endocrinology, 24*(2), 165-182.

Schreiber, V., Amé, J.-C., Dollé, P., Schultz, I., Rinaldi, B., Fraulob, V., . . . de Murcia, G. (2002). Poly (ADP-ribose) polymerase-2 (PARP-2) is required for efficient base excision DNA repair in association with PARP-1 and XRCC1. *Journal of Biological Chemistry, 277*(25), 23028-23036.

Schreiber, V., Dantzer, F., Ame, J.-C., & De Murcia, G. (2006). Poly (ADP-ribose): novel functions for an old molecule. *Nature reviews Molecular cell biology, 7*(7), 517-528.

Scott, H. M., Mason, J. I., & Sharpe, R. M. (2009). Steroidogenesis in the fetal testis and its susceptibility to disruption by exogenous compounds. *Endocrine reviews, 30*(7), 883-925.

Shao, Z., Lee, B. J., Zhang, H., Lin, X., Li, C., Jiang, W., . . . Baer, R. (2023). Inactive PARP1 causes embryonic lethality and genome instability in a dominant-negative manner. *Proceedings of the National Academy of Sciences, 120*(31), e2301972120.

Sharpe, R. M., McKinnell, C., Kivlin, C., & Fisher, J. S. (2003). Proliferation and functional maturation of Sertoli cells, and their relevance to disorders of testis function in adulthood. *REPRODUCTION-CAMBRIDGE-, 125*(6), 769-784.

Smeenk, G., Wiegant, W. W., Marteijn, J. A., Luijsterburg, M. S., Sroczynski, N., Costelloe, T., . . . Vermeulen, W. (2013). Poly (ADP-ribosyl) ation links the chromatin remodeler SMARCA5/SNF2H to RNF168-dependent DNA damage signaling. *Journal of cell science, 126*(4), 889-903.

Stocco, D. M., & McPhaul, M. J. (2006). Physiology of testicular steroidogenesis. In *Knobil and Neill's physiology of reproduction* (pp. 977-1016): Elsevier.

Strauss III, J. F. (2019). Organization of ovarian steroidogenic cells and cholesterol metabolism. *The ovary*, 83-94.

Stringer, J. M., Winship, A., Liew, S. H., & Hutt, K. (2018). The capacity of oocytes for DNA repair. *Cellular and molecular life sciences, 75*, 2777-2792.

Ström, C. E., Johansson, F., Uhlen, M., Szigyarto, C. A.-K., Erixon, K., & Helleday, T. (2011). Poly (ADP-ribose) polymerase (PARP) is not involved in base excision repair but PARP inhibition traps a single-strand intermediate. *Nucleic acids research, 39*(8), 3166-3175.

Suede, S. H., Malik, A., & Sapra, A. (2020). Histology, spermatogenesis.

Sun, K., Mikule, K., Wang, Z., Poon, G., Vaidyanathan, A., Smith, G., . . . Wang, J. (2018). A comparative pharmacokinetic study of PARP inhibitors demonstrates favorable properties for niraparib efficacy in preclinical tumor models. *Oncotarget, 9*(98), 37080.

Suzuki, T., Matsuzaki, T., Hagiwara, H., Aoki, T., & Takata, K. (2007). Recent advances in fluorescent labeling techniques for fluorescence microscopy. *Acta histochemica et cytochemica, 40*(5), 131-137. Retrieved from https://www.jstage.jst.go.jp/article/ahc/40/5/40_07023/_pdf

Szántó, M., Brunyánszki, A., Kiss, B., Nagy, L., Gergely, P., Virág, L., & Bai, P. (2012). Poly (ADP-ribose) polymerase-2: emerging transcriptional roles of a DNA-repair protein. *Cellular and molecular life sciences, 69*, 4079-4092. Retrieved from https://pmc.ncbi.nlm.nih.gov/articles/PMC11114944/pdf/18_2012_Article_1003.pdf

Tentori, L., Lacal, P. M., Muzi, A., Dorio, A. S., Leonetti, C., Scarsella, M., . . . Stoppacciaro, A. (2007). Poly (ADP-ribose) polymerase (PARP) inhibition or PARP-1 gene deletion reduces angiogenesis. *European Journal of Cancer, 43*(14), 2124-2133.

Tramontano, F., Malanga, M., & Quesada, P. (2007). Differential contribution of poly (ADP-ribose) polymerase-1 and-2 (PARP-1 and-2) to the poly (ADP-ribosyl) ation reaction in rat primary spermatocytes. *Molecular human reproduction, 13*(11), 821-828.

Tubbs, A., & Nussenzweig, A. (2017). Endogenous DNA damage as a source of genomic instability in cancer. *Cell, 168*(4), 644-656. Retrieved from https://pmc.ncbi.nlm.nih.gov/articles/PMC6591730/pdf/nihms-1037106.pdf

van den Berg-Bakker, C. A., Hagemeijer, A., Franken-Postma, E. M., Smit, V. T., Kuppen, P. J., Claasen, H. H. V. R., . . . Schrier, P. I. (1993). Establishment and characterization of 7 ovarian carcinoma cell lines and one granulosa tumor cell line: growth features and cytogenetics. *International journal of cancer, 53*(4), 613-620. Retrieved from https://onlinelibrary.wiley.com/doi/abs/10.1002/ijc.2910530415?sid=nlm%3Apubmed

Verhoeven, G., & CAILLEAU, J. (1988). Follicle-stimulating hormone and androgens increase the concentration of the androgen receptor in Sertoli cells. *Endocrinology, 122*(4), 1541-1550.

Veuger, S. J., Hunter, J. E., & Durkacz, B. W. (2009). Ionizing radiation-induced NF-κB activation requires PARP-1 function to confer radioresistance. *Oncogene, 28*(6), 832-842.

Vichai, V., & Kirtikara, K. (2006). Sulforhodamine B colorimetric assay for cytotoxicity screening. *Nature protocols, 1*(3), 1112-1116. Retrieved from https://www.nature.com/articles/nprot.2006.179

Vida, A., Márton, J., Mikó, E., & Bai, P. (2017). *Metabolic roles of poly (ADP-ribose) polymerases.* Paper presented at the Seminars in cell & developmental biology.

Vodenicharov, M. D., Sallmann, F. R., Satoh, M. S., & Poirier, G. G. (2000). Base excision repair is efficient in cells lacking poly (ADP-ribose) polymerase 1. *Nucleic acids research, 28*(20), 3887-3896.

Vyas, S., Matic, I., Uchima, L., Rood, J., Zaja, R., Hay, R. T., . . . Chang, P. (2014). Family-wide analysis of poly (ADP-ribose) polymerase activity. *Nature communications, 5*(1), 4426.

Wang, Y., Zhang, J., Wu, X., Huang, L., Xiao, W., & Guo, C. (2024). The Potential of PARP Inhibitors as Antitumor Drugs and the Perspective of Molecular Design. *Journal of Medicinal Chemistry*.

Winship, A. L., Griffiths, M., Lliberos Requesens, C., Sarma, U., Phillips, K.-A., & Hutt, K. J. (2020). The PARP inhibitor, olaparib, depletes the ovarian reserve in mice: implications for fertility preservation. *Human Reproduction, 35*(8), 1864-1874.

Wistuba, J., Neuhaus, N., & Nieschlag, E. (2023). Physiology of testicular function. In *Andrology: male reproductive health and dysfunction* (pp. 15-54): Springer.

Yang, F., Baumann, C., & De La Fuente, R. (2009). Persistence of histone H2AX phosphorylation after meiotic chromosome synapsis and abnormal centromere cohesion in poly (ADP-ribose) polymerase (Parp-1) null oocytes. *Developmental biology, 331*(2), 326-338.

Yang, Y.-G., Cortes, U., Patnaik, S., Jasin, M., & Wang, Z.-Q. (2004). Ablation of PARP-1 does not interfere with the repair of DNA double-strand breaks, but compromises the reactivation of stalled replication forks. *Oncogene, 23*(21), 3872-3882.

Yen & Jaffe's Reproductive Endocrinology

Physiology, Pathophysiology, and Clinical Management (2019). (Eighth Edition ed.).

Yıldız, C. S. (2021). *The Effects of Bone Morphogenetic Protein 7 (BMP7) on Steroidogenic Function and Luteinization*

Characteristics of Human Luteal Granulosa Cell. (Master of Science). Koç University, (713131)

Zhang, H., Vollmer, M., De Geyter, M., Litzistorf, Y., Ladewig, A., Dürrenberger, M., . . . De Geyter, C. (2000). Characterization of an immortalized human granulosa cell line (COV434). *Molecular human reproduction, 6*(2), 146-153.

Zhang, Y., Zhou, X., Zhu, Y., Wang, H., Xu, J., & Su, Y. (2021). Current mechanisms of primordial follicle activation and new strategies for fertility preservation. *Molecular human reproduction, 27*(2), gaab005.

Zirkin, B. R., & Papadopoulos, V. (2018). Leydig cells: formation, function, and regulation. *Biology of reproduction, 99*(1), 101-111.